Offshore transport, conditioning and storage of Carbon Dioxide

A comprehensive method to evaluate the suitability of existing offshore infrastructure for the transport and storage of carbon dioxide

Master of Science Thesis

C.P.W. Christiaanse

TU Delft

Offshore transport, conditioning and storage of Carbon Dioxide

by

C.P.W. Christiaanse

Process & Energy Department

Faculty of Mechanical, Maritime and Materials Engineering

Student number: 4049241
Project duration: February 14, 2018 – November 14, 2018
Thesis committee: Prof. dr. ir. B.J. Boersma,   TU Delft, supervisor
                    Dr. R. Delfos,   TU Delft
                    Dr. ir. R. Pecnik,   TU Delft
                    Ir. V. Doedée,   HMC, company supervisor

An electronic version of this thesis is available at `http://repository.tudelft.nl/`.

TUDelft

Abstract

In its 2018 special report, the Intergovernmental Panel on Climate Change emphasizes that carbon emissions have to be cut drastically and immediately to limit global warming to moderate levels that will prevent the worst impacts [1]. Apart from laying out different pathways for industries to realize these drastic cuts with conventional methods - such as efficiency measures, renewable energy sources and electrification - the report stresses the need for a quick integration of carbon dioxide removal technologies into existing processes.

One of many initiatives in line with this advice aims to construct and operate a pipeline network in the port of Rotterdam that collects captured CO_2 from different industries in a central compression station. From here the CO_2 is then liquefied and transported to an offshore storage location by means of a subsea pipeline. The properties of CO_2 require it to become supercritical before injection in order to achieve maximum storage efficiency, which requires additional conditioning steps before it enters the reservoir.

This report presents the first simple and comprehensive method to effectively compare different infrastructure configurations for reservoirs that have been found suitable for long-term storage of carbon dioxide. Modelling the different transport phenomena along the chain, this study identified a fixed set of input parameters and used them to evaluate the differences between existing and new infrastructure. The report then explores how these differences affect the conditioning steps the CO_2 must undergo before injection.

The model was then applied to a a test case, the P18-2 natural gas reservoir $30 km$ northwest of the Hague. The results for this test case show that an auxiliary pumping step is required for supercritical injection at the desired pressure. Subsequently, the results are used to develop a conceptual design for a module that can either be installed on a new platform or retrofitted to existing offshore production facilities, allowing them to be used for conditioning and injection of CO_2. Last, the economic feasibility analysis demonstrates that reusing existing infrastructure can reduce the costs of transport and storage of CO_2 by over 50%.

---

[1]IPCC, 2018: Special Report on Global Warming of 1.5 °C. In Press.

Contents

Glossary

CATO	CO_2 Afvang, Transport en Opslag
CCS	Carbon Capture and Storage
CCUS	Carbon Capture for Utilization and Storage
CDR	Carbon Dioxide Removal
CO$_2$	Carbon Dioxide
CS	Control Surface
CV	Control Volume
EC	European Commission
EEA	European Economic Area
EGR	Enhanced Gas Recovery
EOR	Enhanced Oil Recovery
EOS	Equation of State
ETS	Emission Trading System
EU	European Union
HFG	Heerema Fabrication Group
HMC	Heerema Marine Contractors
IEA	International Energy Agency
IPCC	Intergovernmental Panel on Climate Change
NIST	National Institute of Standards and Technology
PORTHOS	Port Of Rotterdam CO_2 Transport Hub & Offshore Storage
ROAD	Rotterdam Opslag en Afvang Demonstratieproject
RQ	Research Question
UGS	Underground Gas Storage
UNFCCC	United Nations Framework Convention on Climate Change

Nomenclature

Δf	Change in f
$\dot{m}$	Mass flow rate
$\dot{V}$	Volumetric flow rate
ϵ	Roughness
η	Efficiency
μ	Dynamic or shear viscosity
μ_{JT}	Isenthalpic Joule-Thomson coefficient
Ψ	Potential energy term
ρ	Mass density
θ	Angle
υ	Kinematic viscosity
A	Area
c_p	Specific heat at constant pressure
c_v	Specific heat at constant volume
Ca	Cavitation number
d, D	Diameter
E	Energy
f	Generic function
f_c	Critical value of f
f_D	Darcy friction factor
g	Acceleration of gravity
H	Height, enthalpy
h	Specific enthalpy
h_c	Average heat transfer coefficient
K	Degrees Kelvin
k	Thermal conductivity
KE	Kinetic energy
L	Length
Nu	Nusselt number
P	Power

p	Pressure
p_{vap}	Vaporization pressure
PE	Potential energy
Pr	Prandtl number
Q	Rate of heat transfer
q	Heat flux
R	Thermal resistance
r	Radius
Re	Reynolds number
S	Shape factor
T	Temperature
t	Time, metric tonne
T_{vap}	Vaporization temperature
U	Internal energy
u	Speed, specific internal energy
V	Volume
v	Specific volume
Z	Compressibility factor
z	Depth
$°C$	Degrees centigrade

List of Figures

List of Tables

Introduction

1.1. Effects and consequences of anthropogenic emissions

Scientific research shows that global temperatures have risen during the last decades of the twentieth century - and the majority of scientists agrees that this is directly linked to the growing concentration of greenhouse gases in the earth's atmosphere [1]. This section presents a brief overview of the research on climate change caused by anthropogenic emissions.

1.1.1. History

In 1824, the French mathematician and physicist Joseph Fourier calculated that the earth's temperature should in fact be much lower than it actually is, given that solar irradiation was the only source of heat. While he attributed most of the excess heat to some form of interstellar irradiation, his argument that it is the earth's atmosphere that keeps the planet warmer than expected in the vacuum of space is generally acknowledged as the first step in exploring what would later become known as *the greenhouse effect* [2] [3].

By the late 1890s, the Swedish scientist Svante Arrhenius calculated that reducing the atmospheric CO_2 concentration by half would trigger an ice age, while doubling the CO_2 concentration would increase average global temperatures by 5-6 °C [4]. Together with his colleague Arvid Högbom, he was the first to predict the possibility of global warming caused by human emission of CO_2. While natural fluctuations in the atmosphere's CO_2 concentration and temperature are part of our planet's history and future, a stable greenhouse effect is critical to maintain life on earth [5] - and Arrhenius' and Högbom's findings show that large-scale anthropogenic emissions of CO_2 pose a threat to the global ecosystem: Even relatively small increases in mean global temperatures can have major consequences, such as weather pattern changes, intense local warming or cooling, ocean acidification and melting of glaciers. This can lead to drastic changes in ecosystems, fresh water availability and agricultural productivity [6].

The concentration of CO_2 in the atmosphere has risen from $537mg/m^3$ in 1750 to $775mg/m^3$ in 2015, with several measurement stations recording monthly averages above that last value since 2015 - an increase of over 45% [7]. This sharp increase in such a short period of time represents a clear disruption of the natural cycles over the past few million years and has largely been attributed to the combustion of fossil fuels [8]. Besides, after 2016 and 2015, 2017 was the year with the third-highest global land and ocean temperatures since observation recordings started in 1880 [9]. The magnitude of global temperature rises and the effects are still under heavy debate, but the general consensus is that further temperature increases should be minimized by reducing anthropogenic emissions, primarily of CO_2. Any CO_2 stabilization target above $872mg/m^3$ is associated with a significant probability of triggering a large-scale climatic event [10].

1.1.2. International agreements

Almost a century after Arrhenius' and Högbom's findings, 165 countries signed the UNFCCC of 1992, which states that the concentration of greenhouse gases in the atmosphere, among them CO_2, needs to be stabilized at a level that prevents dangerous anthropogenic interference with the climate system [11]. In 1995 the parties to the UNFCCC concluded the Kyoto Protocol in Japan, in which they committed to reduce their greenhouse gas emissions [12]. Coming into effect in 2005, the Kyoto Protocol was also the first treaty that specifically called for the developments of mechanisms and emission trading systems to curb the emission of greenhouse gases. The 2010 UNFCCC's Conference of the Parties in Cancún, Mexico, resulted in the agreement that, in order to avoid the dangerous consequences of climate change, the long-term global temperature should not rise more than 2 °C compared to pre-industrial levels [13].
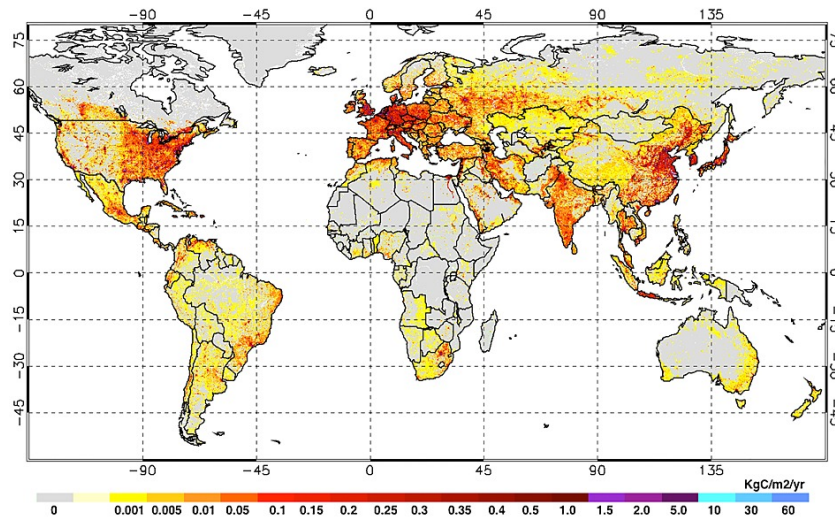
Figure 1.1: Global map of total CO_2 emissions from fossil fuels in $kg/m^2/year$ for 2010 [14]

The 2015 international agreement on climate change adopted in Paris represents a historic milestone: 176 states and the EU signed the agreement pledging to limit the global temperature increase to *"well below"* 2 °C and to *"pursue efforts"* to limit such increase to 1.5 °C. Furthermore, a balance between *"anthropogenic emission sources and removal by sinks"* - or net-zero emissions - is to be achieved by the second half of this century [15]. These commitments suggest a greater political willingness to address the challenges and to support the technologies that can reduce net emissions to zero. At the current rate, the anthropogenic emissions account for an annual net accumulation of 15 Gt of CO_2 into the atmosphere [10]. To put this number in perspective, the average annual CO_2 emissions from volcanic activity amount to about 0.3 Gt [16].

1.1.3. The way forward

In order to reduce anthropogenic emissions, drastic action is needed. So far, impressive progress has been made in clean energy technologies such as renewable energy sources (especially solar and wind energy), electric vehicles and large-scale energy storage. Still, these technologies currently represent only a small portion of the global energy system, and their pace of deployment needs tremendous acceleration if the goals set in the Paris Agreement are to be met, which requires vast amounts of money and resources and international cooperation.

Most studies agree that the most cost-efficient path to achieving sufficient emission reductions is an integrated approach that combines different technologies and developments, ranging from increased efficiency and use of renewable energy to Carbon Capture and Storage (CCS) [17] [18]. Since continued emissions from agricultural and industrial production processes seem inevitable in the foreseeable future, negative emission technologies and pro-

cesses like CCS will have to play an important role in reaching the desired balance between emission sources and sinks. In fact, to reach the goal of staying well below the 2 °C temperature increase, the IEA predicts that CCS will have to reach an annual storage capacity of 4.9 Gt by 2060 [18].

1.2. Carbon Capture and Storage

CCS is a generic term that describes different processes of capturing waste CO_2 from large point sources, preventing its release into the atmosphere. The CO_2 is captured, purified if necessary, then pressurized and transported to a suitable storage location, commonly a geological formation [19].

1.2.1. Capture

The capture of CO_2 accounts for the majority of the costs (70-90%) in the CCS chain and takes place at large point sources. Possible sources include fossil fueled power plants and industrial facilities in the production of iron, steel, cement and fertilizer [20]. Several capture technologies exist, which are generally divided into three groups [21]:

- **Post-combustion** capture technology extracts the CO_2 from exhaust gases of conventional facilities. Since typical flue gases have a low CO_2 concentration and are just above atmospheric pressure, the resulting low partial pressure favors liquid solvents for the chemical absorption of the CO_2 [22]. This technology is already used on a commercial scale in various places around the world

- **Pre-combustion** technology captures the CO_2 before the fuel is combusted: It includes a process to produce a synthetic gas (syngas) from the fuel, after which the resulting CO_2 is captured and the H_2 is used as carbon-free fuel or feedstock. The higher partial pressure of CO_2 makes it possible to use physical solvents for the capture process [23].

- **Oxy-fuel combustion** technology combusts the fuel with almost pure oxygen. This produces a stream of CO_2 and water, which are then separated [22]

In short, the goal of the capture part is to separate and purify the CO_2 stream. Although an industry-wide agreement on the required purity of the product flow has yet to be established, viable proposals generally range between 95 to 99% CO_2 content. The threshold is often determined by the type of impurity that can be handled by the equipment of the subsequent transport and storage sections [24].

1.2.2. Transport

Since the storage facilities are generally not located next to the involved emitting facilities, large quantities of CO_2 will have to be transported in a cost-efficient way. Transport of CO_2 is already done in many parts of the world, via pipelines, trucks, trains and ships. The main drivers for choosing the most efficient transport mode are the quantity, location and required flexibility. Pipelines are generally regarded as the most suitable mode of transport for large volumes of CO_2, that will be required for large-scale CCS projects [25] [26].

1.2.3. Storage

While the CO_2 itself is not toxic, high concentrations can cause asphyxiation [27]. Therefore, the primary risk management approach for any potential storage location is to minimize the possibility of future leaks over a long time. A second condition is that the storage location must present sufficient storage capacity: for a single coal-fired power plant that emits around $5Mt$ of CO_2 each year, the average 40-year lifetime emissions amount to over $200Mt$ of CO_2 [28]. Given that economies of scale predict that storage costs can be significantly reduced by combining CO_2 from various sources, the required capacity becomes a multiple of that number.

One of the few options that meets all these criteria is geological storage, which can be divided into three types:

- **Unmineable Coal Seams** Coal layers that are either too thin or at such depths that make them uneconomical to recover via current standard mining techniques. Because of the biological and geological conversion processes that take place in coal layers, they often contain large amounts of methane. Injection of CO_2 into these layers can displace the methane reserves, which can then be recovered [29]. The total storage capacity of CO_2 in unmineable coals seams is estimated at about $200Gt$ worldwide [30].

- **Deep Saline Aquifers** Carbonate and sandstone formations that are filled with saline water, which present the highest potential storage capacity for CO_2 in the world [31] [32]. In contrast to hydrocarbon reservoirs, aquifers are generally not well explored, so the actual amount of CO_2 that could be stored in aquifers is often uncertain. Global storage capacities have been estimated to range from 4000 to $23000Gt$ [30].

- **Depleted Hydrocarbon Reservoirs** These are generally regarded as very suitable storage locations because they once contained oil and natural gas for millions of years. Given the extensive research into their exploration, they are well studied and characterized, which makes estimations of their structure and capacity more accurate than those for coal seams or saline aquifers. At the same time, underground gas storage (UGS) has led to depleted hydrocarbon reservoirs being thoroughly investigated for their storage capacity, maximum injection rates and structural integrity [33]. Furthermore, enhanced oil and gas recovery (EOR & EGR) has produced valuable knowledge on carbon dioxide injection into reservoirs [32]. Their worldwide storage capacity is estimated at $1000Gt$ of CO_2 [30].

1.2.4. Potential impact of CCS

While acknowledging that most Carbon Dioxide Removal (CDR) technologies - including CCS - remain largely unproven to date, they are central to the mitigation pathways described in the newly released IPCC *Special Report on Global Warming of 1.5 °C* to limit global warming to 1.5 °C [34]. One reason why the technology has not been deployed on a large scale yet are the associated costs. Figure 1.1 shows that Europe is one of the major emitters of CO_2 in the world, particularly western Europe. Figure 1.2 presents a more detailed view of the continent's emissions, clearly showing that the countries in and around the Benelux area are responsible for a significant portion of European emissions [14].
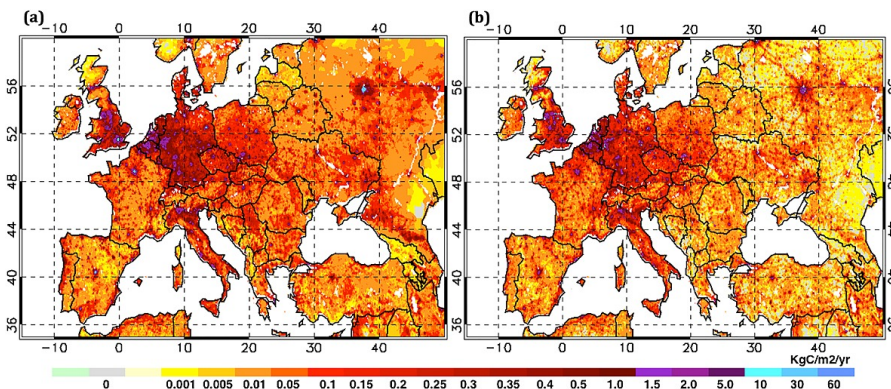
Figure 1.2: Overview of total CO_2 emissions from fossil fuels in kilograms per square meter per year on the European continent in 2010; power plant emissions are distributed by nightlights and population (**left**), and power plant emissions are allocated to the plant's locations (**right**) [14]

The Netherlands

The Netherlands emitted a total of $163Mt$ of CO_2 in 2017, which is almost equal to its emissions in 1990. Figure 1.3 clearly shows that most of the emissions are concentrated in small areas, especially around port areas, with the port of Rotterdam accounting for 17% of all Dutch emissions [35] [36]. Around 50% of all the CO_2 is emitted by around 400 companies that operate within the EU ETS, most of which are active in the energy industry. Of these 400 companies, around 40 (or 10%) are responsible for over 85% of the total CO_2 emissions.

Their proximity to port areas means that they are relatively close to depleted offshore reservoirs, which can serve as potential storage locations, so these areas offer a great opportunity to start large scale CCS and CCUS pilot projects [37].

Minder dan 5
5 tot 10
10 tot 20
20 tot 40
40 of meer
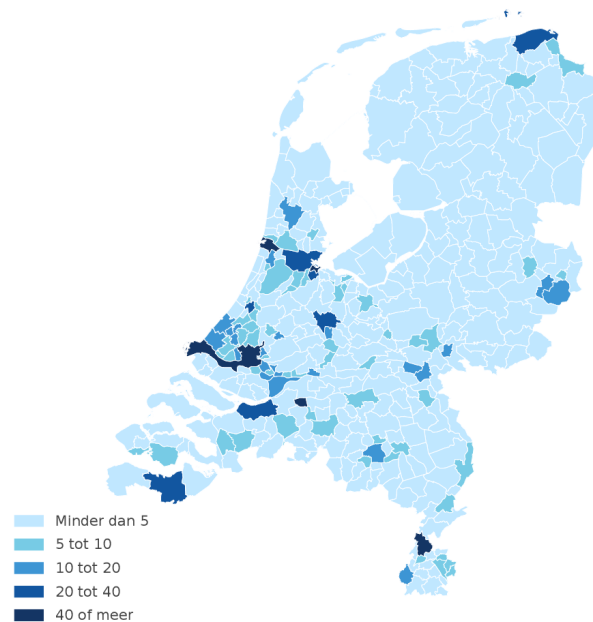
Figure 1.3: A map of the Netherlands showing CO_2 emissions in kilograms per square meter per municipality in 2016 [35]

The Netherlands already has some CCU experience with CO_2 in the gaseous phase, as the OCAP pipeline transports captured CO_2 from two facilities in the port of Rotterdam to the greenhouses in the Westland region. At a pressure of $1.6 - 2.2 MPa$, it supplies connected greenhouses with over $130kt$ of CO_2 per year through a repurposed 83 km oil pipe line between Rotterdam and Amsterdam [38].

In October 2017 the new Dutch cabinet announced its intentions to reduce greenhouse gas emissions by 49% until 2030, with respect to 1990 levels. Early roadmaps issued by the government indicated that $18Mt$ of CO_2 emissions were to be reduced through CCS until 2030, which translates into about $1.8Mt$ per year from 2020 onwards [39]. An updated analysis published in April 2018 has reduced this ambition to $7.2Mt$, or $0.72Mt$ per year from 2020 onwards [40].

1.2.5. Current policy framework

Surveys conducted by the Global CCS institute highlight that there is still insufficient policy certainty to support a business case for large-scale CCS projects. As these are capital intensive projects with long construction times, investors require long-term predictability before they are ready to invest in the development of CCS projects.

This means that strong and clear technology-neutral emission reduction policies are required on a global scale. An example of such a policy is the EU ETS, which was launched in 2005 as the first large greenhouse gas emissions trading scheme in the world [41]. However, with significant carbon price fluctuations over the past decade, the EU ETS still has serious shortcomings that make it difficult to produce reasonable and bankable estimations for future revenues.

In a consultation to the EC, the Global CCS Institute advises a *"structural reform of the EU ETS after the 2020 period to restore long-term confidence in the business case of CCS and achieve emission reduction targets"*, along with key policy observations and advice to realize these reforms [42].

1.3. Adoption of CCS

The first CO_2 capture technologies have been in use since the 1920s to separate CO_2 from natural gas. Since then, the basic technologies required for the CCS chain have been proven numerous times, and in some instances they have already been successfully demonstrated on a commercial scale.

1.3.1. Existing CCS projects worldwide

Some of the largest CCS projects worldwide are operated by the Norwegian oil and gas company Equinor (formerly Statoil), which has captured and stored over $20Mt$ of CO_2 to date from their Sleipner and Snøhvit gas fields, the 1996 Sleipner CCS project being the first commercial CO_2 injection project [43]. Furthermore, the joint venture that develops the Algerian onshore gas fields of In Salah, in which Equinor is also involved, has injected over $4Mt$ of CO_2 from 2004 to 2011 [44]. Another major initiative is the Quest CCS facility operated by Royal Dutch Shell in Canada, where $2Mt$ of CO_2 have been captured and stored since 2015 [45] [46]. The only project in the Netherlands where CO_2 is injected for storage is the K12-B gas field in the North sea.

1.3.2. Existing CCS projects in the Netherlands

While the Netherlands already contributed to European CCS research teams in the 1990s, the first national CCS research projects were undertaken under the CATO program set up in 2004. Research performed under the CATO umbrella covered the full CCS chain and addressed both fundamental and applied topics, including regulation, safety and public perception [47]. Although only one storage project has been realized to date, several initiatives already reuse captured carbon from industrial processes, the most well-known being greenhouses. An overview of projects initiated since 2004 is given below.

K12-B Gas field - *operational*
This is a natural gas field located approximately 150 kilometers northwest of Amsterdam, which is used for the first offshore carbon injection project in the Netherlands. While CO_2 has been separated from recovered natural gas since the start of production in 1987, it was not until 2004 that its operator Gaz de France started injecting it back into the depleted reservoir instead of venting it into the atmosphere. Since then, cumulative injection is estimated at over $100kt$ [48].

Barendrecht onshore storage - *canceled*
As part of a 2007 pilot initiated by the Dutch government, Royal Dutch Shell planned to inject captured CO_2 from its refinery in Pernis into two depleted gas fields near the city of Barendrecht, in what would have been the first application of onshore CO_2 storage. After fierce opposition by the local population, the project was canceled by the Dutch government in 2010 [49] [50].

ROAD project - *canceled*
The ROAD project was supposed to be the largest integrated CCS demonstration project in the world when it was initiated in 2009. The plan was to use post combustion capture technology to capture CO_2 from the flue gases of a new coal-fired power plant in the port of Rotterdam, which would then be transported 20 kilometers by pipeline to the P18 platform in the North Sea for injection into depleted gas reservoirs [51]. While the project was canceled by its initiators Engie and Uniper in 2017, the research on both the transport infrastructure and the P18 gas field as a storage location are being used in the new initiative PORTHOS, which is elaborated below [52].

Porthos - *in development*
PORTHOS is a joint initiative launched in 2018 by EBN, Gasunie and the Port of Rotterdam, who intend to develop the infrastructure for a port-wide CCUS project. It will consist of a pipeline network to collect CO_2 from different parties and a central temporary storage location. From there, part of it will be reused in the Dutch greenhouse sector, but most of it will be transported offshore for permanent storage [53] [54].

1.4. Offshore opportunities

Since the Oil crisis in the 1970s sparked the beginning of large-scale offshore exploration in the North Sea, the oil and gas industry in the surrounding countries has developed an extensive infrastructure, ranging from wells and platforms to processing and storage facilities - all connected by a complex network of pipelines. Most of this infrastructure is still in use to extract, process and transport fossil fuels, but once the fields are depleted, it is the industry's own responsibility to ensure that the decommissioning is executed in a safe and environmentally friendly way.

At the same time, developed countries face an enormous challenge to achieve the goals of reducing greenhouse gas emission set by international agreements, like the 2014 Paris agreement [15]. This means that their economies have to transition to a sustainable energy system and that polluters must take steps to reduce their emissions. Repurposing parts of the vast offshore infrastructure might offer some unconventional possibilities to help curb anthropogenic emissions.

1.4.1. Energy Storage

Platforms in the vicinity of offshore wind turbine fields could be retrofitted with power-to-gas facilities; when electricity supply exceeds demand, the excess can be used to generate hydrogen through electrolysis. With molecules being a more efficient energy carrier than electrons, the hydrogen can either be transported to shore through existing natural gas pipelines, or stored in depleted reservoirs first to serve as an energy storage mechanism. While research has shown that hydrogen can be safely transported through conventional natural gas pipelines, its smaller molecule size makes it much harder to contain: In contrast to CO_2, hydrogen remains mobile through the cap rock of common gas reservoirs and will eventually escape [55].

Since investment costs of long offshore pipelines are considerably lower than equally long electricity cables, the extra costs of installing offshore electrolysers and their efficiency losses will be offset outside a certain range. This suggests that the main market for offshore power-to-gas facilities will be as part of long distance offshore wind farm initiatives [56] [57].

1.4.2. Carbon Storage

Another option is to reuse the pipeline infrastructure to transport CO_2 from the shore and use the support structure to mount a conditioning module before injecting the CO_2 into depleted fields. Simultaneously, unused parts of the infrastructure can be decommissioned.

1.5. MSc thesis research project

This graduation research project is the final part of the Master of Science program in Mechanical Engineering at Delft University of Technology and intends to demonstrate that the author has achieved the required academic level. It is an individual in-depth research project, supervised by a qualified member of the faculty and conducted in cooperation with an external party, Heerema Marine Contractors (HMC).

1.5.1. Client - Heerema Marine Contractors

HMC is a world-leading marine construction company that mainly operates within the oil, gas and renewable energy industry. It owns and operates a fleet of vessels, including the worlds largest semi-submersible crane vessel Thialf, and is specialized in the design, transportation, installation and removal of all types of fixed and floating offshore structures and infrastructures in both shallow and deep water.

1.5.2. Assignment description

Since many of the North Sea platforms that were constructed in the last decades are approaching the end of their prospected lifetime, decommissioning will be a growing market within the offshore industry.

One of the initiatives to employ HMC's capabilities for CCS initiatives involves a concept for the temporarily continued use of part of the offshore facilities of abandoned natural gas fields, like the support structure and the pipelines, by integrating them into the CCS chain. In this new concept, the existing extraction and production facilities are to be replaced by a new module that is specifically designed to condition and inject CO_2 into the depleted field below. The working title for this new module is CaStor (Carbon Storage). The hypothesis is that the high costs of offshore carbon storage can be brought down significantly and become competitive with traditional offshore CCS initiatives by reusing the existing pipeline infrastructure for carbon transport and the support structure for the installation of the CaStor module.

The overall goal of this thesis is to determine the feasibility of the CaStor concept by developing a comprehensive method for HMC to assess the techno-economic feasibility of reusing abandoned natural gas fields and their infrastructure for carbon storage.

1.6. Research questions

This thesis focuses on the physical transport phenomena along the transport and storage chain. It investigates how the reservoir parameters change the configuration and results in a conceptual design of an injection module. To give an impression of the expenses associated with the CaStor module, a cost estimation will be included in the appendix. More precisely, the following research questions were explored:

1. What are the dominant transport phenomena along the transport and storage chain?

2. What are the conditioning steps the CO_2 must undergo before injection?

3. How do different infrastructure and reservoir properties affect the requirements of the conditioning steps?

4. What is the configuration, size and energy consumption of a CaStor module?

	Chapter 2	Chapter 3	Chapter 4	Appendix
RQ1		x	x	
RQ2	x	x		
RQ3		x	x	
RQ4			x	x

Table 1.1: Overview matrix of the research questions and chapters in which they are addressed

1.7. Outline of the thesis

The thesis starts with a literature study in chapter 2 that explores the properties of CO_2 and subsequently reviews the current state of academic knowledge on its behavior during transport and storage. The findings are then used to define the first set of assumptions and the boundary conditions.

The method is presented in chapter 3: First, a conceptual overview of the computer model is explored. Next, the the governing equations are set, after which the dominant transport phenomena for each section are determined and discussed how they integrate into the model. Each section then starts with its specific set of assumptions, followed by how the boundary conditions are substituted to conduct the different testing scenarios. The outcome of each section is analyzed separately in the results section in chapter 4, followed by a comprehensive analysis for the test case.

Chapter 5 discusses how the hypothesis has been demonstrated by the new research and contextualizes these findings in the general field. The concluding remarks are presented in chapter 6.

The accuracy of the model's results is verified with different methods in appendix A. Appendix B contains a simplified analysis of the current economic and policy challenges governing large scale CCS initiatives, along with a raw estimate for the business case of the CaStor module. In appendix C, the results are used to come up with the conceptual design plan of a CaStor module, along with an approximation of its size and weight, two important parameters for HMC.

1.7.1. Units of measurement

The units of all physical variables can be expressed in terms of the units of four basic variables; *length*, *mass*, *time* and *temperature*. This thesis used the international system of units, commonly reffered to as SI. These basic units, along with other units used in this thesis, are listed in table 1.2.

Quantity	Name of unit	Symbol	Equivalent
Length	Meter	m	
Mass	Kilogram	kg	
Time	Second	s	
Temperature	Kelvin	K	
Force	Newton	N	$kg\ ms^{-2}$
Pressure	Pascal	Pa	$N\ m^{-2}$
Energy	Joule	J	$N\ m$
Power	Watt	W	$J\ s^{-1}$

Table 1.2: Overview matrix of the SI units used in this thesis

Strict adherence to the SI system can be inconvenient and will occasionally be abandoned; a temperature might be expressed in degrees Celcius (°C), which is related to Kelvin (K) by the relation °C $= K - 273.15$. Time scales might be expressed in hours (3600 s) or days ($86.4 \cdot 10^3\ s$).

To avoid very small or very large numbers, prefixes are used to indicate multiples of respective units. Some of the common prefixes are listed in table 1.3.

Prefix	Symbol	Multiple
Giga	G	10^9
Mega	M	10^6
Kilo	k	10^3
Milli	m	10^{-3}
Micro	μ	10^{-6}

Table 1.3: Prefixes used in this thesis

2

Literature study

2.1. Properties of CO_2

Both the triple point and the critical point of pure CO_2 are defined by a pressure and a temperature and are shown in figure 2.1. The triple point is found at a pressure of approximately 0.51 MPa and a temperature of 216.45 K and defines the point where the gas, solid and liquid phases can coexist in thermodynamic equilibrium.
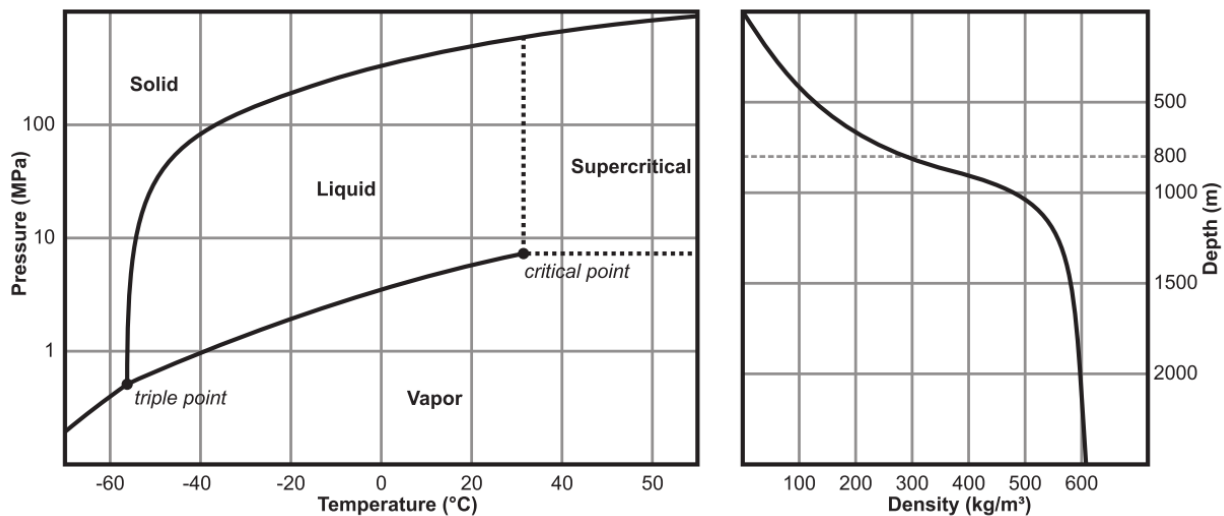
Figure 2.1: **Left:** The phase diagram of pure CO_2 as a function of temperature and pressure. Above the critical point ($\sim$ 31°C and 7.4 MPa), CO_2 becomes supercritical, which is most suitable for geological storage. **Right:** The density of CO_2 as a function of depth. At a depth of approximately 800m, the increase in geothermal temperature and hydrostatic pressure initiates a stable transition to the supercritical phase [58].

The critical point lies at a pressure of approximately $7.38 MPa$ and a temperature of $304.2K$. Above the critical point, the gas and liquid phases cannot coexist as separate phases anymore, so the CO_2 develops supercritical properties. This means that it will behave like a gas, while its density is common to a liquid, and there is no distinction anymore between the liquid and gas phase. Supercritical CO_2 offers a number of advantages as it can effuse through solids like a gas and dissolve materials like a liquid. These properties greatly increase the storage capacity of potential storage reservoirs [59].

2.1.1. Density

A crucial parameter in the calculations performed in this thesis is the density of the transport medium. Figure 2.1 indicates that the temperature and pressure dependence of the density of CO_2 changes with increasing depth. A plot of the density of pure CO_2 at relevant temperatures and pressures is shown in figure 2.2. A closer look reveals that the density becomes more temperature-dependent at lower temperatures and as the pressure increases. Also, the density shows to be very sensitive to temperature changes around the critical point, which is defined in section 2.1.
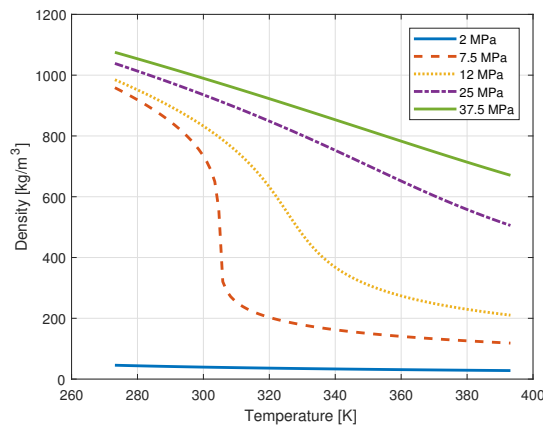
Figure 2.2: Density of pure CO_2 as a function of temperature and pressure relevant for this thesis [60].

2.1.2. Viscosity

The viscosity plays a central role in determining the flow behavior of a fluid near solid boundaries. In simple terms, viscosity can be described as the friction between the molecules of a fluid. Just like density, viscosity shows a strong temperature dependence, especially near the critical point. Compared to other fluids, pure CO_2 has a relatively low viscosity: At $T = 293.15\ K$ and $P = 2\ MPa$, water and ethanol have a viscosity of $10 \cdot 10^{-4}\ Pa \cdot s$ and $12 \cdot 10^{-4}\ Pa \cdot s$, respectively, whereas that of CO_2 is $1.6 \cdot 10^{-4}\ Pa \cdot s$.
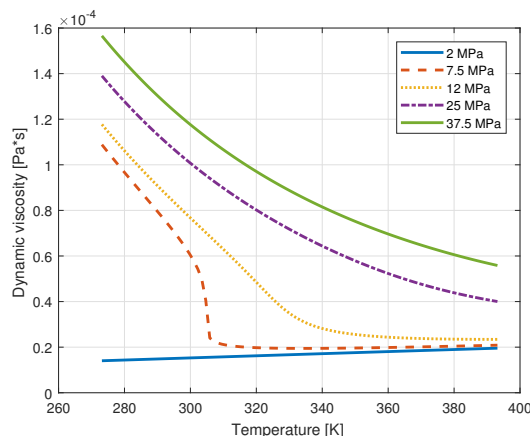
Figure 2.3: Dynamic viscosity of pure CO_2 as a function of temperature and pressure [60].

2.1.3. Compressibility factor

The compressibility factor is a corrective factor that describes the deviation of real gas behavior from ideal gas behavior. The deviation increases for heavier gases as their molecules are larger [61]. Figure 2.4 shows a plot of the compressibility factor z based on data from

the NIST's database for pure CO_2 at conditions relevant for this thesis. While an ideal gas has a z-factor of one, the graph shows that z-factor of CO_2 ranges from below 0.2 to 0.95, which suggests a strong deviation from ideal gas behavior at lower temperatures. It is this low z-factor, combined with the high molecular weight, that makes the density and viscosity of CO_2 so temperature dependent. The low z-factor implies that CO_2 cannot be assumed to behave like an ideal gas in the relevant pressure and temperature ranges.
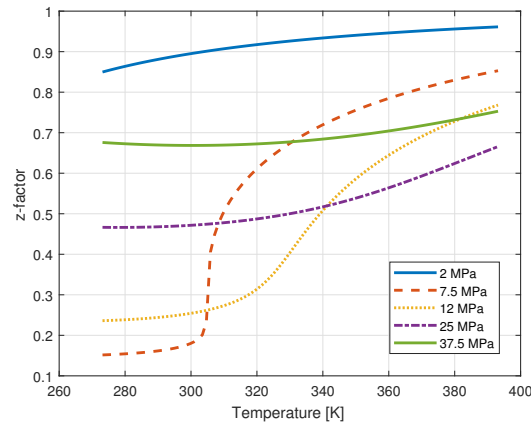
Figure 2.4: Compressibility factor (z-factor) of pure CO_2 as a function of temperature and pressure [60].

2.1.4. Specific heat capacity

Heat capacity is a measurable physical quantity that is defined as the amount of heat energy that is required to raise the temperature of a substance by one degree [62]. The specific heat capacity is the heat capacity per unit mass.

For single-component systems, the specific heat capacities at constant volume and constant pressure are defined as follows:

$$c_v \equiv (\frac{\partial u}{\partial T})_V , \ and \ \ c_p \equiv (\frac{\partial h}{\partial T})_p \tag{2.1}$$

This means that specific internal energy u and specific enthalpy h are regarded as functions of V, T and p, T, respectively. While figure 2.5 shows that both c_v and c_p display a strong temperature dependence around the critical pressure, they remain almost constant the further they are away from the critical point.
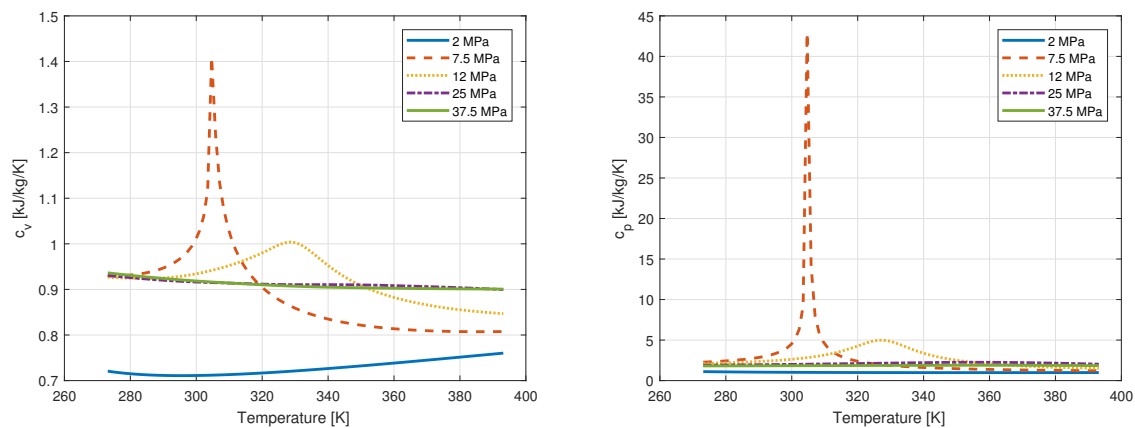
Figure 2.5: The specific heat capacity of pure CO_2 at constant volume (left) and at constant pressure (right), both as a function of temperature and for different pressures [60]

2.1.5. Transport behavior

Given its thermodynamic properties, CO_2 can either be transported as a gas, a liquid, in supercritical state or as a mixture of gas and liquid phase (also known as two-phase flow), depending on the temperature and pressure of the medium. While gaseous transport occurs at a pressure of up to 4 MPa, liquid phase transport requires a minimum pressure of 5 MPa at a temperature of 283 K. Supercritical flow requires a pressure that exceeds 7.3 MPa and a temperature above 304.2 K, as shown by the critical point in figure 2.1.

Generally, CO_2 is moved in the liquid or supercritical phase. The resulting low viscosity and high density allow for the transport of large amounts of CO_2, with minimum friction losses [63]. Two-phase flow, on the other hand, should be avoided if possible, as it results in cavitation, which damages the equipment. Two-phase flow also makes the use of compressors and pumps much more difficult, reducing the amount of CO_2 that can be transported and increasing costs compared to the liquid and supercritical transport [64].

2.1.6. Injection & storage behavior

For maximum storage efficiency, the CO_2 should enter the reservoir in the supercritical phase. This ensures a quick and gas-like effusion through the porous reservoir rock, while the density remains close to that of a liquid, resulting in a high mass transfer rate. The pressure and temperature inside the reservoir are commonly well above the critical point described in section 2.1, so once the CO_2 reaches the supercritical phase during injection, it will remain stable. In some instances, however, Joule Thomson-related cooling due to the abrupt expansion in the reservoir might lead to the formation of solid phase CO_2, significantly reducing the permeability of the rock formation [33].

2.1.7. Effect of impurities & flow composition

Depending on the method used to capture CO_2 from industrial processes, it will contain a certain level of impurities that can affect the behavior of the mixture at a given pressure and temperature, for example by altering the critical point. This has an effect on the system as a whole, as it might require different conditions for the CO_2 to remain in a certain phase. Furthermore, impurities can also influence corrosion-related performance, which can increase investment costs. Depending on the employed capture and separation technology, the output quality of CO_2 in large-scale CCS applications ranges between 95 and 99.9 % [65] [66]. Since the goal of this thesis is to present a conceptual overview of the transport and storage chain, a CO_2 quality of 100% is assumed.

2.2. General Assumptions

Since industrial processes continuously emit CO_2, its capture and compression must be continuous, too. This implies that the mode of transport to the storage facility should ideally be continuous as well, to minimize bottlenecks along the chain. It is therefore assumed that pipelines are the preferred option.

As mentioned in section 1.2.4, most of the companies that operate under the EU ETS umbrella are located in the vicinity of port areas. This means that transport distances are relatively small, which makes transport to a central storage location in the gas phase the preferred option. This thesis uses the PORTHOS project in Rotterdam [53] as a blueprint: A network of small pipelines that transport the captured CO_2 from industrial installations to a central compression and storage station close to shore. From there, the CO_2 has to be transported to a permanent storage location.

2.2.1. Offshore transport

EBN and GasUnie have established a national framework for the transport of CO_2 through pipelines: Short onshore distances are to be undertaken in the gas phase at 2 MPa and the limit for offshore transport to permanent storage locations is set at 10-12 MPa in the liquid phase. This pressure is realized by central compressing stations along the coast, which collect CO_2 from different sources and maintain a buffer to ensure a buffer of CO_2 [49] [67]. These conditions will be used as input parameters in this thesis.

2.2.2. Conditioning steps

To achieve maximum storage efficiency, the liquid CO_2 must undergo some conditioning steps to become supercritical: Its pressure, which is already above the critical threshold, must be further increased to exceed the reservoir pressure. Furthermore, the temperature must be increased to surpass the critical temperature.

Figure 2.6 shows a pressure-enthalpy diagram for pure CO_2, which can be used to estimate how the substance properties change due to a change in pressure or energy along certain thermodynamic paths. For instance, the steep isentropic lines in the liquid region indicate that the energy input required to increase the pressure is relatively low compared to the energy required in the vapour region.

The two main thermodynamic paths of the transition from the liquid to the supercritical region at a desired reservoir pressure are depicted in figure 2.6.

(a) In this path, a heating stage is followed by a compression stage.

(b) In this path, compression to the required injection pressure is followed by a heating stage.
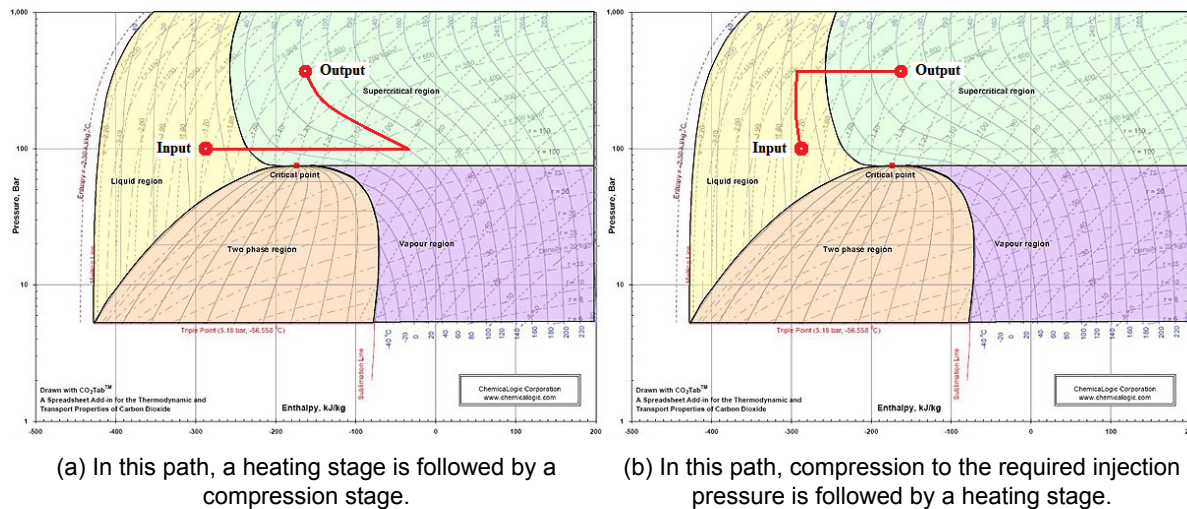
Figure 2.6: The Mollier diagrams (Pressure-Enthalpy) for CO_2 with the two different possible thermodynamic paths [68].

The Mollier diagrams show that configuration (a) results in a much larger enthalpy difference than the path chosen in (b). Since the CO_2 is already in the supercritical phase if heated first, a compressor must be used to increase the pressure instead of a pump, even though the latter is much more efficient. Furthermore, putting a heater first leads to a higher risk of cavitation in sequential conditioning steps as the temperature is closer to the boiling point. Therefore, the energy required to reach the output conditions is much higher for path (a), which is why it will not be further considered during this thesis.

2.2.3. Storage capacity

The principal assumption used in this thesis is that a depleted or partially depleted gas field can be refilled with CO_2 up to its initial pressure. This assumption is based on the argument that the reservoirs have proven their sealing capacity by containing natural gas at this pressure for geological time scales [69]. Research shows that the expected storable volume of CO_2 is more than 90% of the total recovered volume of natural gas [33]. For this reason, all capacity calculations in this thesis simply convert recovered natural gas reserves to an equivalent tonnage of storable CO_2.

2.3. Boundary conditions

This section establishes and summarizes the boundary conditions used to compile the model for the planned CO_2 transport and storage chain off the coast of Rotterdam.

2.3.1. Overview

The CO_2 is received in the liquid phase through the pipeline that connects the storage location to shore. Once at the platform, the CO_2 will undergo the required conditioning steps, after which it is injected through the well pipe, where it becomes supercritical.
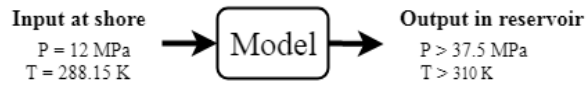
Figure 2.7: The input and output conditions for developing the model

Since the injected CO_2 will be heated by geothermal energy while it travels down the well, the auxiliary heater only plays a complementary role: Should the geothermal heating fall short of reaching the critical temperature, the heater will bridge the gap. It is therefore assumed that the solution remains in the liquid phase until it travels down the well, where it gradually transitions to the supercritical phase.

2.3.2. Storage location

Two locations that have been found to be suitable for long-term storage of CO_2 are the P15 and P18 fields [70]. P15 and P18 refer to a group of natural gas reservoirs located around 30km north-west of the Hague that are connected to the Maasvlakte port area by means of a 40km long 66cm-diameter pipeline. Since this steel pipeline was installed in 1989 [71], it is assumed to have moderate rust development, which results in an estimated roughness of 0.25 mm [72].
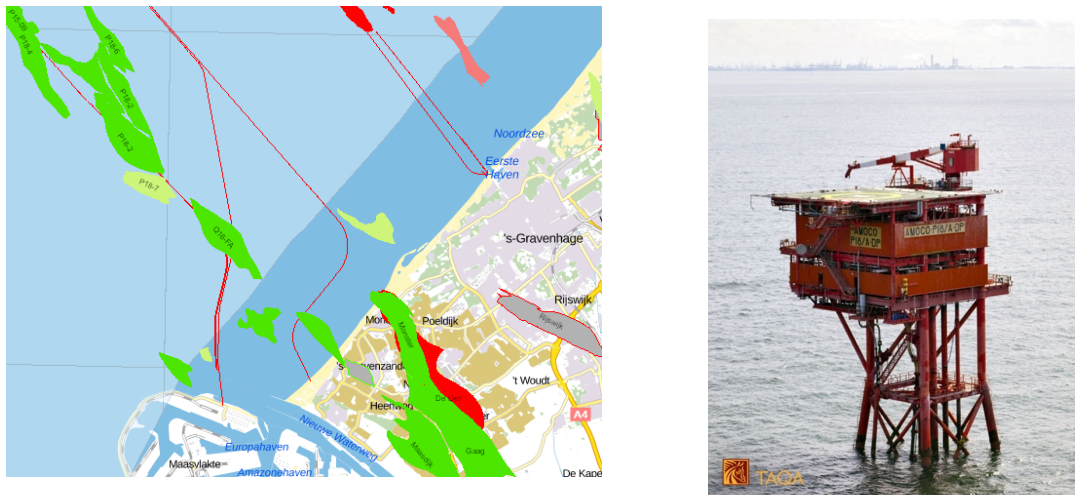
Figure 2.8: **Left:** the location of the P15 and P18 gas fields (the green areas in the upper-left corner) north-west of the Hague and the pipeline that connects them to Rotterdam's port area (the red line on the left) **Right:** a picture of platform P18A [71]

Reservoir/platfrom	Initial pressure [MPa]	Current pressure [MPa]	Est. storage capacity [Mt]
P18-4 / P18-A	34	2	8
P18-2 / P18-A	37.5	2	32
P15-9 / P15-E	34.7	2	10
P15-13 / P15-G	28.8	3.5	8
P15-11 / P15-F	28.3	1.5	16

Table 2.1: Total storage capacity of P15 & P18 gas reservoirs [70] [73]

Together, the P15 and P18 fields present a potential storage capacity of $74Mt$, as shown in figure 2.1. On top of that, nearby aquifers are currently evaluated for additional storage capacity.

The wells of P18-2 and P18-4 both connect to platform P18-A, shown in figure 2.8. Since the P18-4 reservoir is the first location to receive a permit for commercial offshore CO_2 storage, its properties will be used as a reference to model the injection and storage in this thesis. However, because of its limited storage capacity, P18-4 is designated as proof of concept only to test the technologies. The much bigger P18-2 reservoir is also set to receive a permit soon, and because of the well's similarities to P18-4, its properties will be used to determine the model's boundary conditions.

The reservoirs are modeled as spherical tanks that are top-filled through the connected well pipe, as shown in figure 2.9. Using the relationship between pressure, temperature and density of the initial content, the volume of the equivalent tanks and the mass inside is determined.

The pressure at which the solution must enter the injection well depends largely on the reservoir's depth, as the static pressure at the bottom of the injection column will cause a large overall pressure increase before the solution enters the reservoir.

		P18-2	P18-4
Reservoir depth	$[m]$	3598	3440
Initial pressure	$[MPa]$	37.5	34
Current pressure	$[MPa]$	2	2
Temperature	$[K]$	393	393
Max. injection rate	$[\frac{kg}{s}]$	350	350
Est. storage capacity	$[Mt]$	32	8
Well pipe diameter	$[m]$	0.1	0.1
Equivalent tank diameter	$[m]$	458.36	288.7
Equivalent tank volume	$[m^3]$	$5.042e^7$	$1.26e^7$
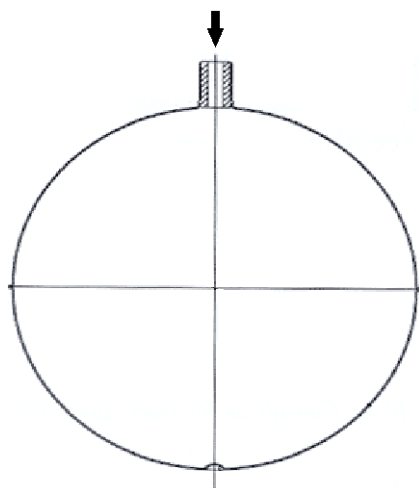
Figure 2.9: The reservoir is modeled as a spherical tank with a well pipe connected to the top

Table 2.2: Reference properties of both reservoirs modeled as spherical tanks [70]

Both pressure and temperature are assumed to behave as linear functions of depth towards the earth's interior. Literature commonly couples the conditions at a certain depth with the geothermal gradient and hydrostatic pressure gradients shown in table 2.3 [58].

Geothermal gradient	0.035	$[K/m]$
Hydrostatic pressure gradient	0.01	$[MPa/m]$

Table 2.3: Overview of the gradients used in the model [74] [75]

<div align="right">

3

</div>

Method

This chapter presents the method used to simulate the transport and storage chain. Using the findings from the literature study, the structure of the conceptual model is described. Next, the governing equations and the governing thermodynamic and fluid dynamic concepts that are used to identify the dominant physical transport phenomena are explained, along with how they are integrated into the model's configuration. Last, the mathematical solution procedure is discussed.

3.1. Structure of the conceptual model

Combining the input and output conditions summarized in figure 2.7 with the assumptions set out in the previous chapter, a conceptual model is compiled as shown in figure 3.1 on the next page.

Fundamental input parameters

Besides the inflow conditions at the beginning of the transport pipeline, the model uses a set of fundamental input parameters, derived from the information in section 2.3.2, that describe the infrastructure and reservoir characteristics. These parameters are shown in table 3.1 below.

	d_{pipe}	$[m]$	inside pipe diameter
	ϵ	$[m]$	pipe roughness
Pipeline	l_{pipe}	$[m]$	total length
	H_{pipe}	$[m]$	depth relative to seabed
	$T_e\ (T_{soil} \sim T_{sea})$	$[K]$	avg. outside temperature
	d_{well}	$[m]$	well pipe diameter
	z	$[m]$	depth
Reservoir	d_{tank}	$[m]$	tank diameter
	p_{res}	$[MPa]$	Current reservoir pressure
	p_{max}	$[MPa]$	Maximum reservoir pressure

Table 3.1: Overview of the fundamental input parameters, for the reservoir modeled as a spherical tank
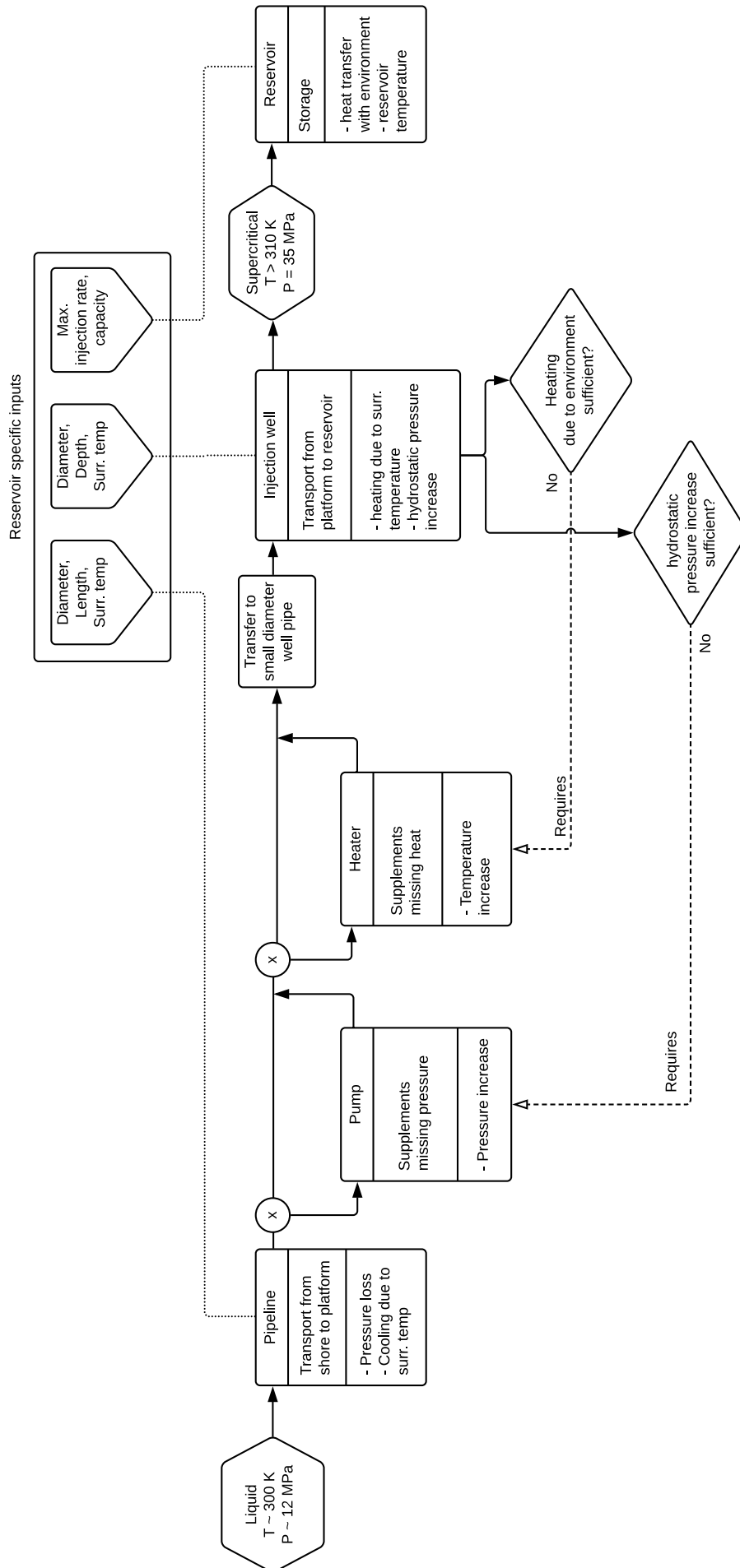
Figure 3.1: A schematic diagram of the simulation model

3.1.1. Configuration scenarios

Every scenario incorporates the same transport phenomena laid out in chapter 3, but uses different reservoir characteristics to simulate varying pressure- and temperature changes along the way.

Scenario 1 - No auxiliary equipment

In the first scenario (Figure 3.2), the reservoir characteristics are such that neither an auxiliary pump nor a heater are required for the medium to reach the supercritical state at the required injection pressure prior to entering the reservoir. This means that the static pressure at the bottom of the well pipe is sufficient and that enough heat energy from the formation is transferred through the well pipe into the CO_2.
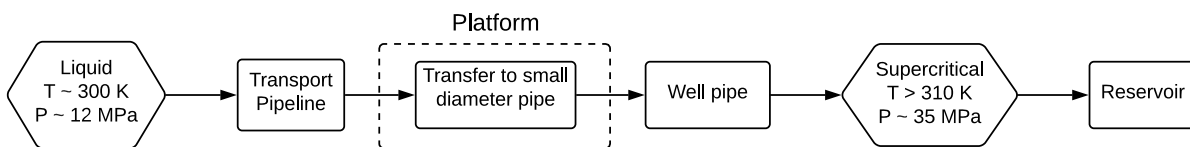
Figure 3.2: Schematic diagram of scenario 1, where no auxiliary equipment is required

Scenario 2 - Heater only

In the second scenario (Figure 3.3), the reservoir is deep enough to reach the required injection pressure solely through the static pressure build-up, but the heat transfer from the environment to the CO_2 is not sufficient to reach the critical temperature. A heater will be required to supplement the missing heat to ensure the solution enters the well pipe at a higher temperature, facilitating the timely transition to the supercritical phase by geothermal energy.
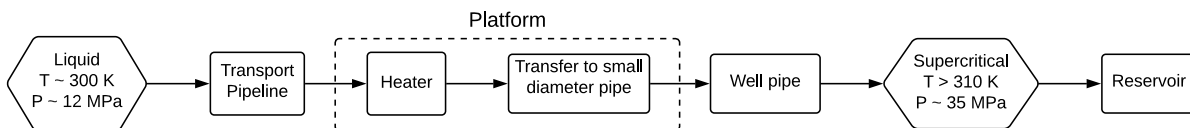
Figure 3.3: Schematic diagram of scenario 2, which includes a heater

Scenario 3 - Pump only

In the third scenario (Figure 3.4), the heat transfer from the surrounding rock is sufficient to reach the critical temperature, but the static pressure build-up is not enough to overcome the reservoir pressure. This means that a pump will be used to increase the pressure of the medium prior to entering the injection well.
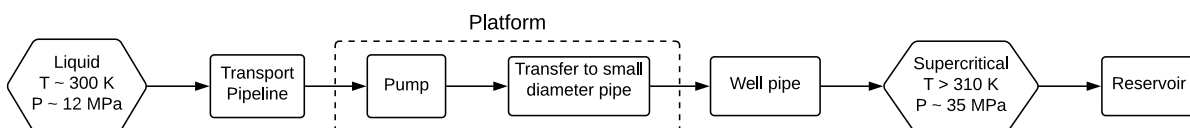
Figure 3.4: Schematic diagram of scenario 3, which includes a pump

Scenario 4 - Pump & Heater

In the last scenario (Figure 3.5), neither the heat transfer from the surrounding rock, nor the pressure build-up from the static pressure are sufficient to reach the required injection conditions. Both a pump and a heater will be required to increase the medium's temperature and pressure prior to entering the injection well.

Platform
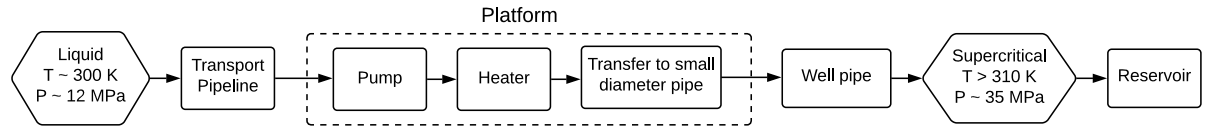
Figure 3.5: Schematic diagram of scenario 4, which includes both a pump and a heater

3.2. Governing equations

The calculations in this thesis are derived from three governing equations that describe dependent variables when independent variables change. The continuity equation and energy equation are mathematical statements which are based on two fundamental physical principles: the *Conservation of mass* and the *Conservation of energy*. On the other hand, the equation of state is the product of a complex set of correlations.

3.2.1. Continuity equation

The integral form of the mass conservation principle imposed on a control volume results in the following equation:

$$\frac{d}{dt} \iiint_{CV} \rho dV = - \iint_{CS} \rho \underline{u} \cdot \hat{n} dS \tag{3.1}$$

Where the left side represents the change in total mass inside the CV and the right side how much volume passes the surface of the CV. Here ρ is the density of the fluid, V the volume, $\underline{u}$ the velocity vector and $\hat{n}$ is the normal vector of control surface S. This can then be rewritten in the differential form, resulting in the continuity equation:

$$\frac{\partial \rho}{\partial t} + \underline{u} \cdot \underline{\nabla} \rho + \rho \, \underline{\nabla} \cdot \underline{u} = 0 \tag{3.2}$$

Where $\underline{\nabla}$ is the gradient. If the flow is incompressible, meaning ρ is constant throughout the flow field, the material derivative becomes zero, after which the equation can be simplified to

$$\underline{\nabla} \cdot \underline{u} = \frac{\partial u}{\partial x} + \frac{\partial v}{\partial y} + \frac{\partial w}{\partial z} = 0 \tag{3.3}$$

Where u, v and w are the flow velocities in the x, y and z direction.

3.2.2. Energy equation

The first law of thermodynamics implies that energy is conserved over a control volume (CV), and that the only way it can be changed is through the transfer of energy by work, by heat or through the inflow and outflow of mass. The time rate form of the overall energy balance over a CV of an open system can be described as the sum of the time rate of change in *Kinetic Energy*, *Potential Energy* and *Internal Energy*:

$$\frac{dE}{dt} = \frac{d\mathrm{KE}}{dt} + \frac{d\mathrm{PE}}{dt} + \frac{dU}{dt} \tag{3.4}$$

This can be rewritten in a form that is more convenient for the systems encountered in this thesis:

$$\frac{dE}{dt} = \dot{Q} - \dot{W} + \sum \dot{m}_{in}(h_{in} + \frac{1}{2} \cdot u_{in}^2 + \Psi_{in}) - \sum \dot{m}_{out}(h_{out} + \frac{1}{2} \cdot u_{out}^2 + \Psi_{out}) \tag{3.5}$$

Here $\dot{Q}$ and $\dot{W}$ represent the rate of energy transfer by heat transfer and work, respectively. The mass flow rate is denoted by $\dot{m}$, the enthalpy by h, the flow velocity by u and Ψ represents the potential energy term. Assuming a steady state, the first law can be further reduced to:

$$\sum \dot{m} \cdot \Delta(h + \frac{u^2}{2} + \Psi) = -\dot{Q} + \dot{W} \tag{3.6}$$

As will be explained in section 3.4.2, the potential energy term $\Psi = g \cdot z$ only plays a role during injection, when the medium travels down the well into the depleted reservoir. Else, the potential energy term is relatively small compared to the enthalpy terms, so equation 3.5 can be further reduced to

$$\sum \dot{m} \cdot \Delta(h + \frac{u^2}{2}) = -\dot{Q} + \dot{W} \tag{3.7}$$

In terms of specific quantities, the enthalpy per unit mass can be defined as

$$h = u + pv = u + \frac{p}{\rho} \tag{3.8}$$

Where u is the specific internal energy, p the pressure and v the specific volume.

3.2.3. Equation of state

An equation of state (EOS) is used to describe the properties of fluids, gases, mixtures and solids. It relates state variables such as pressure, volume and temperature to each other by means of a thermodynamic equation [76]. The simplest and most well-known EOS is the ideal gas law, which is accurate for weak polar gases at modest temperatures and slightly polar gases; it was first stated by Émile Clapeyron in 1834 [77] and is shown in equation 3.9.

$$pV = nRT \tag{3.9}$$

Where V is the volume, n represents the amount of moles, R the universal gas constant and T the absolute temperature. Since the ideal gas law becomes more and more inaccurate as temperatures decrease or pressures increase and fails to forecast phase transitions, a number of alternative EOSs has been developed, none of which can correctly predict the characteristics of all substances under all circumstances.

As described in section 2.1.3, the compressibility factor suggests that CO_2 shows a strong deviation from ideal gas behavior in the relevant pressure ranges. To prevent a discussion on the accuracy of the end result of the real-gas model based on the EOS of choice, the decision was made to use REFPROP, a program developed by the NIST. REFPROP provides tables and plots of thermodynamic and transport properties of different pure fluids and mixtures and is based on the most accurate models currently available, including different EOSs explicit in Helmholtz energy, the modified Benedict-Webb-Rubin EOS and an extended corresponding states model [78].

3.3. Governing thermodynamic and fluid-dynamic concepts

To describe the physical transport phenomena along the transport and storage chain, a set of thermodynamic and fluid-dynamic concepts are used to determine accurate assumptions. Table 3.2 depicts a matrix of the sections and the concepts employed to describe the system behavior.

	Transport pipe	Pipe convergence	Well pipe	Injection
Flow regime	x	x	x	
Modes of heat transfer	x	x	x	x
Lumped capacity model	x		x	
Phase transition			x	
Cavitation		x		
Joule-Thomson effect				x

Table 3.2: Overview matrix of the different sections of the transport and storage chain, along with the dominant thermodynamic and fluid-dynamic concepts

3.3.1. Flow regime

The flow regime is predicted using the Reynolds number, the dimensionless quantity shown in equation 3.10. It gives an indication of when a flow ceases to be smooth and steady (*laminar*) and becomes fluctuating and agitated (*turbulent*).

$$Re = \frac{inertial\ forces}{viscous\ forces} = \frac{\rho u L}{\mu} = \frac{uL}{v} \qquad (3.10)$$

Here L is the characteristic length and μ and v represent the dynamic and kinematic viscosity, respectively. Turbulent flow is inherently unsteady because both velocity and pressure are characterized by time-dependent fluctuations. These fluctuations are usually averaged to time-smoothed velocities and pressures, so that they become time-dependent on a time scale that is much larger than that of the fluctuations and can therefore be assumed to be steady [79] [80].

0	$< Re <$	1	*laminar*, highly viscous "creeping" motion
1	$< Re <$	100	*laminar*, strong Reynolds number dependence
100	$< Re <$	10^3	*laminar*, boundary layer theory useful
10^3	$< Re <$	10^4	*transition* to turbulence
10^4	$< Re <$	10^6	*turbulent*, moderate Reynolds number dependence
10^6	$< Re <$	∞	*turbulent*, slight Reynolds number dependence

Table 3.3: Approximate ranges of the Reynolds number and the dependency of the corresponding flow regimes in a pipe [81]

Initial calculations using the pipe diameters and the mass flow rate have shown that the Reynolds number exceeds 10^6 over the whole chain, meaning the flow is fully turbulent.

The heat transfer rate in turbulent flow is much higher because of additional transport mechanisms in the radial and azimuthal directions, a phenomenon commonly referred to as "eddy transport". Because of this intense transverse transport of energy, all heat transfer is assumed to take place in the fully developed region and the thermal entrance region is

neglected. Mills recommends to assume fully developed conditions for any situation where $\frac{L}{D} \geq 60$ [82].

3.3.2. Modes of heat transfer

While there are four fundamental modes of heat transfer (*advection, conduction/diffusion, convection* and *radiation*), Mills recommends to categorize them in three subject areas for engineering purposes: *Heat conduction, thermal radiation* and *heat convection* [82]. Since there is no situation in this thesis where the medium between two bodies is assumed to be transparent for the spectral regions relevant for thermal radiation, this mode of heat transfer will from now on be neglected, leaving only heat convection and heat conduction.

Over the years, a set of dimensional groups has been developed to determine the ratio between the modes of heat transfer in a particular system. This thesis uses two of them, the Nusselt number and Prandtl number, which are described below.

The Nusselt number defines the ratio of heat transferred through convection (*fluid motion*) to the heat transferred through conduction (*if the fluid was stagnant*) at a boundary surface. Since fluid motion always results in increased heat transfer, the Nu is always greater than 1 if convection occurs.

$$Nu_L = \frac{Convective\ heat\ transfer}{Conductive\ heat\ transfer} = \frac{h_c}{k_l/L} = \frac{h_c L}{k_l} \tag{3.11}$$

Where h_c is the convective heat transfer coefficient and k_l the thermal conductivity of the fluid. A Nu close to unity indicates a sluggish motion in the fluid, being marginally more effective than the conduction by the stagnant fluid. A higher Nu implies a more efficient convection: Turbulent flow in pipes usually yields Nu in the order of 100 to 1000 [83].

The Prandtl number represents the ratio of diffusion of momentum to diffusion of heat in a specific fluid. It indicates how fluid properties affect heat transport in the fluid by comparing the relative thickness of the velocity boundary layer to the thermal boundary layer [82].

$$Pr = \frac{Viscous\ diffusion\ rate}{Thermal\ diffusion\ rate} = \frac{\mu/\rho}{k/(c_p \rho)} = \frac{c_p \mu}{k} \tag{3.12}$$

Here c_p is the specific heat capacity at constant pressure. Using the example of a flow through a heated pipe, a $Pr < 1$ indicates that the fluid temperature along the center line heats up almost as fast as along the pipe walls. This is usually true for gases and liquid metals. A $Pr > 1$ implies that the fluid temperature along the center line takes much longer to reach the temperature of the pipe walls. For the pressures and temperatures encountered in this thesis, $Pr_{CO_2} \sim 2$.

3.3.3. Lumped thermal capacity model

When a system maintains a nearly uniform temperature while it undergoes a transient thermal response to a heat transfer process, small differences of temperature within the system may be ignored and a single uniform temperature may be used. This concept is called the lumped thermal capacity model. Its validity is determined through a dimensionless quantity called the Biot number:

$$Bi = \frac{internal\ conduction\ resistance}{external\ convection\ resistance} = \frac{L/k_s A}{1/h_c A} = \frac{h_c L}{k_s} \tag{3.13}$$

$Bi < 0.1$ ensures that the temperature at the center of the body will not differ by more than 5% from that at the surface [82], so this is a suitable criterion for determining if the lumped thermal capacity model is valid.

3.3.4. Phase transition

Along the transport and storage chain, the CO_2 will undergo a transition from the liquid to the supercritical phase, where the boundaries between the liquid phase and the vapor phase vanish. This transition is initiated by a change in temperature and pressure, as shown in table 3.4. As a result, some properties of the medium change as well: Supercritical CO_2 has the density of a liquid, but a lower viscosity and a higher compressibility.

Liquid	$T > T_{vap}$	$p > p_{vap}$
Gas	$T < T_{vap}$	$p < p_{vap}$
Liquid-like supercritical	$T < T_c$	$p > p_c$
Gas-like supercritical	$T > T_c$	$p < p_c$
Supercritical	$T > T_c$	$p > p_c$

Table 3.4: Definition of the different CO_2 phases encountered in this thesis, along with their conditions [84] [85]

3.3.5. Cavitation

The pressure at which a liquid boils and is in equilibrium with its own vapor phase is called the vapor pressure. As long as the liquid pressure is higher than the vapor pressure, evaporation at the interface accounts for the only exchange in mass. But if the liquid pressure drops below the vapor pressure, vapor bubbles start to appear. If this drop in liquid pressure is induced by a flow phenomenon, such as an obstruction, it is called cavitation. Once the liquid pressure rises again, the cavitative bubbles collapse, creating a shock wave which can cause significant damage to the equipment. Hence, cavitation should be avoided if possible.

Whether or not a flow sytem is prone to cavitation can be estimated with the Cavitation number, a dimensionless quantity that expresses the relationship between the difference in local pressure from the vapor pressure p_{vap} and the kinetic energy per volume.

$$Ca = \frac{p - p_{vap}}{\frac{1}{2}\rho u^2} \qquad (3.14)$$

Zero or a negative cavitation number at any point in a flow indicates a high probability of vapor-bubble formation - and thus cavitation - at that location.

3.3.6. Joule-Thomson effect

The Joule-Thomson effect is a thermodynamic effect that describes the temperature change of a real gas (as opposed to an ideal gas) or liquid when it is allowed to expand from high pressure to low pressure through a valve, porous plug or other throttling device, while insulation prevents any heat exchange with the environment. This process is also known as an adiabatic expansion, which implies that the enthalpy remains constant [61].

The classic Joule-Thomson expansion experimental setup is shown in figure 3.6 and consists of a thermally insulated system in which gas is allowed to expand freely through a porous plug that acts as a throttle. The gas on the left side, initially at pressure p_1, volume V_1 and temperature T_1, flows through the plug and out the other side at p_2, V_2 and T_2.
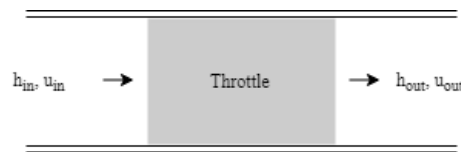
Figure 3.6: A diagram showing the principle of the Joule-Thomson apparatus

The energy equation presented in section 3.2.2 is now applied to this steady state situation, where the continuity equation shown in section 3.2.1 determines that the mass flow rates must be equal. Since the system is thermally insulated and no work is done by or on the plug, both $\dot{Q}$ and $\dot{W}$ are reduced to zero. Furthermore, the setup is assumed to be completely horizontal so the gravitational terms cancel out. This means that equation 3.7 can be reduced to

$$h_{in} + \frac{1}{2} \cdot u_{in}^2 = h_{out} + \frac{1}{2} \cdot u_{out}^2 \qquad (3.15)$$

Since the in- and outflow areas are equal, the velocities on both sides are equal as well during steady state, so according to equation 3.15 the expansion occurs at constant enthalpy:

$$\Delta h = h_{in} - h_{out} = 0 \tag{3.16}$$

Experimental research has shown that the plot of $\Delta T = T_2 - T_1$ against $\Delta p = p_2 - p_1$ is approximately linear with the slope of the rate of change of temperature T with respect to pressure p at constant enthalpy, denoted as the Joule-Thomson coefficient μ_{JT} [86]:

$$\frac{\Delta T}{\Delta p} \approx \left(\frac{\delta T}{\delta p}\right)_h = \frac{V}{c_p}(\alpha T - 1) = \mu_{JT} \tag{3.17}$$

Here V stands for the gas's volume and α is its coefficient of expansion. A positive μ_{JT} means that expansion of the gas leads to cooling. However, all real gases have an inversion point at which the value of μ_{JT} changes signs. The temperature at which the inversion point is reached, the so-called Joule-Thomson inversion temperature, depends on the particular gas and its pressure before expansion. A negative μ_{JT} means that the gas will heat upon expansion. Table 3.5 gives an overview when the Joule-Thomson effect cools or warms a real gas:

If the gas temperature is	then μ_{JT} is	since δP is	thus δT must be	so the gas
below the inversion temperature	*positive*	*always negative*	*negative*	*cools*
above the inversion temperature	*negative*	*always negative*	*positive*	*warms*

Table 3.5: Conditions that determine whether the Joule-Thomson effect cools or warms a real gas [87]

The inversion temperature of CO_2 at atmospheric pressure is 1500 K [87] - and even though this decreases with increasing pressure, the gas temperature will always be lower than the inversion temperature in pressure ranges encountered in CCS applications [88] [89]. It is therefore assumed that the CO_2 will cool upon entering the reservoir.

One commonly known occurrence of the JT effect is an uncontrolled discharge of pressurized CO_2 - for example due to a ruptured pipeline - whereafter it will expand to gaseous CO_2. The Joule-Thomson effect associated with this pressure drop will cause temperatures in the immediate surrounding area to rapidly fall [59].
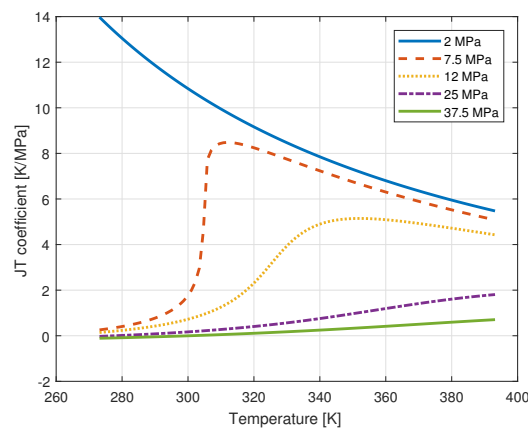
Figure 3.7: Joule-Thomson coefficient of pure CO_2 as a function of temperature [60].

3.4. Configuration of simulation model

This section describes how the different transport phenomena are calculated, so that they can be integrated into the simulation model.

3.4.1. Transport from shore to platform

The first stage of the transport and storage chain consists of transporting liquid CO_2 solution from shore to a platform by means of a pipeline.

Heat transfer

During the transport from shore to platform, the liquid CO_2 solution inside the pipeline will be cooled by forced convection through the ocean water and by heat conduction through the surrounding seabed.
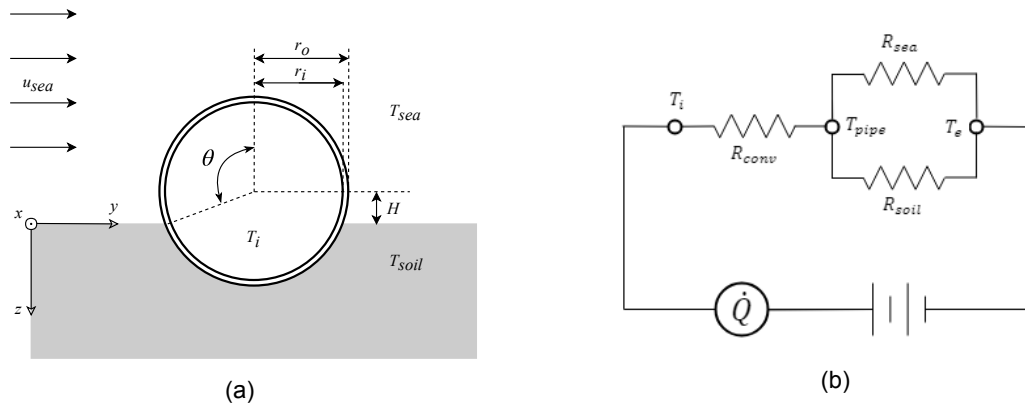
Figure 3.8: **Left:** A schematic diagram of a partially buried transport pipe section on the seabed. **Right:** the equivalent thermal circuit corresponding to the heat transfer from the fluid inside the pipe to its surroundings.

A set of assumptions is established to determine the physical transport phenomena while the liquid solution travels through the pipeline:

- The single-phase fluid is assumed to travel along a horizontal pipe with a constant diameter at steady state conditions

- The fluid is assumed to be incompressible and fully developed; the pressure and temperature of the liquid solution are not radially dependent (quasi-steady perfect mixing occurs)

- Heat is assumed to travel radially outwards from the pipe

- The inside- and outside diameter of the pipe are isothermal surfaces of the same temperature (Lumped thermal capacity model is valid)

- $T_e \approx T_{soil} \approx T_{sea}$

- The heat transfer to the seabed is modelled as a 2D concentric circle with infinite radius

- Material properties remain constant over the given temperature range of $283.15 - 303.15\ K$

The convective heat transfer coefficient from the pipe wall to the solution inside is found using the Dittus-Boelter correlation, an explicit function of the Reynolds number and the Prandtl number for calculating the Nusselt number. The Dittus-Boelter correlation is an empirical correlation of data from experiments and has gained wide-spread acceptance for the calculation of turbulent heat transfer in a smooth pipe - especially for $Re > 10^3$ [82].

$$Nu_{D_i} = 0.023 \cdot Re_{D_i}^{0.8} \cdot Pr^n = 0.023 \cdot \left(\frac{\rho u D_i}{\mu}\right)^{0.8} \cdot \left(\frac{c_p \mu}{k}\right)^n \qquad (3.18)$$

Here $n = 0.3$, since the fluid is cooled by the sea water and sea bed [82]. In this case the characteristic length is the hydraulic diameter $D = 2 \cdot r_i$. The resulting Nusselt number is then used to determine the convective heat transfer coefficient:

$$h_{c_i} = Nu_{D_i} \cdot \frac{k_{CO_2}}{2 \cdot r_i} \tag{3.19}$$

Where r_i is the inner radius of the pipe.

Assuming an average flow velocity of $2m/s$ due to ocean currents [90], the Reynolds number for the outside flow around the pipe is found to be around $Re = 6.95 \cdot 10^5$. According to literature, the average Nusselt number for flow over a cylinder at $Pr > 0.5$ and $Re_D > 4 \cdot 10^5$ can be best determined by means of the following correlation by Churchill and Bernstein [91] [82]:

$$Nu_{D_o} = 0.3 + \frac{0.62 \cdot Re_{D_o}^{1/2} \cdot Pr^{1/3}}{[1 + (0.4/Pr)^{2/3}]^{1/4}} \cdot \left[1 + \left(\frac{Re_D}{282000}\right)^{5/8}\right]^{4/5} \tag{3.20}$$

Next, the heat transfer coefficient can be calculated:

$$h_{c_{sea}} = Nu_{D_o} \cdot \frac{k_{sea}}{2 \cdot r_o} \tag{3.21}$$

Here r_o is the outer radius of the pipe. To determine the overall heat transfer from the transport medium through the pipe wall to the surroundings, an overall shape factor is constructed using the depth of the pipe's center line relative to the seabed:

$$R_{total} = R_{sea+soil} = \frac{1}{UA} = \frac{\theta}{\pi} \cdot R_{sea} + (1 - \frac{\theta}{\pi}) \cdot R_{soil} \ , \ \ with \ \ \theta = acos\left(\frac{H}{r_o}\right) \tag{3.22}$$

Here $R = \frac{1}{UA}$ is the overall thermal resistance. Assuming a thermal conductivity of 0.9 $\frac{W}{mK}$ for the seabed [92] and the heat transfer coefficient calculated in equation 3.21, the heat resistance of the soil and sea can be determined as follows:

$$R_{soil} = \frac{1}{k_{soil} \cdot S} \ \ with \ \ S = \frac{2\pi \cdot dx}{cosh^{-1}(H/r_o)} \ ; \ \ R_{sea} = \frac{1}{h_{c_{sea}} \cdot A} \tag{3.23}$$

Where S denotes the shape factor and L the length of the pipe in the x-direction. Now that the convective heat transfer coefficient is known, the thermal resistances from equation 3.23 are combined in series, after which they are substituted into Newton's law of cooling, shown in equation 3.24:

$$\dot{Q} = UA \cdot \Delta T = \frac{\Delta T}{\frac{\theta}{\pi} \cdot R_{sea} + (1 - \frac{\theta}{\pi}) \cdot R_{soil}} \tag{3.24}$$

Application of the assumptions to the steady flow energy equation (eq. 3.7) results in

$$\dot{m} \cdot \Delta h = -\dot{Q} \tag{3.25}$$

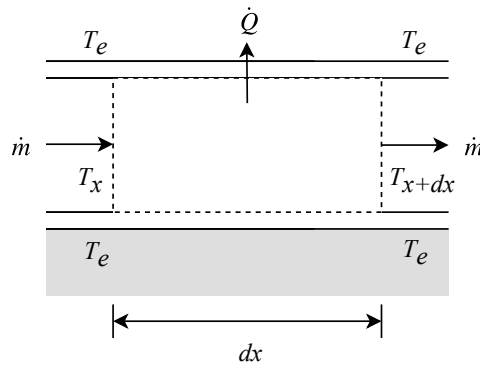Now an energy balance is done on the system boundaries of the CV as shown in figure 3.9:

Figure 3.9: The system boundaries of the control volume for an element of transport pipe of length dx.

Substituting equation 3.25 into equation 3.24, and assuming heat transfers out across the system boundary, yields:

$$\dot{m} \cdot c_p \cdot (T_{x+dx} - T_x) = \frac{\Delta T \cdot dx}{\frac{\theta}{\pi} \cdot R_{sea} + (1 - \frac{\theta}{\pi}) \cdot R_{soil}} \tag{3.26}$$

Now divide by dx and since $T > T_e$, rewrite $\Delta T = T - T_e$, where T_e is the external temperature of both the sea bed and the water and T is the temperature of the fluid:

$$\dot{m} \cdot c_p \cdot (\frac{T_{x+dx} - T_x}{dx}) = \frac{1}{\frac{\theta}{\pi} \cdot R_{sea} + (1 - \frac{\theta}{\pi}) \cdot R_{soil}} \cdot (T_e - T) \tag{3.27}$$

Rearranging and letting $dx \to 0$ yields a differential equation for the temperature as a function of depth:

$$\frac{dT}{dx} = \frac{1}{\frac{\theta}{\pi} \cdot R_{sea} + (1 - \frac{\theta}{\pi}) \cdot R_{soil}} \cdot \frac{T - T_e}{\dot{m} \cdot c_p} \tag{3.28}$$

This equation is used to calculate the temperature of the liquid CO_2 inside the pipe as a function of distance.

Pressure loss

While the liquid (incompressible) CO_2 travels a certain distance through a pipeline, it loses energy through friction alongside the pipe walls, resulting in a pressure drop as depicted in figure 3.10. The following assumptions are used to calculate this loss in pressure:

- The single-phase fluid is assumed to travel along a constant diameter horizontal pipe at steady state conditions

- The fluid is assumed to be fully turbulent and incompressible; the pressure and temperature of the liquid solution are not radially dependent (quasi-steady perfect mixing occurs)

- Pressure loss is caused by viscous effects and follows the Darcy-Weisbach equation: It is proportional to the length of the pipe and to the square of the mean flow velocity

- Material properties remain constant over the given temperature range of $283.15 - 303.15\ K$
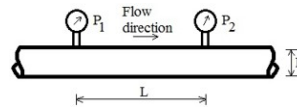
Figure 3.10: Schematic diagram of a segment of transport pipeline.

Assuming a pressure of approximately 12 MPa and a mass flow rate of 50 kg/s yields a volumetric flow rate of about $0.265\ m^3/s$. Using a pipeline diameter of $0.66\ m$, the flow velocity is found to be $2.83\ \frac{m}{s}$ and the Reynolds number from section 3.3.1 becomes $Re \geq 4.4 \cdot 10^6$. Using a roughness of $0.5\ mm$ for rusted steel [93], the relative roughness is $8 \cdot 10^{-3}$.

The most accurate relation to find the Darcy friction factor in rough pipes at $Re \geq 4000$ is the *Colebrook-White* equation [94].

$$\frac{1}{\sqrt{f_D}} = -2 \cdot log\left(\frac{\epsilon}{3.7 \cdot D_h} + \frac{2.51}{Re \cdot \sqrt{f_D}}\right) \tag{3.29}$$

Where ϵ is the pipe wall roughness. The friction factor f_D is then substituted into the *Darcy-Weisbach* equation (Eq. 3.30), which results in the pressure drop per unit length of the pipe for an incompressible fluid.

$$\frac{\Delta p}{L} = f_D \cdot \frac{\rho}{2} \cdot \frac{u^2}{D} \tag{3.30}$$

A dimensional analysis is used to determine how the pressure drop scales with the pipe diameter: An infinitely long pipe decouples its flow characteristics from the position along the pipe, resulting in a relative pressure drop per pipe length of $\frac{\Delta p}{L}$. Since pressure has the dimension of energy per unit volume, the pressure drop between two points must be proportional to $\frac{1}{2}\rho u^2$. As the pressure drop per unit length is a constant, the pressure must be proportional to the length of the pipe between the two points:

$$\Delta p \propto \frac{L}{D} \cdot \frac{\rho}{2} \cdot u^2 = \frac{8L}{D^5} \cdot \frac{1}{\rho \pi^2} \cdot \dot{m}^2 \tag{3.31}$$

This means that the pressure drop should scale inversely with the pipe diameter, assuming a constant flow velocity. Since a constant mass flow rate is a more reasonable approach for this research, the flow velocity will also change with the pipe diameter - meaning the pressure drop should scale inversely with the pipe diameter raised to the fifth power.

However, since the diameter is also present in the Colebrook-White equation (eq 3.29), a change in D also results in a change in the relative roughness $\frac{\epsilon}{D}$, affecting the Darcy friction factor.

P18-2 test case

First, the temperature of the transport medium is explored at a constant mass flow rate for different inflow temperatures and pipeline diameters, inside a semi-buried pipe ($H = 0$) over a length of $40km$. Then the question whether heat is mainly transferred through convection or through conduction is examined, by evaluating the fluid temperature first for a freely suspended pipe ($H = -r_o$) and then for a pipe that is fully buried ($H = r_o$), both with a diameter of $0.66m$.

The pressure loss is calculated over a horizontal $40km$ pipe for a different set of diameters and a varying surface roughness. First, three diameters ($0.33m$, $0.66m$ and $0.99m$) are tested with a constant roughness of $0.05mm$ (new, smooth steel) and $5mm$ (intensily rusted steel) over a distance of $10km$ for a constant flow velocity. This should show whether the diameter-caused change in f_D is significant enough to render the first part of the dimensional analysis from equation 3.31 inaccurate and, if so, whether this can be related to the pipe's surface roughness. Next, the same calculation is performed for a constant mass flow rate, to confirm the second part of equation 3.31's dimensional analysis.

3.4.2. Transport from platform to reservoir

After arriving at the platform, the liquid CO_2 enters the smaller vertical well pipe to the reservoir, where it undergoes the following processes:

Heat transfer

In contrast to the situation described in section 3.4.1, the medium in the injection tube is heated by the environment. This section describes the heat transfer from the surrounding formations to the injected medium inside the well pipe, to see if the geothermal energy is sufficient for the solution to become supercritical prior to entering the reservoir. Assuming that the fluid injection rate and the surface temperature are known, the fluid's temperature is solved as a function of time and depth.

The cross section of most wells consists of varying layers made up of tubes, pipes, an annulus, cement layers and casings, depending on the age and intended use of the well. For simplification, this thesis models the well as a single pipe traveling vertically through a geological formation. An example of the schematic diagram of the P18-4 well is shown in appendix D. In this thesis, the well is modeled as a single vertical pipe, as shown in figure 3.11 on the next page.
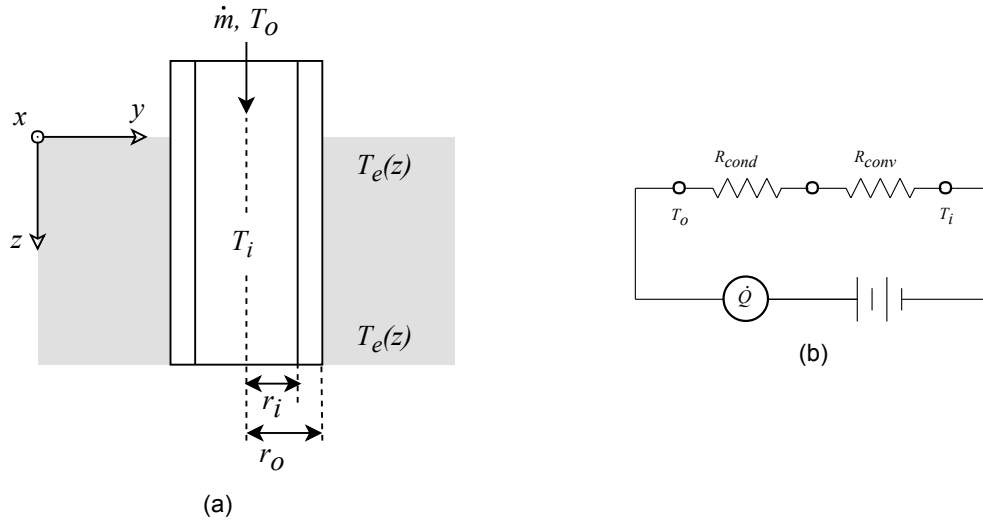
Figure 3.11: **Left:** A schematic diagram of a well pipe section in a geological formation. **Right:** The equivalent thermal circuit corresponding to the heat transfer conducted through the pipe wall and convected into the injection medium.

To develop an expression for the heat transfer mechanisms governing the pipe section, the following set of assumptions is established:

- The single-phase medium is assumed to travel down a constant-diameter vertical pipe

- Heat transfer in the well pipe is rapid compared to heat flow in the formation, thus the system can be represented as a steady state solution

- The medium instantly and fully transitions from the liquid phase to the supercritical phase at the calculated depth

- The pressure and temperature of both the liquid solution and the supercritical solution are not radially dependent (quasi-steady perfect mixing occurs)

- The fluid is assumed to be incompressible, and fully developed and friction losses are assumed to be negligible

- The heat is assumed to travel radially from the surrounding formation towards the well

- The inside and outside surfaces of the pipe are isothermal (Lumped thermal capacity model is valid)

First, the overall thermal resistance R_{total} is determined: it is the net resistance to heat flow offered by the pipe wall and by the fluid flowing inside the pipe.

$$where \quad R_{cond} = \frac{r_o - r_i}{k_{pipe} \cdot S} \quad and \quad R_{conv} = \frac{1}{h_{c_i} \cdot A_i} \tag{3.32}$$

The conduction shape factor S is used to describe the conductive heat flow between the outer and inner surface of the pipe. By describing the pipe geometry as two concentric cylinders, the shape factor is

$$S = \frac{2\pi \cdot dz}{ln(r_o/r_i)} \tag{3.33}$$

While the dimensions and thermal conductivity of the well can be easily determined, the convective heat transfer coefficient is found using the Dittus-Boelter correlation, which is especially recommended for $Re > 10'000$.

$$Nu_{D_i} = 0.023 \cdot Re_{D_i}^{0.8} \cdot Pr^n = 0.023 \cdot \left(\frac{\rho u D_i}{\mu}\right)^{0.8} \cdot \left(\frac{c_p \mu}{k}\right)^n \tag{3.34}$$

This time, $n = 0.4$, since the fluid is heated by the surrounding formation [82]. The resulting Nusselt number is then used to determine the convective heat transfer coefficient:

$$h_{c_i} = Nu_{D_i} \cdot \frac{k_{CO_2}}{2 \cdot r_i} \tag{3.35}$$

Now that the convective heat transfer coefficient is known, the thermal resistances from equation 3.32 are combined in series, after which they are substituted into Newton's law of cooling, which was shown in equation 3.24:

$$R_{total} = \frac{1}{UA} = \frac{ln(r_o/r_i)}{k_{pipe} \cdot 2\pi \cdot dz} + \frac{1}{h_{c_i} \cdot 2\pi \cdot r_i \cdot dz} \tag{3.36}$$

$$\dot{Q} = UA \cdot \Delta T = \frac{2\pi dz}{\left(\frac{1}{h_{c_i} \cdot r_i} + \frac{ln(r_o/r_i)}{k_{pipe}}\right)} \cdot \Delta T \tag{3.37}$$

Application of the assumptions to the steady flow energy equation (eq. 3.7) results in the following expression:

$$\dot{m} \cdot \Delta h = -\dot{Q} \tag{3.38}$$

Now an energy balance is done on the system boundaries of the CV as shown in figure 3.12 below:
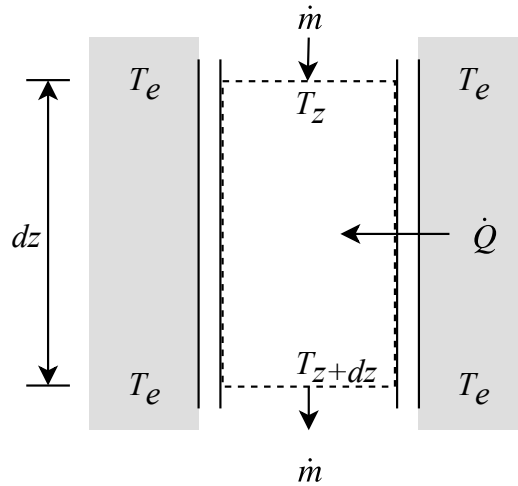
Figure 3.12: The system boundaries of the control volume for an element of well pipe of depth dz.

Substituting equation 3.38 into equation 3.24, and assuming heat transfers in across the system boundary, yields

$$\dot{m} \cdot c_p \cdot (T_{z+dz} - T_z) = \frac{2\pi \cdot dz}{\left(\frac{1}{h_c r_i} + \frac{ln(r_o/r_i)}{k_{pipe}}\right)} \cdot \Delta T \tag{3.39}$$

Now divide by dz and, since $T_e > T$, rewrite as $\Delta T = T_e(z) - T$, where T_e is a function of depth governed by the geothermal gradient, as shown in table 2.3:

$$\dot{m} \cdot c_p \cdot \left(\frac{T_{z+dz} - T_z}{dz}\right) = \frac{2\pi}{\left(\frac{1}{h_c r_i} + \frac{ln(r_o/r_i)}{k_{pipe}}\right)} \cdot \left(T_e(z) - T\right) \tag{3.40}$$

Rearranging and letting $dz \rightarrow 0$ yields a differential equation for the temperature as a function of depth:

$$\frac{dT}{dz} = \frac{2\pi}{\dot{m} \cdot c_p \cdot \left(\frac{1}{h_c \cdot r_i} + \frac{ln(r_o/r_i)}{k_{pipe}}\right)} \cdot \left(T_e(z) - T\right) \tag{3.41}$$

This equation is used to calculate the temperature of the injected CO_2 as a function of depth. It determines at which depth it becomes supercritical, which is essential to determine if a specific reservoir requires an auxiliary heater.

Gravitational pressure increase
While the injected solution travels down the vertical well pipe, the hydrostatic pressure gradient causes the pressure to increase with depth. The following assumptions are used to establish an expression for the pressure at the bottom of the CO_2 column:

- The column of liquid CO_2 - and later supercritical CO_2 - inside the well is at rest in stable equilibrium and results in a higher static pressure at the bottom

- The average densities of CO_2 for the liquid phase and the supercritical phase are calculated for the mean temperature and pressure using the gradients from table 2.3

$$p_{bottom}(z) = \rho_{l,avg} \cdot g \cdot z_{transition} + \rho_{sc,avg} \cdot g \cdot (z_{depth} - z_{transition}) + p_{in} \qquad (3.42)$$

Here $z_{transition}$ is the depth at which the solution becomes supercritical, determined with equation 3.41. To achieve a continuous injection rate, the pressure at the bottom of the CO_2 column must remain above the reservoir pressure. The outcome will determine whether an auxiliary pump is required.

Injection into reservoir
In this step, the injection of the supercritical CO_2 into the reservoir is modeled. The simplified model of the injection step consists of an infinite supply of supercritical CO_2 at the desired injection pressure, which is connected to a closed tank at an initial pressure, with a closed valve in between. Once the valve is opened, the CO_2 flows into the tank until the pressure inside the tank reaches the injection pressure.

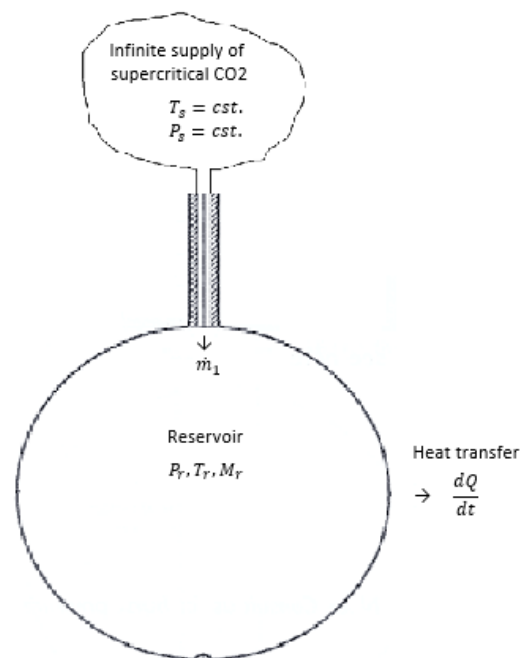Figure 3.13: The injection is modeled as an infinite supply of CO_2 connected to a closed tank.

The following assumptions are used to derive an expression for the mass flow rate, the reservoir temperature, the injection flow speed and the Joule Thomson-cooling:

- The reservoir is modeled as a spherical tank with a constant volume, filled with an infinite supply volume with constant temperature and pressure

- The compressible single-phase supercritical medium is assumed to travel down a constant diameter vertical pipe at steady state conditions

- Changes in kinetic energy and potential energy are negligible

- The pressure and temperature of the supercritical solution are not spatially dependent (quasi-steady perfect mixing occurs)

- Since the reservoir is filled slowly, all internal energy generated by compression is dissipated to the surrounding formations; the reservoir temperature remains constant

Mass flow rate

The energy balance from equation 3.5 over the last section of pipe and the reservoir is simplified by neglecting the potential energy term and assuming that no work is done.

$$\frac{dU}{dt} = \frac{dQ_{env}}{dt} + \dot{m}_{in}(h_{in} + \frac{1}{2}u_{in}^2) - \dot{m}_{out}(h_{out} + \frac{1}{2}u_{out}^2) \tag{3.43}$$

Since the reservoir temperature is assumed to remain constant, the change in internal energy must be equal to the amount of heat transferred to the surrounding formations. Isolating the terms in the brackets from equation 3.7 yields the following expression for the CV over figure 3.13, where the subscript *res* refers to the reservoir:

$$h_{in} + \frac{1}{2}u_{in}^2 = h_{res} + \frac{1}{2}u_{res}^2 \tag{3.44}$$

Since there will be no flow velocity inside the reservoir, u_{res} is set to zero. By replacing u_{in} with $\frac{\dot{m}}{\rho \cdot A}$, equation 3.44 can be rewritten as:

$$h_{in} + \frac{u_{in}^2}{2} = h_{in} + \frac{1}{2}\left(\frac{\dot{m}_{in}}{\rho \cdot A_{in}}\right)^2 = h_{res} \tag{3.45}$$

This expression can be rewritten to determine the mass flow rate injected into the spherical tank:

$$\dot{m}_{in} = \sqrt{2 \cdot \rho_{in}^2 \cdot A_{in}^2(h_{res} - h_{in})} \tag{3.46}$$

Reservoir temperature & heat transfer

Since the filling of the reservoir is a relatively slow process, the reservoir temperature is assumed to remain constant despite the increasing pressure, meaning all the heat is dissipated into the surrounding geological formation. Since the enthalpy of the supply flow remains constant, equation 3.46 implies that the reservoir enthalpy must be larger in the beginning, and should start to decline once the pressure is increased. This is confirmed in figure 3.14 below:

In an isolated system, the influx of a gas causes the tank temperature to increase due to compression. As mentioned in section 3.4.2 above, assuming a constant reservoir temperature implies that this heat is transferred to its surroundings.

$$\frac{dU}{dt} = \frac{dQ_{env}}{dt} = \dot{m}(p) \cdot c_p(p) \cdot T_{in} \tag{3.47}$$

Injection flow speed

Equation 3.43 of the principle of energy conservation is simplified to give an indication of the maximum flow speed inside the injection pipe. Since u_{out} reduces to zero and a steady state situation is assumed, the equation reduces to equation 3.45, which is then rearranged to get an expression for the mass injection flow speed:

$$u_{in} = \sqrt{2(h_{out} - h_{in})} = \frac{\dot{m}_{in}}{\rho \cdot A_{in}} \tag{3.48}$$
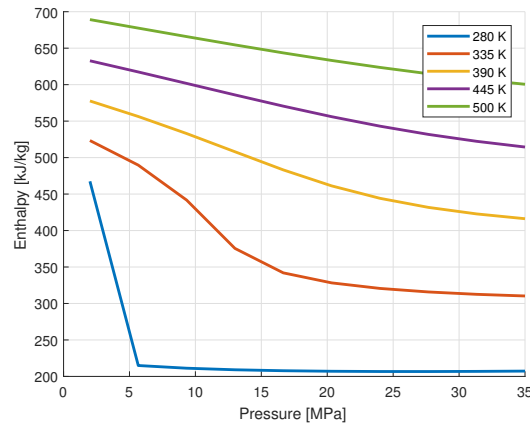
Figure 3.14: The pressure dependence of the enthalpy of pure CO_2 at different temperatures.

Joule-Thomson cooling
During the injection of CO_2, the pressure at the end of the injection pipe will decline promptly as the gas expands into the depleted gas field, hereby causing Joule Thomson-related cooling. One of the concerns is that this cooling effect becomes so strong that it could lead to the formation of hydrates with CO_2 and residual natural gas, while any leftover water could freeze. These solids would significantly reduce the permeability of the surrounding rock, which would have a negative effect on the storage capacity [88].

$$\Delta T_{max} = \mu_{JT} \cdot \Delta p_{max} \tag{3.49}$$

3.4.3. Conditioning steps on the platform
The auxiliary conditioning steps on the platform may consist of a pump and a heater that complement any missing heat energy and pressure to turn the liquid CO_2 supercritical in the well pipe.

Pump
The following set of assumptions is provided to derive an expression for the required power of the pumping stage:

- The column of liquid CO_2 and later supercritical CO_2 inside the well is at rest in stable equilibrium, which results in a static pressure at the bottom

- The pump efficiency η_{pump} depends on the pressure drop and its rotational speed

While the specific considerations that determine the choice of a pump type and pump configuration will be discussed in chapter C, the estimated energy consumption can be derived by converting the desired pressure increase to the equivalent differential head:

$$H_{hd} = \frac{\Delta p}{g \cdot \rho} = \frac{p_{final} - p_{in} - p_{column}}{g \cdot \rho_{CO_2}} \quad [m] \tag{3.50}$$

Here g is the gravitational acceleration, p_{final} is the final reservoir pressure, p_{in} the pressure of the incoming flow and p_{column} the pressure exerted by the liquid column. This can now be substituted into the following equation, which yields the shaft power for the desired pump:

$$P_{pump} = \frac{\dot{m} \cdot g \cdot H_{hd}}{\eta_{pump}(rpm, \Delta p)} \quad [kW] \tag{3.51}$$

Heater
By plotting the in- and output conditions for the heater into the Mollier chart (Pressure-Enthalpy diagram, figure 2.6) for CO_2, the difference in enthalpy was determined. The total

heat energy delivered by the heater is found by multiplying the difference in enthalpy with the mass flow rate:

$$Q_{heater} = \frac{\dot{m} \cdot \Delta h}{\eta_{heater}} = \frac{\dot{m} \cdot (h_{out} - h_{in})}{\eta_{heater}} \quad [kW] \tag{3.52}$$

Transfer to small diameter tube

The liquid medium arrives at the platform in a normal pipeline of diameter d_1 and must be transferred to the smaller well pipe of diameter d_2 for transport to the reservoir. Using the following array of assumptions, an expression for the change in flow characteristics is found:

- Single-phase fluid is incompressible and flowing at steady-state conditions

- The process is isolated and adiabatic

- Isentropic process; irreversibilities such as turbulence can be ignored

- Friction by viscous forces is negligible

- No elevation present
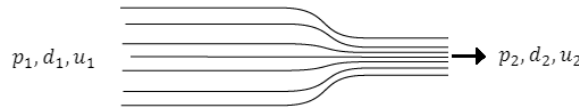
Figure 3.15: A schematic diagram of the converging flow.

As the velocity will increase in the smaller diameter tube, the pressure must decrease. Neglecting the potential energy term from the first law yields

$$h_{in} + \frac{u_{in}^2}{2} = h_{out} + \frac{u_{out}^2}{2} \tag{3.53}$$

For steady flow within this CV, the integral form of equation 3.3 results in the following relation:

$$\dot{m}_{in} = \dot{m}_{out} \rightarrow \rho_{in} \cdot u_{in} \cdot A_{in} = \rho_{out} \cdot u_{out} \cdot A_{out} \tag{3.54}$$

Since the liquid is assumed to be incompressible, all work done on it by pressure forces in any time interval results in a change in its kinetic energy. While the flow in the transport pipe is turbulent and hence contains irreversibilities that will affect the internal energy, the incompressibility assumption means that this change in internal energy will be neglected. Furthermore, the process is assumed to be adiabatic, so the fluid temperature will remain constant:

$$\frac{p_{in}}{\rho} + \frac{u_{in}^2}{2} = \frac{p_{out}}{\rho} + \frac{u_{out}^2}{2} \tag{3.55}$$

The transfer from the transport pipe to the smaller diameter well pipe will lead to an increase in the kinetic energy, which bears the risk of hydrodynamic cavitation. This will be analyzed using the cavitation number.

3.5. Mathematical solution procedure

The heat transfer from the liquid CO_2 inside the transport pipeline to its surroundings is governed by equation 3.28. Since the small temperature range allows the thermodynamic properties to be assumed as constant, this equation is relatively simple to solve analytically.

Calculating the pressure drop over the transport pipeline requires the Darcy friction factor, which is calculated using the Colebrook-White equation shown in equation 3.29. While an explicit solution can be obtained through the Lambert W function, the Colebrook-White equation is usually solved through iteration due to its implicit nature [95].

The heat transfer from the liquid CO_2 inside the well pipe to the surrounding formations is described by equation 3.41. Since the temperature range is much wider than in equation 3.28, the thermodynamic properties cannot be assumed as constant without a considerable loss in accuracy; especially considering the significant changes in thermodynamic behavior around the critical point demonstrated by figures 2.2, 2.3 and 2.5 in section 2.1. As the properties demonstrate nonlinear behavior, equation 3.41 becomes a nonlinear differential equation for which an exact solution would become far too complex.

The goal of this thesis is to present a comprehensive computer model that can be used for different sets of input parameters. This requires a level of flexibility that cannot be achieved analytically, which is why a numerical approach is used instead. The derived differential equations from each subsection are solved using the classic fourth-order Runge-Kutta method in MATLAB. For each time step, the thermodynamic properties are updated from REFPROP. The Colebrook equation for the Darcy-Weisbach friction factor is solved through three iterations.

$$4$$

Results

In this chapter, the results for each section of the transport and storage chain are analyzed separately, as defined in the previous chapter.

4.1. Transport from shore to platform

This section analyses the results of the different transport phenomena that govern the flow of liquid CO_2 while it passes through the subsea transport pipeline.

4.1.1. Heat transfer

The temperature difference between the liquid CO_2 inside the pipe and the surroundings initiates the exchange of thermal energy.

Inflow temperature & pipe diameter

Figure 4.1 (a) shows the temperature of the transport medium as a function of distance for three different inflow temperatures; one of them below the sea temperature, two of them above. Figure 4.1 (b) also shows the temperature of the liquid as a function of distance, but for three different pipe diameters. The liquid in the narrowest pipeline takes much longer to reach the surrounding temperature as opposed to the other liquids. This can be explained by the smaller area that is available for heat transfer, combined with the much higher flow velocity due to the equal mass flow rate.

(a) $D = 0.66m$ (b) $T_{in} = 288.15K$
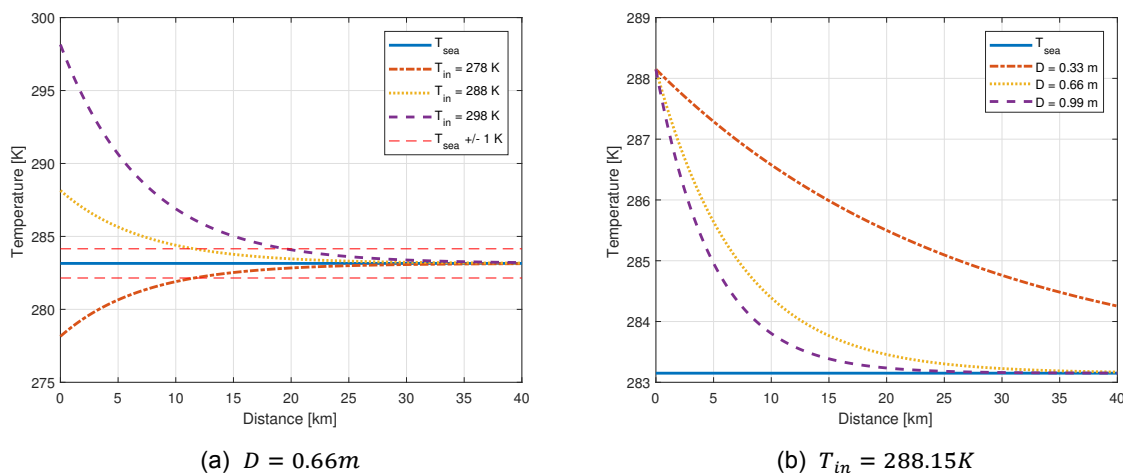
Figure 4.1: The temperature of the transport medium as a function of distance; for different inflow temperatures and pipe diameters.

Convection vs. conduction

Figure 4.2 (a) clearly shows that the heat loss due to forced convection to the surrounding sea water is much larger than that caused by conduction to the surrounding sea bed. Figure 4.2 (b) confirms this result, showing that the heat transfer rate to the surroundings for every meter of pipe is much higher for a completely suspended pipe.
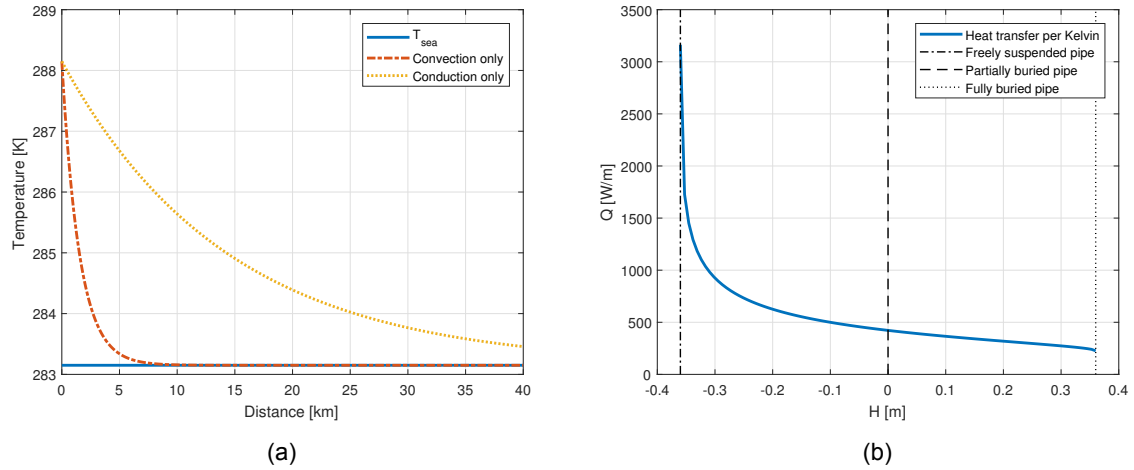
Figure 4.2: **Left:** The fluid temperature as a function of distance for fully convective- and fully conductive flow **Right:** Heat transfer per meter of pipe per degree Kelvin as a function of H.

4.1.2. Pressure loss

Figure 4.3 shows that, if the diameter is doubled at a constant flow velocity, the pressure drop halves, both for a smooth and a rough pipe wall. Multiplying the roughness by 100 increases the pressure drop for each diameter by a factor of 3. The first part of equation 3.31 therefore offers an accurate ratio between the pressure drop and the pipe diameter.

(a) $\epsilon = 0.05mm$ (b) $\epsilon = 5mm$
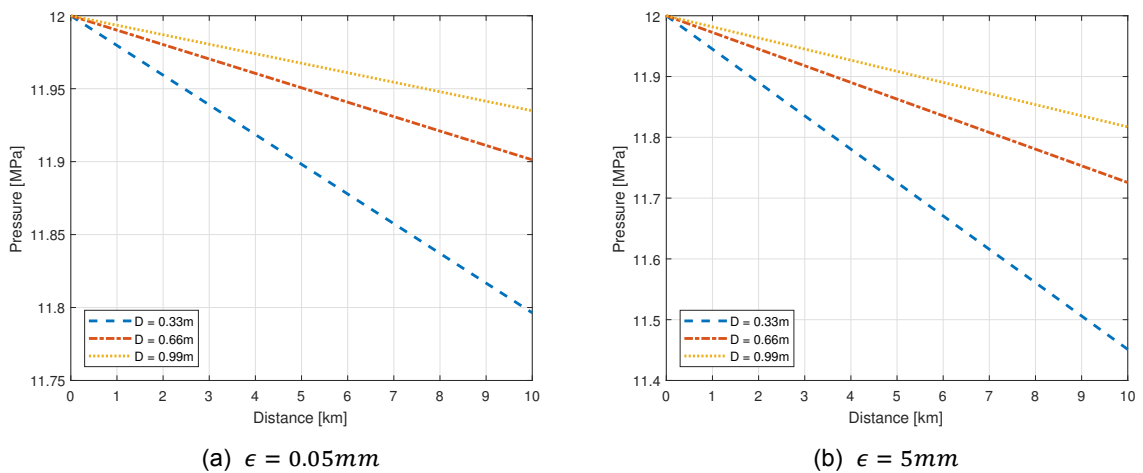
Figure 4.3: The pressure drop over a distance of 10km for three pipe diameters at constant roughness and flow velocity.

Figure 4.4 shows that, for a constant mass flow rate, the pressure drop scales inversely with the diameter raised to the fifth power: For the pipes with a diameter of $0.66m$ and $0.99m$ with a factor of $1/2^5$ and $1/3^5$, accordingly, with respect to the pressure drop over the $0.33m$ diameter pipe. This suggests that the second part of equation 3.31 also represents an accurate

scaling for the pressure drop. Furthermore, the graphs suggest that the surface roughness has a considerably bigger effect on the pressure drop in small diameter pipes, as the pressure in the narrowest pipe decreases by a factor of 3.

(a) $\epsilon = 0.05mm$ (b) $\epsilon = 5mm$
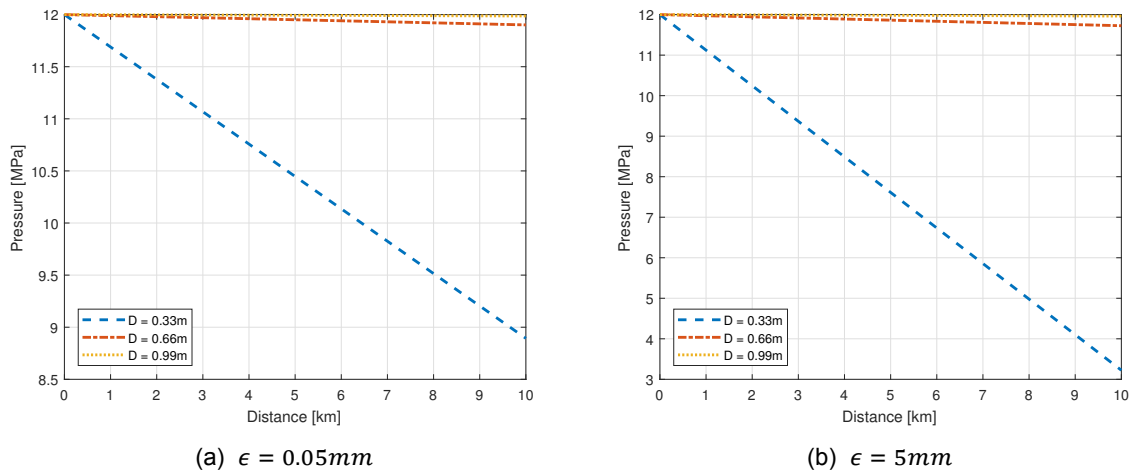
Figure 4.4: The pressure drop over a distance of 10km for three pipe diameters at constant roughness and mass flow rate.

Surface roughness

To investigate the suspicion that the effect of the surface roughness on the pressure loss increases with decreasing pipe diameter, figure 4.5 shows the roughness as a function of the pressure drop for three pipeline diameters over a length of 10km, both on a regular scale (a) and logarithmic (b) scale.

(a)   (b)
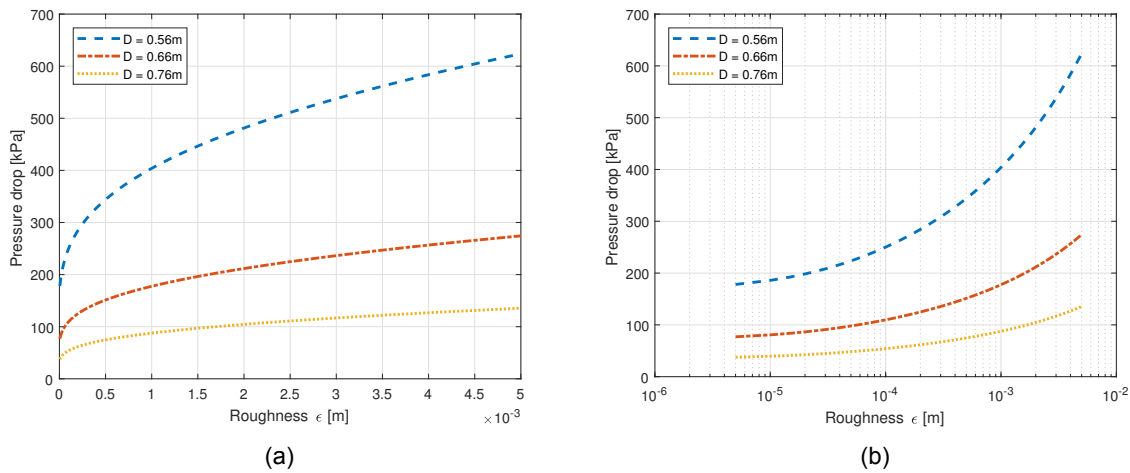
Figure 4.5: The pressure drop as a function of surface roughness for three pipe diameters over a distance of 10km.

It appears that a change in surface roughness has a relatively minor influence on the overall pressure drop below $\epsilon = 10^{-4}$. The effect then increases exponentially with an increasing roughness, and the magnitude of the increase is indeed much higher for the smaller diameter pipelines. Considering the high Reynolds number, this suggests that the relative roughness term ϵ/D in the Colebrook-White equation is dominant in determining the loss in pressure.

4.1.3. Result for P18-2 boundary conditions

For an inflow temperature of 20 °C, the temperature of the liquid CO_2 comes within $1K$ of the surrounding temperature after a distance of 16 km and within $0.1K$ after 30 km.

The pressure drop remains relatively small: 2.28% for every 10 km. For the 40 km pipeline defined in the boundary conditions, the total pressure loss is 9.12%, which results in an output pressure of 10.9 MPa.
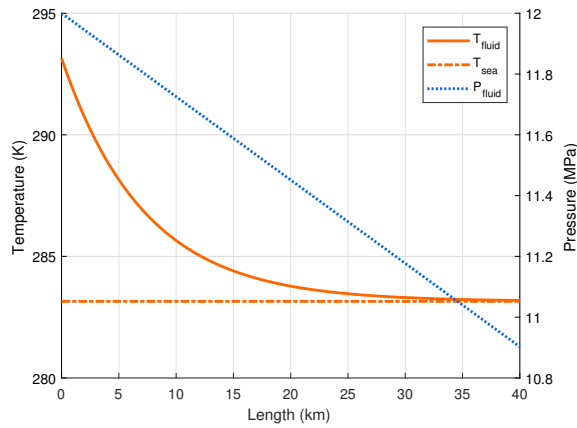
Figure 4.6: Temperature- and pressure development inside a semi-buried 0.66m transport pipe, as defined in the P18-2 case study.

4.2. Transport from platform to reservoir

This section examines the results of the different transport phenomena that govern the flow of CO_2 while it travels down the well pipe and during the subsequent injection into the reservoir.

4.2.1. Heat transfer

Figure 4.7 shows that at a mass flow rate of 350 kg/s in a 0.1m diameter pipe, the liquid CO_2 reaches the critical temperature at a depth of approximately $1190m$. The average heat transfer coefficient is $5.53 \cdot 10^3 \frac{W}{m^2 \cdot K}$. The Biot number for the well pipe turns out to be 2.27, which means that the assumption of a uniform pipe wall temperature reduces the accuracy of the end result.

(a)   (b)
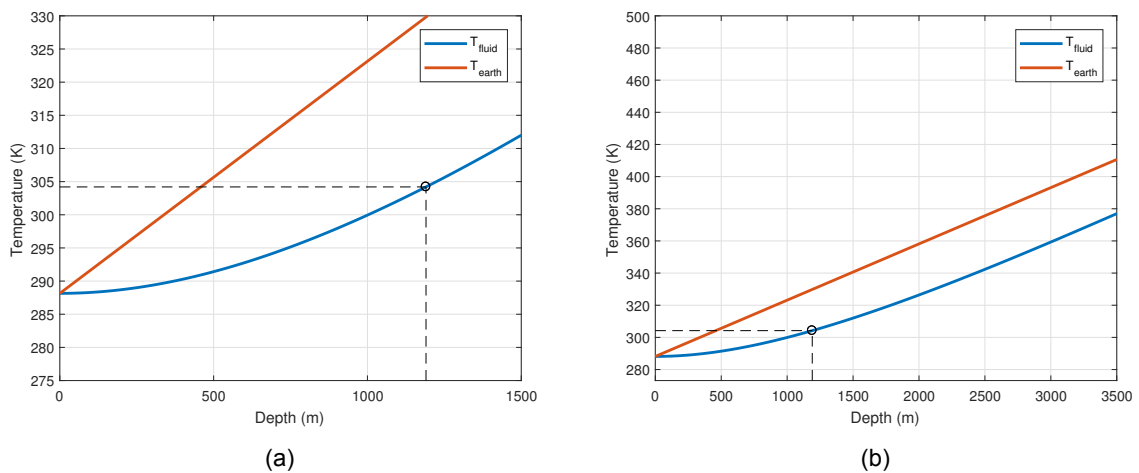
Figure 4.7: Temperature increase of the injected fluid as a function of depth.

4.2.2. Gravitational pressure increase

Using an inflow pressure of 11 MPa, the development of the static pressure inside the column is shown in figure 4.8. At the bottom of the well, the pressure increases to 36.44 MPa. The pressure increase over the CO_2 column therefore amounts to 25.44 MPa.
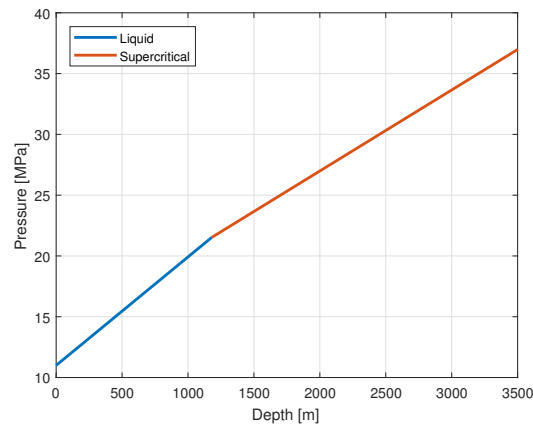
Figure 4.8: Static pressure increase in the well column as a function of depth for liquid and supercritical CO_2.

4.2.3. Injection into the reservoir

If the mass flow rate is constrained to $350\frac{kg}{s}$ and the flow temperature is kept at the level of $400K$, filling the reservoir to 99.99% of the supply pressure takes approximately 3.43 years, or 1250 days. The course of the individual parameters over this period of time is analyzed in the figures below.

Figure 4.9a shows the mass flow rate as a function of time. Since the mass flow rate is capped at $350kg/s$, this maximum value is maintained for the first 2.5 years, after which it linearly decreases due to the decreasing pressure difference between the reservoir and the supply. Figure 4.9b shows the amount of CO_2 stored in the reservoir as a function of time. The final stored mass of $34Mt$ is higher than the expected storage capacity of $32Mt$; this is due to the fact that the initial pressure of $2MPa$ is converted into an equivalent initial mass of CO_2.

(a)   (b)
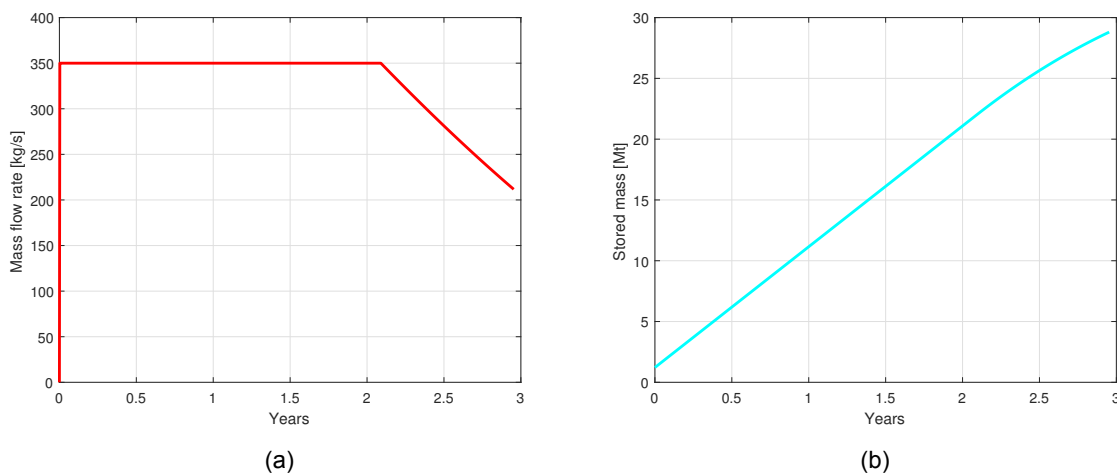
Figure 4.9: **Left:** The mass flow rate of CO_2 into the reservoir as function of time until the reservoir pressure reaches the supply pressure. **Right:** The total injected mass of CO_2 as a function of time.

Figure 4.10a shows the almost linear increase of the reservoir pressure as a function of time, until the reservoir pressure reaches 99.99% of the supply pressure. Figure 4.10b displays the decrease of the enthalpy of the injected CO_2 inside the reservoir as a function of time. The drop in enthalpy is expected because of the increase in pressure while the reservoir temperature remains constant, as explained in section 3.4.2 and figure 3.14.

(a)   (b)
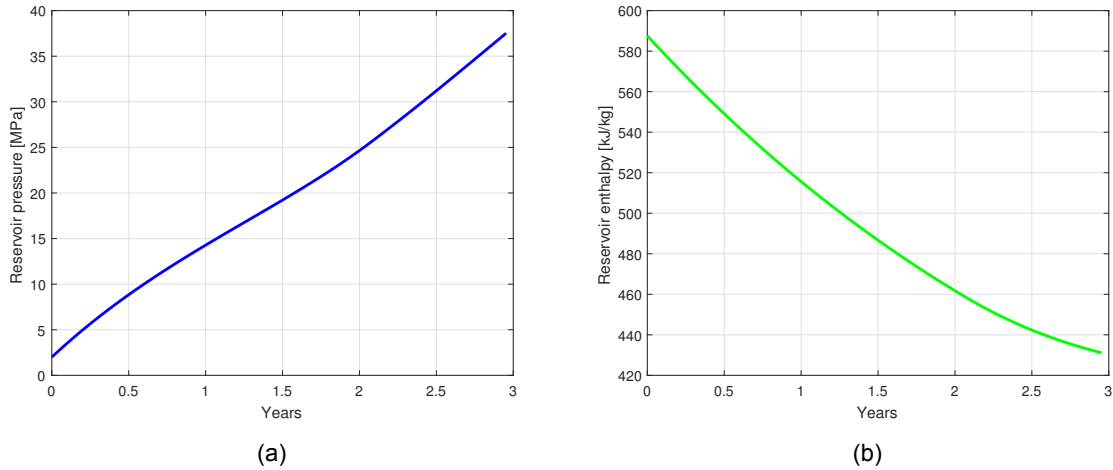
Figure 4.10: **Left:** The reservoir pressure over time. **Right:** The enthalpy of the CO_2 in the reservoir as a function of time.

Last, the constant reservoir temperature implies that any increase in internal energy must dissipate as heat into the surrounding formations. Figure 4.11 shows the rate of heat transfer from the reservoir to its surroundings as a function of time, along with the reservoir temperature as a function of time.

(a)   (b)
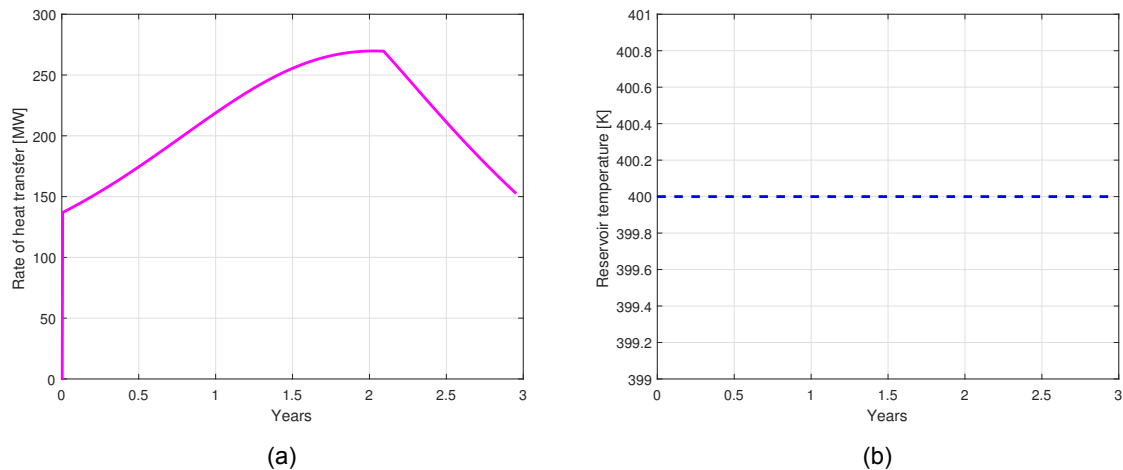
Figure 4.11: **Left:** The rate of heat transfer to the surrounding formations as a function of time. **Right:** Reservoir temperature over time.

4.2.4. Joule Thomson cooling

Sourcing the Joule Thomson coefficient directly from REFPROP, the maximum pressure difference of $35.5MPa$ (encountered in the first moments of injection) results in a local temperature drop of $27K$. As the pressure difference declines, the temperature drop linearly decreases along with the increasing pressure in the reservoir, as shown in figure 4.12. Section 4.2.1 determined that the temperature of the CO_2 lies around $380K$ upon entering the reservoir, well above its critical temperature of $305K$. The Joule Thomson-cooling therefore causes the

local temperature around the well pipe exit to drop to $353K$, which is far from the temperature that might cause phase changes or the formation of hydrates. Therefore, the influence of the Joule Thomson-induced cooling can be neglected.
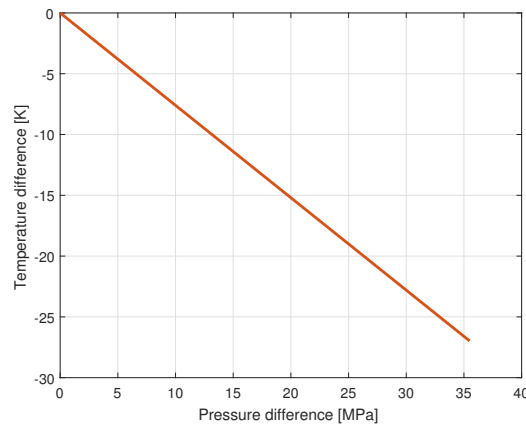
Figure 4.12: Temperature drop due to Joule Thomson cooling as a function of pressure difference.

4.3. Conditioning steps on the platform

This section analyzes how the results from the two previous sections affect the conditioning steps the CO_2 must undergo on the platform.

4.3.1. Pump

The column of CO_2 results in a static pressure increase of $25.44MPa$ at the bottom. When a pressure drop from $12MPa$ to $11MPa$ is assumed over the $40km$ pipeline, the pressure at the bottom of the CO_2 column becomes $36.44MPa$. This means a pumping stage will have to increase the pressure by about $1.1MPa$ to achieve the desired final reservoir pressure of $37.5MPa$.

4.3.2. Heater

The transfer of geothermal energy to the liquid CO_2 results in a transition to the supercritical phase at a depth of approximately $1190m$, which is well above the reservoir depth of $3500m$. This means that no auxiliary heater will be required.

4.3.3. Transfer to a smaller diameter tube

When the liquid CO_2 arrives at the platform, it must transfer from the wider transport tube into the smaller diameter well pipe. This results in a pressure loss of about 0.0016%, which is negligible.

d_1 [m]	d_2 [m]	u_1 [m/s]	u_2 [m/s]	p_1 [MPa]	p_2 [MPa]
0.33	0.1	4.37	47.65	12	11.998
0.66	0.1	1.1	47.65	12	11.998
0.99	0.1	0.49	47.65	12	11.998

Table 4.1: Pressure drop over constricting pipe for different diameter ratios at equal mass flow rate

Cavitation

The cavitation number for this constriction turns out to be $Ca = 0.00239$, which means that there is no significant risk of hydrodynamic cavitation.

4.3.4. Recommended platform configuration for P18-2

Based on these results, the recommended platform configuration is scenario 3 as described in section 3.1.1:
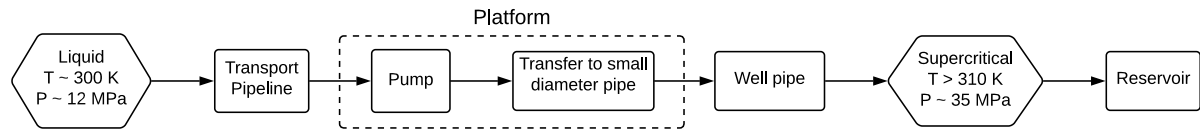
Figure 4.13: Schematic diagram of scenario 3, which includes a pump but no heater.

4.3.5. Input parameters resulting in alternative platform configurations

As the density of both liquid CO_2 and supercritical CO_2 is lower than that of water, the static pressure gradient of CO_2 will always be lower than the hydrostatic pressure gradient. Using the results form section 4.2.2, the average static pressure gradient for CO_2 is 0.0065 MPa/s. Assuming the CO_2 arrives at the platform at $11 MPa$, the depth at which the hydrostatic pressure reaches the static pressure of the CO_2 column can be calculated:

$$z_{min} = \frac{p_{in}}{\left(dp_{H2O}/dz - dp_{CO2}/dz\right) \cdot dz} = \frac{11}{(0.01 - 0.0065) \cdot 1} = 3142 \ m \tag{4.1}$$

This suggests that for any reservoir that is deeper than $3142m$, a pumping stage will be required to reach the final reservoir pressure. Furthermore, the findings from section 4.2.1 indicate that, for boundary conditions similar to those of P18-2, an auxiliary heater is required for a reservoir depth less than $1190m$.

Depending on the exact combination of these parameters, the alternative configuration scenarios from section 3.1.1 are required for successful injection.

5

Discussion

This model uses a supply of pure CO_2 as input. The actual quality of the CO_2 flow depends on the capture method and ranges between 95 and 99.9 %, meaning that it will contain a certain amount of impurities [65] [66]. Since some impurities are known to affect the thermodynamic behavior of the composition, the configuration must be adapted to the specific fluid properties [59]. Impurities can also have a significant effect on corrosion-related performance, which can drive up investment costs [96].

The flow is assumed to be one-dimensional and steady, the latter meaning that it is not time-dependent. The dimensionless quantities used to describe the flow in section 3.3 therefore do not change with time either. Since these dimensionless quantities are often decisive in choosing the optimal correlation to describe a specific situation, any alteration in the flow characteristics requires a new evaluation whether the correlation is still within its validated range. This means that the model can only be used for a limited range of flow characteristics and that it cannot be used to describe the dynamic behavior over short time spans, for instance start-up and shut-down processes. The assumption of incompressible flow for liquid CO_2 also means that irreversibilities associated with turbulent flow are neglected.

During the transport from shore to the platform, the model neglects the effect of differences in height, pipe curvatures and other restrictions. The deviation this causes from the actual situation largely depends on the specific infrastructure configuration.

The case study for the P18-2 revealed that a pump is required to increase the pressure at the bottom of the column to the final pressure of $37.5 MPa$. An option to reduce both the costs and the energy consumption would be to use the pump only during the final phase, when the required pressure increase cannot be achieved through gravitation anymore.

Because of the delayed temperature increase during injection, the CO_2 entering the reservoir is about $20K$ colder than the surrounding formations, meaning that the reservoir temperature will in fact be slightly lower than the temperature of the surrounding formations. As the temperature will stabilize over time, the pressure inside the reservoir will slightly increase even after the well has been sealed. This requires an extra safety margin during the assessment of the reservoir's storage capabilities.

In a common reservoir, the hydrocarbons are contained in porous or fractured rock formations and trapped by an overlying cap rock with a lower permeability. While modelling the reservoir as an underground tank greatly simplifies the process, it also has an impact on the accuracy of the final result: In reality, the injected CO_2 must travel through the porous formations, creating local high pressure spots, which results in a delay in mass transfer. While this will have a limited effect on steady state simulations, dynamic models will have to be adapted accordingly.

Furthermore, common natural gas reservoirs often contain varying amounts of water and residue gas. During the CO_2 injection, the pressure build-up causes it to dissolve in the water, which can result in a decrease in reservoir pressure over time [70]. Research also shows that residual gas can have a negative impact on storage performance and that reservoirs with low residual gas contents are a better choice for storage purposes. [97].

Finally, most natural gas reservoirs are exploited through multiple wells, so injection rates of CO_2 can presumably be increased by injecting it through multiple wells. While this will increase the complexity and certain costs of the transport and storage chain, a shorter overall filling time is likely to reduce overall costs.

6

Conclusion

This study provides a solid basis for a method to evaluate and compare the suitability of different offshore infrastructure configurations for the large-scale transport and storage of CO_2, as part of a CCS chain. The underlying hypothesis was that the high costs of offshore transport of CO_2 can be brought down significantly by reusing existing infrastructure. The general understanding in the field is doubtful whether large volumes of CO_2 can be transported by existing offshore natural gas infrastructure, and whether the reduction in costs would be worthwhile.

Contrary to this view, this study demonstrated that large volumes of liquid CO_2 can be transported offshore through existing pipelines and pass one or two conditioning steps, transition to the supercritical phase while travelling down the well pipe before being injected into a depleted natural gas reservoir. Furthermore, it showed that the transport and storage costs can be brought down by more than 50% by reusing existing offshore infrastructure.

During the transport of the liquid CO_2 from shore to the platform, the report highlights the importance of the relative roughness to determine whether an existing pipe can be reused. Furthermore, the convective heat transfer to the sea water was found to be significantly higher than the conductive heat transfer to the sea bed, suggesting that burying or partially burying a pipeline drastically reduces the heat transfer from the transport medium to its surroundings. For a fixed mass flow rate, a smaller diameter pipe also significantly reduces the heat transfer to the environment, delaying the point where the transport medium cools down to the environmental temperature. In case of a storage location where the geothermal energy is not sufficient to reach the critical temperature, a buried or partially buried small-diameter pipeline can be a solution to minimize the need for auxiliary heating by preserving more of the CO_2's original energy content.

The report also emphasizes the significance of the mass flow rate and the well pipe diameter in determining the depth at which the geothermal heat transfer is sufficient for a full transition of the CO_2 to the supercritical phase. Local cooling due to the Joule-Thomson effect was found to have a negligible influence during injection.

Furthermore, the report identifies a fixed set of input parameters that can be used to evaluate how different infrastructure and reservoir properties affect the requirements of the conditioning steps on the platform: The depth of the reservoir, the diameter of the well pipe, the mass flow rate and the temperature and the pressure of the flow arriving at the platform. While the need for an auxiliary heater depends both on the depth of the reservoir and on the well diameter, a pumping stage was found to be necessary for all reservoirs at depths greater than $3142m$ for the boundary conditions defined in the P18-2 test case.

Finally, the appendix of the report presents a brief overview of the economic and policy challenges associated with the succesful deployment of large-scale CCS, followed a conceptual design method for the CaStor module:

Because of the long time span of operation of more than three years under steady state, an unmanned platform will be sufficient, significantly reducing the required size, weight and costs. Depending on the exact configuration, the platform will weigh between $500t$ and $1000t$ and can either be placed on a purpose-designed jacket or a monotower. Alternatively, an existing platform or support structure can be used to carry the required equipment, which would reduce costs even further.

7

Acknowledgements

First of all I would like to thank my academic supervisor, Professor Bendiks Jan Boersma, chairman of the Process & Energy Department of the faculty of Mechanical, Maritime and Materials Engineering at Delft University of Technology. Without the monthly progress meetings and his tendency to abruptly challenge me to explain specific details and place them into a broader context, this report would have been a lot less focused and less complete. Furthermore, our in-depth discussions on topics surrounding my research and his fundamental way of reasoning frequently gave me new insights and inspired me to dig deeper.

I would also like to thank my company supervisor, ir. Vincent Doedée, of Heerema Marine Contractors (HMC). While he let me plan and adjust my research project independently, his routine to have me present my progress, setbacks, learnings and goals on a single slide at the beginning of each week forced me to organize and structure my work accordingly from the first day onward. This practice later saved me a lot of time and effort while documenting my research and allowed me to continuously set clear and substantiated priorities. His relentless efforts to connect me to the right people within the Heerema Group also provided me with a great network for criticism and feedback.

Furthermore, I would like to thank the following experts for inspirational talks and feedback during the course of my research: Professor Marco Mazzotti and Dr. Mijndert van der Spek from ETH Zurich, Professor Andrea Ramírez, Professor Ruud Henkes and Dr. Denis Voskov from Delft University of Technology, Dr. Matteo Gazzani from Utrecht University and ir. Paul van Riel with his extensive experience in geophysics.

In addition, I would like to express my gratitude to HMC for the opportunity, the interesting research topic, the great atmosphere and the company resources it has offered me over the last nine months. My special thanks go to the HMC's Renewables team: Thank you all for your input, feedback and enthousiasm that made this project fun and memorable.

Last but not least, I would like to thank my family, especially my parents, for providing me with unfailing support and continuous encouragement throughout my years as a student and through the process of this research project. This accomplishment would not have been possible without them.

C.P.W. Christiaanse
Amsterdam, November 2018

A
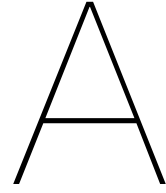
Validation

In this section, the models developed for this thesis will undergo different procedures to make sure that they accurately fulfill their intended purpose.

A.1. Transport from shore to platform

A.1.1. Heat transfer

First, the assumption of the validity of the lumped thermal capacity model is checked: Using the average heat transfer coefficient calculated with equation 3.21, $Bi \approx 0.19$. This is higher than the $Bi < 0.1$ commonly used to legitimize the lumped thermal capacity model and means that temperature differences within the pipe wall exceed 5% [82].

Next, equation 3.28 is solved analytically to see if the resulting temperature of the CO_2 as a function of distance matches that of the numerical model. The resulting graph in figure A.1 shows practically the same temperature as a function of distance as figure 4.6.

$$T(x) = T_0 - \frac{e^{-a(x+b)} - a \cdot T_e}{a}, \quad where \quad b = \frac{ln(a(T - T_e))}{-a} \quad and \quad a = \frac{1}{(1/2 \cdot R_{sea} + 1/2 \cdot R_{soil}) \cdot \dot{m} \cdot c_p}$$

$$(A.1)$$
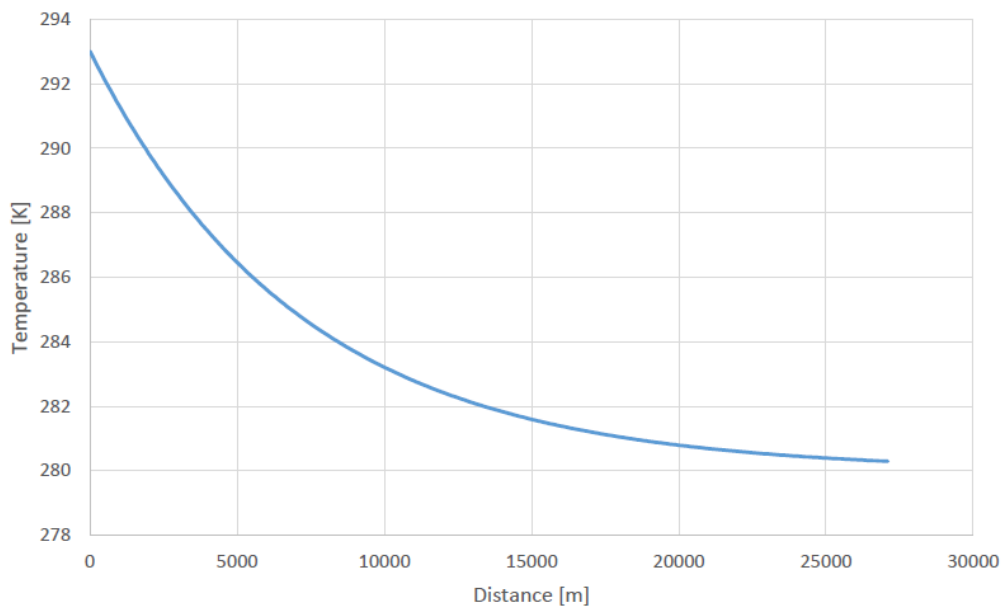
Figure A.1: Analytical solution for the fluid temperature as a function of distance.

A.1.2. Pressure loss

The pressure drop over a section of pipe that is calculated using the Darcy-Weisbach equation can be graphically validated using the Moody diagram as shown in figure A.2. It is a graph in non-dimensional form and relates the friction factor, Reynolds number and relative surface roughness for fully developed flow in a pipe.

The Reynolds number and relative roughness for the transport pipe are calculated for the $0.66m$ pipe shown in figure 4.3b and listed in table A.1 below.

$$Re = 7.825 \cdot 10^6$$
$$\frac{\epsilon}{d} = 8 \cdot 10^{-3}$$

Table A.1: The Reynolds number and relative roughness for the flow in the transport pipe from section 3.4.1

Inserting them into the Moody diagram shown in figure A.2 results in an approximate friction factor of $f = 0.036$.

$$\Delta P = f \cdot \frac{\rho u^2 l}{2D} = 0.036 \cdot \frac{858 \cdot 1.165^2 \cdot 10^4}{2 \cdot 0.66} = 317590 \; Pa \approx 0.32 \; MPa \tag{A.2}$$

Dividing this pressure drop by the pressure of the inflow yields the percentage of pressure lost:

$$\frac{0.32}{12} = 0.0266 = 2.7\% \tag{A.3}$$

According to the results from the MATLAB model, the pressure drops $0.274 \; MPa$ over the length of $10km$. This results in

$$\frac{0.274}{12} = 0.02283 = 2.3\% \tag{A.4}$$

This is 14.8% less than the pressure drop derived from the Moody chart, just within its assumed $\pm15\%$ range of accuracy [98].
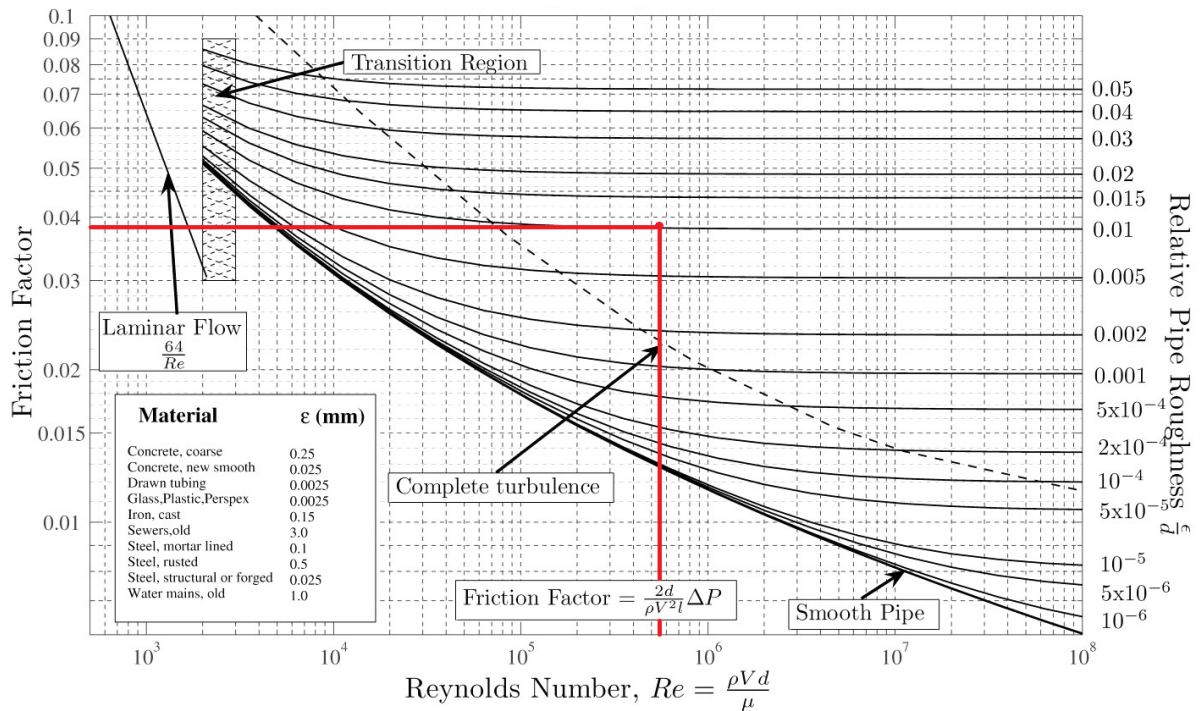
Figure A.2: Moody chart for pipe friction with smooth and rough walls, along with a geometric approximation of the friction factor [93].

A.2. Transport from platform to reservoir

A.2.1. Heat transfer

The first step to verify this part of the model is to test it under two extreme scenario's: One where the mass flow rate is divided by 10 and one where it is multiplied by 10. The scenario with the lower mass flow rate should show a smaller lag in temperature between the surroundings and the liquid inside the pipe - meaning that T_c will be reached at a much smaller depth. Similarly, the higher mass flow rate scenario should result a bigger lag in temperature increase, meaning that T_c is reached at a much greater depth.

(a) $\dot{m}/10$ (b) $\dot{m} \cdot 10$
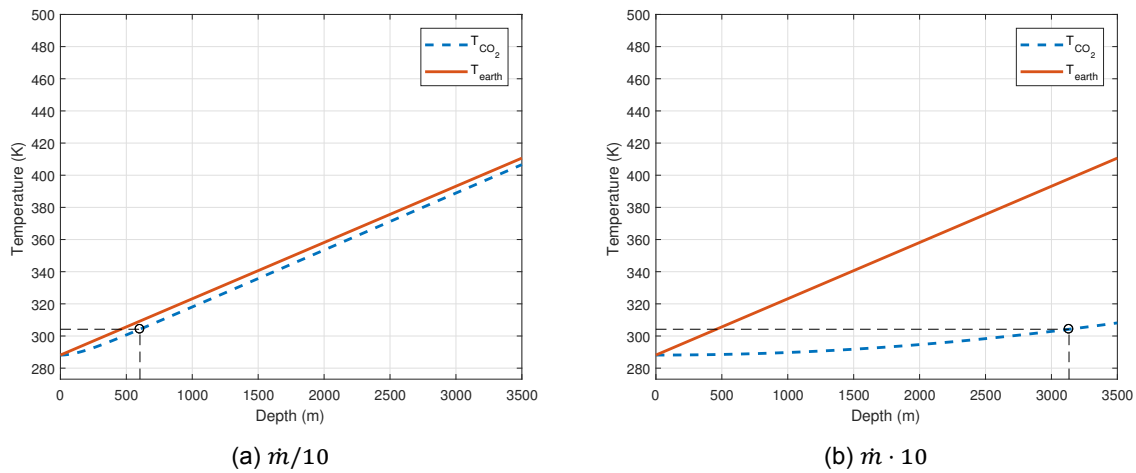
Figure A.3: The resulting temperature development from two extreme scenarios, along with the different depths at which T_c is surpassed.

As expected, there is a big difference in the lag between the two scenarios: While the low $\dot{m}$ T_c is already reached after $603m$ - the high $\dot{m}$ case reaches T_c only after $3133m$.

Next, the model is evaluated at a fixed mass flow rate of $350 \ kg/s$ for two other substances with a different c_p, water (H_2O) and ammonia (NH_3), whose properties are listed in table A.2. The results are plotted in figure A.4

Fluid	$\rho \ [\frac{kg}{m^3}]$	$c_p \ [\frac{J}{kgK}]$	$\mu \ [Pa \cdot s]$	$k \ [\frac{W}{mK}]$	Pr	$T_c \ [K]$	$p_c \ [MPa]$
CO_2	878	$2.425 \cdot 10^3$	$0.86 \cdot 10^{-4}$	0.1015	2.061	304.2	7.38
H_2O	1003	$4.15 \cdot 10^3$	$9.98 \cdot 10^{-4}$	0.6039	6.857	647.1	22.06
NH_3	619	$4.64 \cdot 10^3$	$1.47 \cdot 10^{-4}$	0.5191	1.315	405.5	11.28

Table A.2: Properties of the reference substances at 15 °C and $12 \ MPa$ [60]

Just as expected, the ammonia takes the longest to heat up, followed by the water - the CO_2 heats up the fastest. H_2O and NH_3 also have a much higher critical point than CO_2, meaning that they would become supercritical at much greater depth. The Re of all substances is also in the range recommended by Churchill and Bernstein [91], as shown in table A.3.
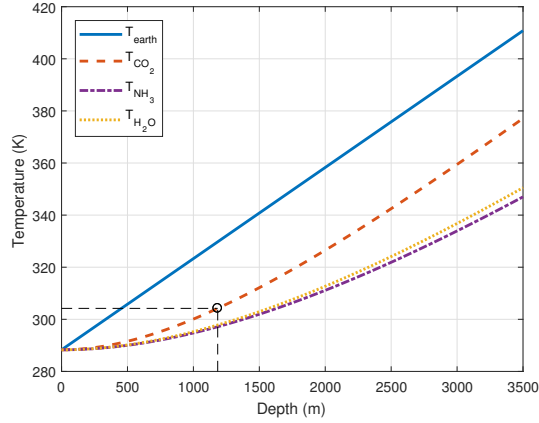
Figure A.4: The temperature of the transport medium inside the well pipe as a function of depth for each substance.

Fluid	u	Re
CO_2	49.1	$4.7 \cdot 10^7$
H_2O	44.36	$0.39 \cdot 10^7$
NH_3	71.1	$2.9 \cdot 10^7$

Table A.3: The flow velocities and Reynolds numbers of the compared substances

In the article *"Flow Rates Measurement and Uncertainty Analysis in Multiple-Zone Water-Injection Wells from Fluid Temperature Profiles"*, the authors aim to reproduce experimental well fluid temperature profiles during cold water injection using a computer program based on the Ramey method [99][100]. The input parameters for their model are shown in table A.4 and will be used in an attempt to reproduce their results using the computer model developed for this thesis.

T_{in}	14.7	[°C]
$T_{surface}$	21.11	[°C]
$\dot{V}$	8.814	$[\frac{m^3}{s}]$
r_i	0.08	$[m]$
z	2000	$[m]$
$\frac{dT}{dz}$	0.0151	$[\frac{°C}{m}]$

Table A.4: Input parameters used by Reges and Salazar in their research on the reproduction of temperature profiles of well fluids during cold water injection [99]

Figure A.5 shows the graphs of both programs; the first graph shows the temperature profile of the well fluid according to the model developed by Reges and Salazar. The second shows the temperature profile according to the computer model developed for this thesis. While the water temperature in the first model reaches about 19.2 °C (292.3 K), the final temperature of the second model is 19 °C (292.15 K).
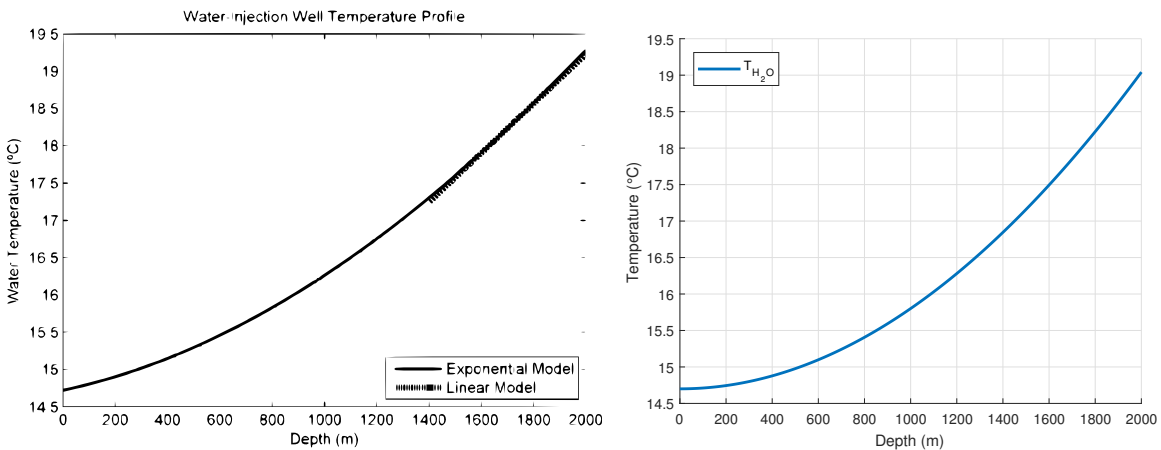
(a) Temperature profile of the well fluid during cold water injection from Reges and Salazar [99].

(b) Temperature profile of the well fluid during cold water injection according to model developed for this thesis.

Figure A.5: Comparison of well fluid temperature profiles during cold water injection.

A.2.2. Injection into the reservoir

The first step in validating the model used to compare the total mass inside the reservoir using the model and a simple calculation: Figure 4.9a shows that the mass flow rate stays at its maximum of $350kg/s$ for the first 2.5 years. Multiplying the mass flow rate by 2.5 years results in a total stored mass of 27.6 Mt, just like the graph in figure 4.9b.

Next, the filling process is repeated without restricting the mass flow rate to $350kg/s$. The resulting mass flow rate as a function of time is shown in figure A.6a and compared with that of filling the hydrogen tank of a car [101]. While the former occurs over a time scale of almost three years, the latter takes place in only 35 seconds. Still, the graphs show similar characteristics during the filling process: Once the valve is opened, the mass flow rate instantly increases before reaching its local maximum and then starts to decreasing linearly.
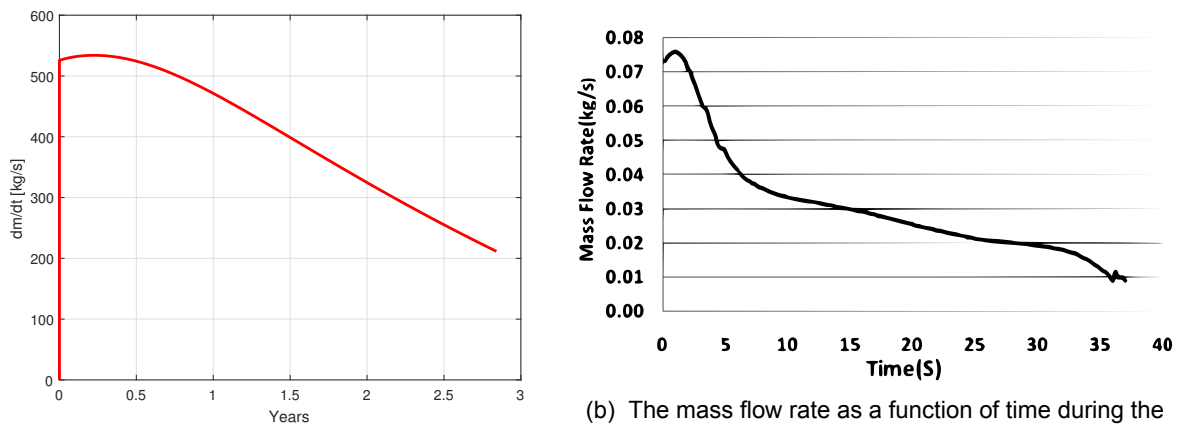
(a) Unrestricted mass flow rate as a function of time for the P18-2 reservoir.

(b) The mass flow rate as a function of time during the filling of a hydrogen tank [101].

Figure A.6: Comparison of mass flow rate as a function of time during injection.

The flow speed inside the injection well is calculated using both ways described in equation 3.48: First by dividing the mass flow rate by the density and cross-sectional area, then using the difference in enthalpy. Both yield a speed of about $49m/s$.

Last, the mass flow rate as a function of time is evaluated for two alternative overall pressure differences between the supply flow and the tank. Figure A.7a shows the mass flow rate for $\Delta p \cdot \frac{1}{2}$, figure A.7b for $\Delta p \cdot 2$. Just as expected from equation 3.46, the mass flow rate scales with the square root of the pressure drop-multiple.

(a) $\Delta p \cdot \frac{1}{2}$ (b) $\Delta p \cdot 2$

Figure A.7: Unrestricted mass flow rate as a function of time for two alternative pressure differences.

B

Economic & Policy framework

While the necessary technologies and supply chains are already fit for purpose, long lead times in regulation, planning and construction have slowed the large scale deployment of CCS initiatives so far [102].
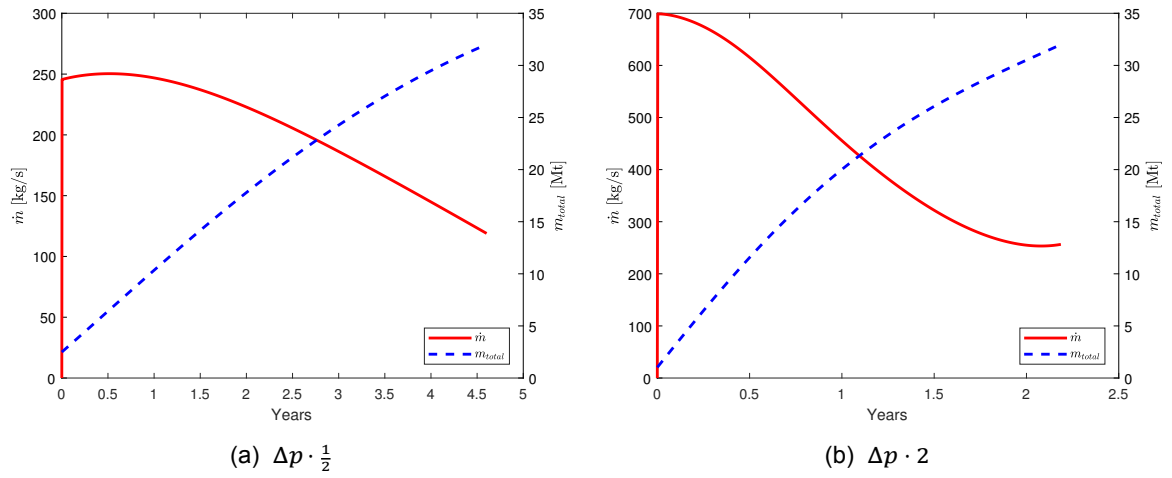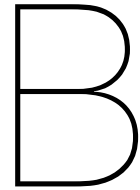
Furthermore, there currently is little or no commercial driver to reduce CO_2 emissions in the majority of regions and industries where CCS is expected to play a role. As most potential sectors operate in competitive international markets, additional costs associated with CCS cannot be passed on to consumers, making it hard to come to a profitable business case. This section aims give a brief overview of the economics and policies associated with the successful deployment of CCS.

B.1. Emission reduction policies

Most CCS applications are at an early stage of commercialization and, therefore, at the top of the cost curve. This requires a significant effort to accelerate its deployment and calls for strong and clear technology-neutral emission reduction policies on a global scale. This section provides an overview of the three instruments that can be used by policy makers to stimulate the technology's progress [103].

B.1.1. Result-based climate financing

Result-based financing (RBF) is a financing approach under which an investor disburses funds to a recipient once a result is delivered, contrary to the the case of upfront financing. It implicates that new initiatives will need to secure pre-financing in addition to the conditional financing they will eventually receive. Result-based climate financing (RBCF) is defined as RBF that specifically targets climate mitigation projects. RBCF does not need to compete with existing financial instruments such as upfront grants, loans and guarantees, but should be used to complement them instead [104].

B.1.2. Emission Taxes

Emission taxes are commonly known as carbon taxes and are levied on the carbon content of hydrocarbon fuels, most notably coal, petroleum and natural gas. Since the greenhouse gas emissions due to the combustion of these fuels are closely linked to their carbon content, a carbon tax can reduce CO_2 emissions without significantly altering the economy [105]. Long-term investors can use carbon pricing to analyze the potential impact of climate change policies on their investment portfolios, which allows them to revise investment strategies and reallocate capital toward low-carbon or climate-resilient activities. But while emission taxes guarantee the price of emissions in the economic system, their effect on the environment is uncertain, as they do not impose a limit on emissions.

The World Bank Carbon pricing dashboard provides an overview and key statistics on regional, national and subnational carbon pricing carbon pricing initiatives [106].

B.1.3. Emission Trading Systems

An ETS operates under a cap and trade principle: a central authority issues a limited number of allowances to emit a specific quantity of a specific pollutant per time period, and the cap is the sum of all allowances. The cap is often subject to a periodic curtailment mechanism to achieve a continuous reduction in emissions [107].

All parties in the ETS are required to hold an amount of allowances equal to their emissions, and any increase in emissions requires them to buy allowances from others willing to trade them. While traditional regulation offers no incentive to go beyond the regulatory standard, an ETS provides an incentive for continuous innovation in emission reduction. The underlying hypothesis is that polluters who can reduce their emissions most efficiently will do so and hereby free up allowences that can be sold to others. [108]. Contrary to emission taxes, an ETS does provide certainty about its environmental impact as it limits the total amount of emissions, but its price remains flexible and depends heavily on the enforcement of allowance reduction. For example, the 2008 economic crisis led to emissions reductions that were greater than expected. This led to a large surplus of allowances, which weighed heavily on the carbon price and reduced the effectiveness of the system [109].

EU ETS

The EU ETS is the world's largest emissions permit market to date, covering almost half of the total CO_2 emissions of the EEA. The total cap is set to fall by 1.74 % annually between 2013 and 2020, which will increase to an annual reduction of 2.2% after 2020 [110]. It covers emissions from nine industry sectors designated by activity codes, which total over 11'000 individual installations [111] [112].

- (1) Power & Heat

- (3-5) Metals & Coke

- (6) Cement & Lime

- (2) Oil & Gas

- (7-8) Glass & Ceramics

- (9) Pulp & Paper

Firms can trade allowances within the EU and by April 30 of each year, permits corresponding to their emissions in the previous calendar year must be handed in. This is also the date when each installation's externally verified emissions from that year are published by each country - the penalty for non-compliance is 100 euros for every ton of emitted CO_2 for which firms to not have an allowance. In addition, the missing allowances must be surrendered in the following year.
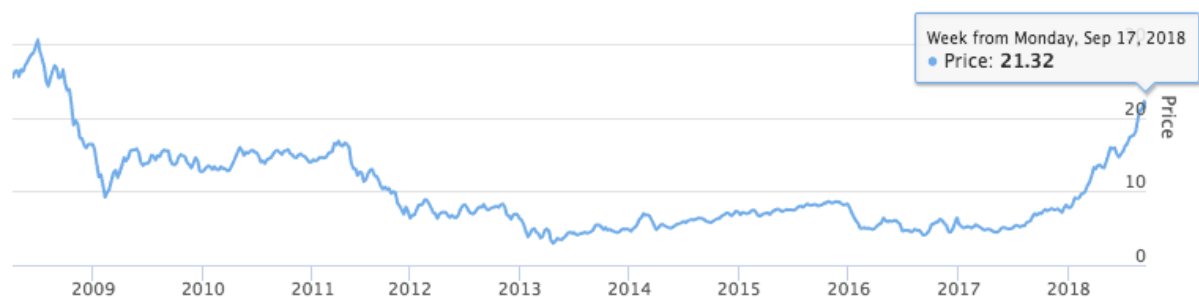

Figure B.1: Graph showing historical EU ETS price per ton CO_2 [113]

The allowance price per ton of emitted CO_2 has dropped sharply in 2009 after emission data over the year 2005 were released, revealing an oversupply in emission rights. After remaining at around 5 euros per ton for almost ten years, the price increased to over 20 euros again

last august, after the EC announced it would exclude a number of permits from the market next year [114]. In a consultation to the EC, the Global CCS Institute advises a "*structural reform of the EU ETS after the 2020 period to restore long-term confidence in the business case of CCS and achieve emission reduction targets*", along with key policy observations and advice to realize these reforms [42].

B.2. Estimated costs

This section provides a brief overview of the costs that are associated with the construction and operation of the CO_2 transport and storage chain.

B.2.1. Capture and compression of CO_2

Most research estimates of the costs to capture one metric ton of CO_2 range from €20-90, leading to a great deal of uncertainty of the true costs of implementing and operating CCS installations [115]. In 2017, a study by EBN and Gasunie narrowed down the expected costs for installations in the Netherlands that are likely to be part of future CCS initiatives. The full cost matrix is shown at the end of this appendix in figure B.6.

[€/ton]	Low volume	Mid volume	High volume
Capture	75	65	55
Onshore transport	1.05	0.53	0.53
Central compression	3.05	3.05	3.05
Total	79.1	68.5	48.6

Table B.1: Overall costs for the capture, onshore transport and central compression per ton CO_2 [67]

B.2.2. Transport pipeline

The material costs are a function of the dimensions, the density and the steel grade, as shown in equation B.1:

$$C_{material} = t \cdot \pi \times (OD_{NPS} - t) \times L \times \rho_{steel} \times C_{steel} = €20.39M \tag{B.1}$$

The individual parameters are listed in table B.2 below, along with the values derived from the boundary conditions of the case study for P18-2:

t	0.02	$[m]$	Wall thickness
OD_{NPS}	0.7	$[m]$	Outer diameter of the nominal pipe size
L	40'000	$[m]$	Pipeline length
ρ_{steel}	7900	$[\frac{kg}{m^3}]$	Density of steel
C_{steel}	1.51	$[\frac{€}{kg}]$	Steel cost (S550QL) [116]

Table B.2: Parameters for pipeline material costs calculation [117]

For offshore pipelines, labor costs are significantly higher than for onshore pipelines since they require special pipelay barges and risers. The onshore - offshore landfall is costly and the connection to the injection point is more complicated than onshore, which brings fixed additional costs of about €35M, independent of the pipe's length [118]. The additional variable labor costs for offshore pipelines amount to approximately $845\frac{€}{m^2}$ [117]. For a $40km$

pipeline of $0.66m$ diameter, this amounts to around €176'000. Adding the fixed additional costs mentioned above amounts to a total of €35.17M.

Most literature calculates O&M costs as a percentage of the total capital costs, ranging from 1.5 to 4% [119] [120]. This means that O&M costs for the P18-2 pipeline will range between €0.83M − 2.22M per year.

B.2.3. Pump & heater

The design of a water pump does not differ significantly from a liquid CO_2 pump, so the cost of water pumps is used as an approximation to determine the cost of the pumps [121].

$$E_{pump} = \frac{p_2 - p_1}{\eta_{pump} \times \rho} = 2.5 \ [\frac{kJ}{kg}]$$
(B.2)

$$P_{pump} = E_{pump} \times \dot{m} = 875 \ [kW]$$
(B.3)

p_1	11	$[MPa]$	Inlet pressure
p_2	12.5	$[MPa]$	Outlet pressure
η_{pump}	0.75	$[-]$	Pump efficiency
ρ	800	$[kg/m^3]$	Fluid density
$\dot{m}$	350	$[kg/s]$	Mass flow rate

Table B.3: Parameters to calculate pump capacity

The maximum capacity of a liquid CO_2 pump is around 2 MW [122], so for larger capacities, two pump units with similar capacity will have to be installed in parallel. However, it might be beneficial to install multiple pumps with lower capacities in parallel, as this configuration can better handle variations in mass flow. A train advantage is determined using a multiplication factor [123].

$$I_{pump} = 74.3 \times 10^{-4} \times P_{pump}^{0.58} \times n^{me} = €1.3M$$
(B.4)

P_{pump}	500	$[kW]$	Capacity per pumping unit
n	4	$[-]$	number of units in parallel
me	0.9	$[-]$	Multiplication exponent

Table B.4: Parameters to calculate pump costs [124]

The fixed O&M costs for pumping units are often expressed as a percentage of their capital costs, ranging from $1.5 - 5\%$, which results in €0.295M − 0.98M per year [119] [122].

While no heater is required for the P18-2 boundary conditions used in this thesis, different environmental conditions might require additional heating. The Mollier diagram from figure 2.6 can be used to determine how much energy is required for the desired heating step. The heating costs are estimated at $1\frac{M€}{MW}$ and O&M costs account for 4% of the capital costs [125].

For example, to heat a liquid flow of CO_2 from 0 °C to 5 °C at a pressure of $10MPa$, figure 2.6 indicates that around $12.5\frac{kJ}{kg}$ are required. At the reference mass flow rate of $350\frac{kg}{s}$, this results in a heater capacity of $4.375MW$; with an associated cost of €4.375M. O&M then results in a yearly cost of €175'000.

B.2.4. Total costs for transport & storage

Using the resulting costs from each unit, the total costs for the P18-2 case study can be determined, as shown in table B.5 below:

	New	Reuse	New & Reuse
	Capex [€]	Capex [€]	Opex [€/$year$]
Transport pipeline	55.56M	1M	2.22M
Platform	22M	5M	2.5M
Pump units	19.7M	19.7M	0.98M
Heater	-	-	-
Total	75.26M	25.7M	5.7M

Table B.5: Overall cost calculation for P18-2 case study [67] [124]

Considering a total storage capacity of 40Mt over a period of 3.5 years, the cost offshore transport and storage per ton CO_2 is calculated as follows:

In case no existing equipment can be reused, the fixed costs plus O&M costs over time result in a total cost of €95.21M; or €2.95/ton. But when the existing transport infrastructure and pipeline can be reused, as is assumed in the case of P18-2, the total costs reduce to €45.65M; or €1.42/ton, representing a reduction of almost 52%.

While this presents a good approximation, the final costs will much likely be even higher because other factors must be included, such as financing costs, insurances and investor yields.

B.2.5. Combined costs

The costs from the previous section are now combined with the costs associated with the P18-2 case study used in this thesis to determine a final price of capturing and storing a metric ton of CO_2.

In the best scenario, where existing offshore infrastructure can be used to transport and store high volumes of CO_2, the total costs would be €50.02/ton. While it is likely that existing infrastructure can be reused, the high volume case requires a huge capture and onshore transport network, which makes it unrealistic to assume this will happen within the next decade. In the first years, when volume is low to medium, the price will amount to €80.52/ton and €69.9/ton, respectively. The requirement of a new platform drastically increases these costs to €82.05/ton.

B.2.6. Policy gaps

Before large scale CCS projects can be initiated, a completely new regulatory system must be set up: A framework for a consistent monitoring system and a legal structure for the responsibilities of each party, amongst others. The main subject that still has to be solved is the long-term liability: Who is responsible for monitoring the storage locations for the next 100 years? Who is responsible if the stored CO_2 starts to leak after 50 years? Since no company can be asked to reserve billions of euros in case one of their storage reservoirs fails at some point in time, the most likely outcome is that the responsibility is transferred to a state institution like the Dutch NAM once the storage process has ended - similar to the responsibility structure for conventional oil- and gas fields [54] [126].

Furthermore, the policy framework of the EU ETS in its current form is too narrow: Since it focuses only on certain industries, polluting emitters outside of its umbrella face no incentive to reduce their emissions [126].

B.2.7. Conclusion

Once CCS is deployed on a large scale, with high volumes of emissions being captured and stored, the price per ton is estimated at around €50, depending highly on the applied capture technology. This means that the current price of CO_2 emissions must increase by a 150%. However, once the price increases above that threshold, significant returns can be made by storing CO_2.

Large scale CCS is often cited by the media as an innovative technology that can help reduce anthropogenic emissions. However, the technologies used to capture, transport and store the CO_2 have been around since decades. The real thing holding back the large scale deployment - and therefore the success - of CCS are the policy gaps and uncertainties that undermine the long term confidence in the business case. The EU ETS is a step in the right direction by laying the ground work for a price on carbon emissions, but still has serious shortcomings that result in significant price fluctuations. In 2020 the next phase of the EU ETS comes into effect, for which the Global CCS Institute has proposed a set of structural reforms to restore long term confidence in the business case [42].

B.3. Indicative capture costs

Sector	Process	Costs of captured CO_2 [€/t]
Refining	Hydrogen production	33 (23-42)
	Hydrogen production	79 (42-126)
	Process heaters	99 (79-128)
	Heating power	104 (42-126)
Iron & steel	Blast furnace	53 (30-79)
	Hot stoves, power/steam plant	71 (71-85)
	Cokes oven	83 (83-92)
Chemicals	Ethylene oxide	15
	Hydrogen (ammonia/methanol)	34 (18-43)
	Ethylene/propylene	71
	Process heaters/ heating power	101 (41-126)
Gas processing	Gas processing	12
Paper & cardboard	Kraft process	67 (34-69)
Cement	Pre-calcinator	37 (21-50)
	Complete installation	61 (35-111)
Biofuels	Ethanol	15
Aluminium	Smelting furnace	15
Electricity	Coal post-combustion	57
	Coal pre-combustion	43
	Coal oxyfuel	51
	Gas post-combustion	79

Table B.6: Indicative capture-costs per ton CO_2 for typical industrial processes [67]

$$C$$
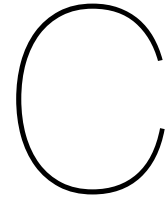
Module design

To maximize circular efficiency, the goal is to construct a reusable module that can be both retrofitted to old platforms and placed in new platform configurations. This section provides an overview of the design considerations and the required equipment for the design of the CaStor module.

C.1. Design considerations

Conditioning and injection equipment for CO_2 require an understanding of its unique thermal and physical characteristics and its proneness to corrosion in the presence of water. Furthermore, its partial pressure and the composition of impurities can have a significant influence on its thermodynamic behavior and corrosion rates [127].

Pressure

The equipment must be sufficiently designed to handle the high pressures along the different sections. The module will experience pressures in the range of up to $15 MPa$, as calculated in chapter 4. However, this is based on a steady state situation. Dynamic behavior during start-up and shut-down processes will likely lead to even higher pressures, which must be modeled before a final design of the module.

Corrosion

Dry and pure CO_2 is virtually non-corrosive at temperatures below 400 °C. But in the presence of water it forms carbonic acid, who's corrosiveness increases along with the partial pressure of the CO_2. On the other hand, experimental observations have shown that small amounts of H_2S reduce the uniform corrosion rate - this effect is attributed to the formation of an iron sulphide corrosion products layer [127]. This means that either the moisture content in the CO_2 has to be removed, or the environments where the CO_2 mixture becomes corrosive must be properly protected - the latter can be achieved with corrosion-resistant construction materials or corrosion inhibitors. It is not realistic to assume the use of exotic materials and coatings that are resistant to corrosive CO_2 compositions, as this will increase costs by several orders of magnitude. Instead, the CO_2 should be dried and purified before it is transported.

Thermal stresses

The temperature of the CO_2 will remain between 5-35 °C along the whole chain, which means that there will be no critical thermal stresses during normal operation. However, in case the pressure builds up in one of the sections, the CO_2 must be released through a relief valve, where it will drastically expand and transition into gas phase. Due to this rapid expansion, Joule-Thomson cooling can make local temperatures drop by 80 °C, which can cause local thermal stresses. The graph in figure C.1 shows the Joule Thomson cooling effect for pure CO_2 at different pressures.
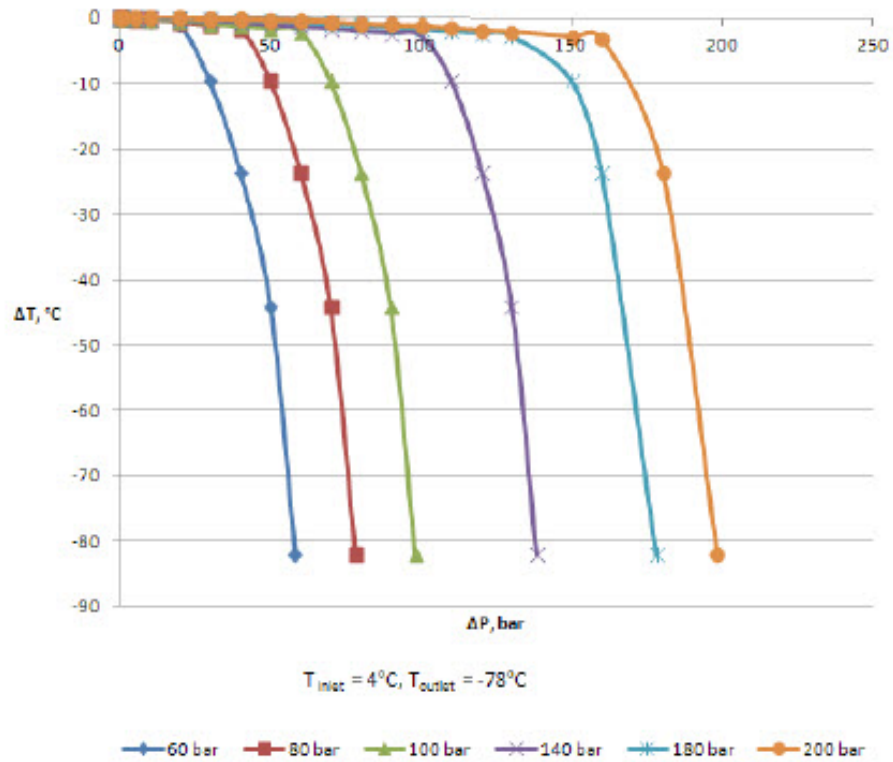
Figure C.1: Changes in temperature as a result of the Joule Thomson effect for pure CO_2 at $4°C$ [59].

C.2. Required components

The following components will be required to build an integrated CO_2 conditioning and injection module [128]:

Pig launcher and -receivers

Pigs are devices used to perform various maintenance operations inside pipelines. This is usually done without stopping the flow inside the pipeline. It works by inserting the pig into an oversized section of pipe which gradually reduces to the normal diameter, called the "launcher". From here the pressure-driven flow inside the pipeline pushes the pig until it reaches the "receiver" or "catcher" further downstream, where it is taken out [129].

Figure C.2: **Left:** A pig launcher for a gas pipeline. **Right:** A pig being inserted into a pig launcher. The yellow plastic disks seal against the inside of the pipe to propel the device and to remove loose sedimentation or scale buildup [130]

Pipe for high pressure liquid

Especially when existing pipelines are reused, standard hydrocarbon piping diameters and -thicknesses will apply. Depending on the concentration and amount of impurities, specific material properties may be required to limit corrosion. Several key factors that influence the design of offshore pipeline systems: The distance from shore to the storage location impacts the final pressure and capacity, which, in turn, may influence the wall thickness and optimal pipe diameter. Pipelines that have been deployed to transport gas are commonly damaged the least, whereas those for oil transport are likely to have spatial differences in wall thickness due to local corrosion. Furthermore, the condition of an oil pipeline depends heavily on its operational history; the amount of water in the stream, the amount of time it was in idle mode and the employed corrosion management regime. Moreover, most oil pipelines are not designed for pressure ranges needed to keep CO_2 in its liquid phase, making them less suitable for reconversion [129].

Pressure boosting pumps

A pumping stage that increases the pressure of liquid CO_2 if its arrival pressure is below the intended pressure of the filled reservoir. Because of the comparable density and lower viscosity of liquid CO_2, the design of a suitable pump does not differ significantly from a common water pump [127] [121].

Close attention must be paid to local pressure differences around the pump, as cavitation bubbles can cause significant damage to the equipment [131]. It should be noted that offshore boosting of CO_2 should be avoided if possible, as this significantly increases the complexity and costs of the platform.

Heater

An auxiliary heater will be required if geothermal heating is not sufficient to bring the CO_2 into its supercritical state.
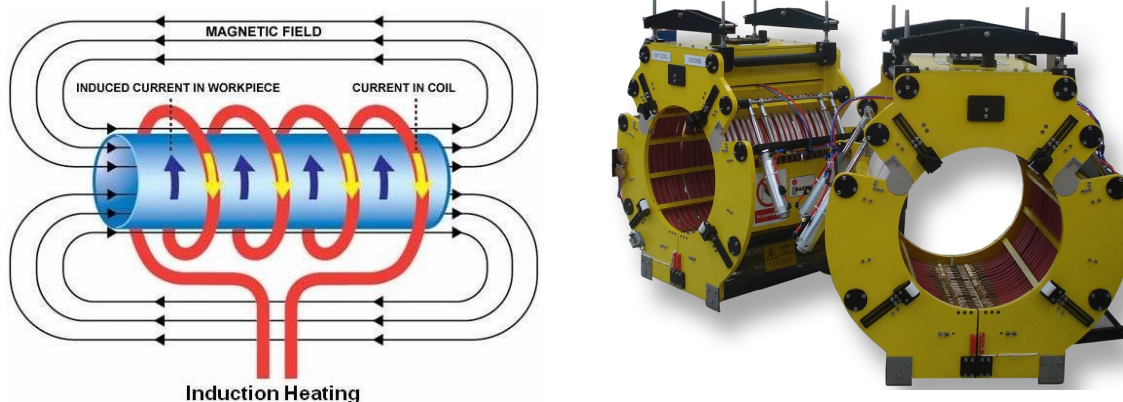
Figure C.3: **Left:** Geometry of and physical processes inside an induction pipeline heater. **Right:** An offshore clam heating coil that can be placed around a pipeline [132]

Riser

The riser is the section of pipe which transports the fluid between the platform and the seabed. Many oil and gas platforms use (partially) flexible hoses, especially on floating production installations. It is plausible that the materials used in these parts will not be suitable for liquid CO_2 transfer and therefore need to be replaced.

Pipe constriction

A transfer section, where the liquid CO_2 flows from the wider transport pipe into the narrower well pipe

Measurement & control systems

Both on- and offshore storage of CO_2 will require an extensive monitoring system to ensure that the reservoir integrity remains intact and the CO_2 does not leak. Furthermore, any migration of CO_2 within the reservoir must be monitored to adapt filling procedures. Figure C.4 shows the three key regions that are defined in the EU's CCS directive for monitoring carbon injection. The diagram does not necessarily denote spatial or stratigraphic relationships, as this will be based on site-specific conditions [133].
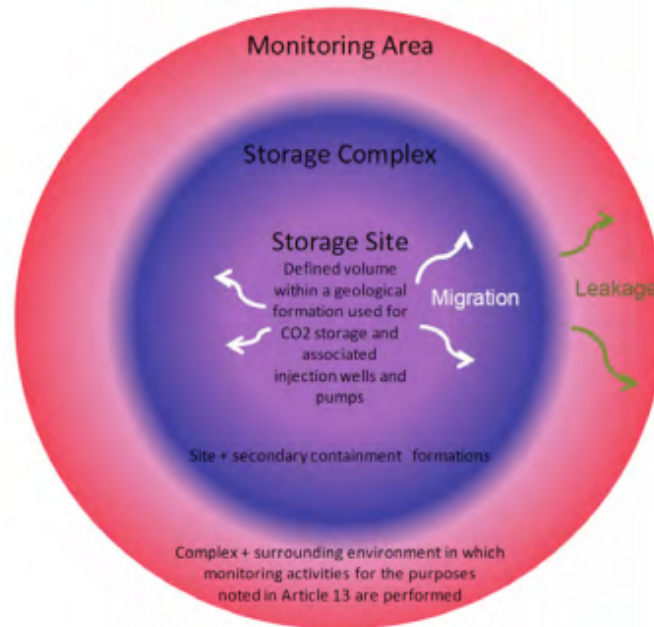

Figure C.4: Schematic diagram of the three different monitoring zones defined by Directive 2009/31/EC on the monitoring of Geological Storage of Carbon Dioxide [133].

Emergency shutdown valves

This concerns a valve positioned between the transport pipe and the riser to the platform and functions as a fail-safe device to ensure that a failure on the platform does not result in an accidental release of CO_2 from the complete pipeline network. Emergency shutdown valves are usually located on the seabed, just inside the safety zone of platforms to prevent any damage from ship operations.

Seals

Over the whole network, specifically designed mechanical seals are installed which are flooded with high pressure nitrogen. A very small portion of nitrogen leaks into the flow of CO_2 at all times, which keeps it away from the elastomeric seals. This eliminates the risk of explosive decompression of the seals when the unit is shut off and pump pressure declines.

Venting systems

Liquid CO_2 in a static tank will reach a vapor-liquid equilibrium point, where the vapor phase at the top is just above its boiling point and the liquid phase underneath is just below the boiling point. Changing the pressure or temperature of the tank will change this equilibrium. Here the Joule-Thomson cooling effect plays a major role, as the pressure difference between the in- and outside of the pipe will be significant. Thermal stresses caused by the JT effect can cause ruptures and other failures to the equipment.

Should it be necessary to reduce the pressure of inside the pipe to atmospheric pressure, it should therefore happen slowly so that the temperature can adjust accordingly and the formation of solids is prevented. This means that venting systems should be located at various positions along the CO_2 transport pipes.

Generating capacity
A significant part of this equipment requires energy to operate. Since installing a cable from shore will not always be possible, this energy might have to be generated offshore. While solar- and wind energy are preferred sources, there must always be a redundant backup generator in place to ensure a continuous operation.

C.3. Energy consumption
Conventional manned offshore platforms in the North Sea typically require between $50 - 100MW$ to power their operations [134]. The CaStor will only need a fraction of that; approximately $5MW$.

Pump
The required properties are listed in table B.3 and are used to calculate the pumping energy per unit mass:

$$E_{pump} = \frac{p_2 - p_1}{\eta_{pump} \times \rho} = 2.5 \ [\frac{kJ}{kg}] \tag{C.1}$$

Multiplying the result with the mass flow rate yields the required pumping power.

$$P_{pump} = E_{pump} \times \dot{m} = 875 \ [kW] \tag{C.2}$$

Since the pumping system must be built redundant, the required power can be achieved through different configurations of multiple pumps. Several smaller pumps can be arranged in series to increase the pressure increase, while arranging them in paralell increases the flow rate.

Heater
For example, to heat a liquid flow of CO_2 from 0 °C to 5 °C at a pressure of $10MPa$, figure 2.6 indicates that around $12.5\frac{kJ}{kg}$ are required. At the reference mass flow rate of $350\frac{kg}{s}$, this results in a heater capacity of $4.375MW$.

C.4. Platform type
C.4.1. Repurposing existing platforms
No two existing platforms are the same: They have different amounts of free deck space, installed processing equipment, installations and safety- and control systems. This means that, in case of insufficient deck space, it can either be gained by removing some of this equipment - or by constructing additional decks. Next, new equipment like pumping and heating units and dedicated measurement- and control systems must be installed and connected to both the transport- and well pipe. The P15C platform combination shown in figure C.5 on the next page are also investigated for reuse in transporting and injecting CO_2 and offer sufficient space for the required equipment. Since only one of the platforms would be required for conditioning and injection, the rest can be decommissioned simultaneously.

Determining whether a platform is actually fit for reuse will have to be determined in detail on a case-by-case basis. In the cost calculations it was assumed that all existing equipment on the platforms is fit for reuse, which means that all equipment must have been stored in proper conditions when exploration was ceased. Furthermore, it is assumed that the tubings of the production pipes and wellheads must be replaced. The well itself must also be thoroughly investigated to certify its integrity [67].

Figure C.5: The TAQA P15C platform combination north-east of the Hague [135]

C.4.2. New platform

If an existing platform cannot be reused, a new platform can be installed: This can be a simple monotower platform specifically designed for the conditioning and injection of CO_2. A monotower can be fixed to the seabed with suction anchors and connected to the wells, so that it can be moved to a new storage location once the reservoir is full. Another option is to use a purpose-designed topside that can be placed on the existing support structures.

(a)
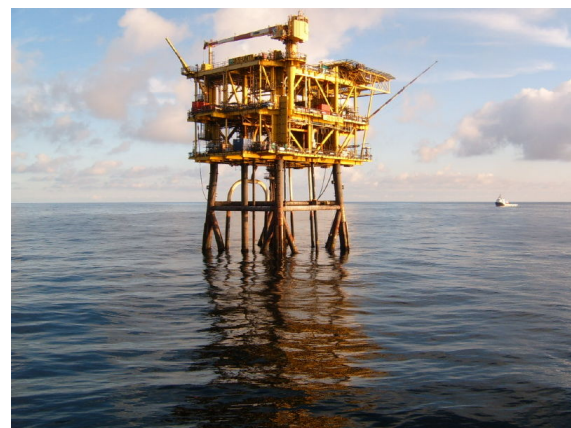
(b)

Figure C.6: Impression of a monopile platform (a) and a small topside installed on an existing support structure (b) [136] [124]

D

Well diagram P18-2

See next page

Figure D.1: Schematic diagram of the P18-4A2 well [70].

Bibliography

[1] P. Sellers, D. Schimel, B. Moore, J. Liu, and A. Eldering. Observing carbon cycle–climate feedbacks from space. *Proceedings of the National Academy of Sciences*, pages 7860–7868, 2018.
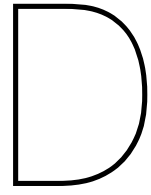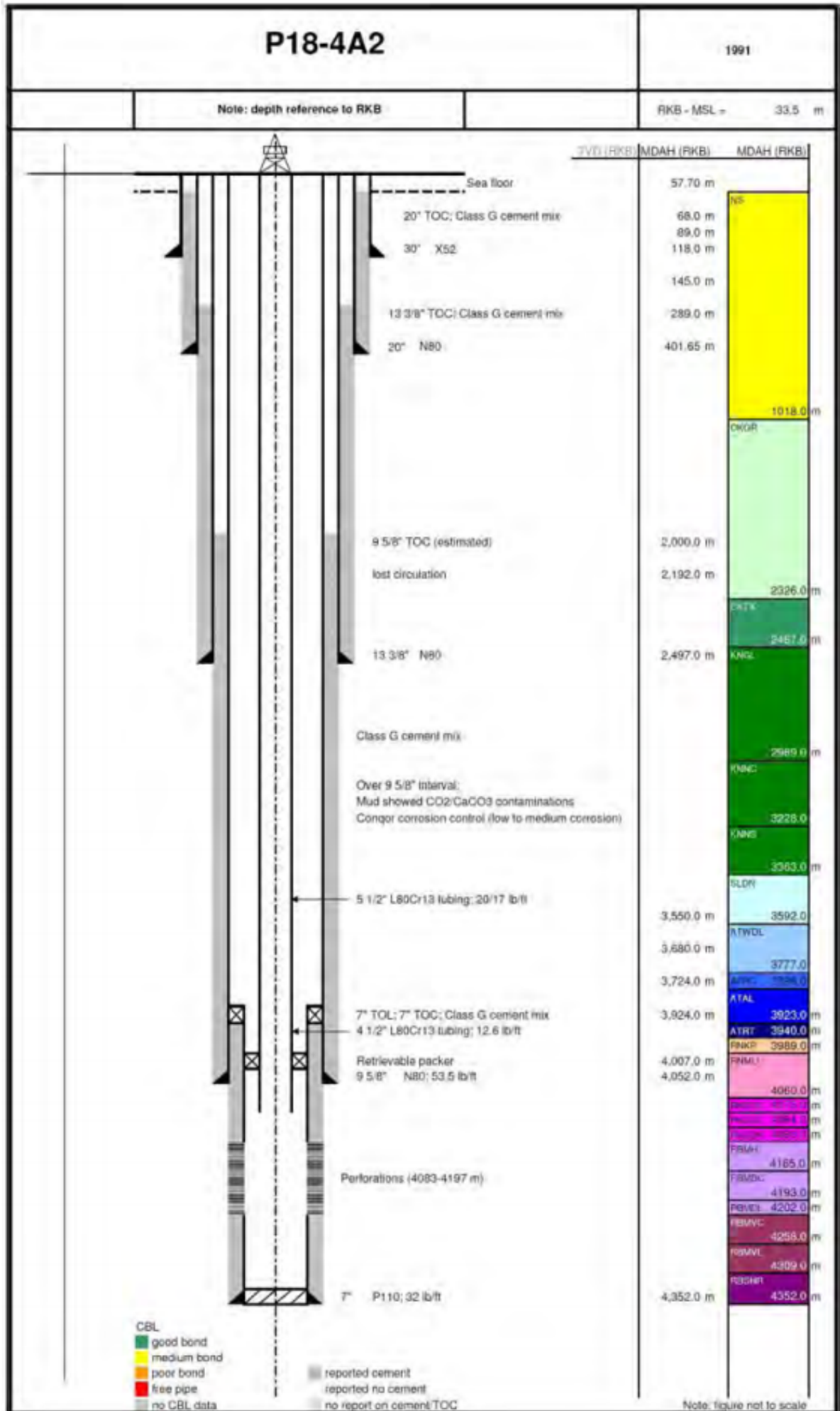
[2] J. Fourier. Remarques générales sur les températures du globe terrestre et des espaces planétaires. *Annales de Chimie et de Physique, 2e série*, 27:136–167, 1824.

[3] J. Fourier. Mémoire sur les températures du globe terrestre et des espaces planétaires. *Mémoires de l'Académie Royale des Sciences de l'Institut de France*, 7:570–604, 1827.

[4] S. Arrhenius and E. Holden. On the influence of carbonic acid in the air upon the temperature of the earth. *Publications of the Astronomical Society of the Pacific*, 9(54):14–24, 1897.

[5] V. Smil. *The Earth's Biosphere: Evolution, Dynamics, and Change.* MIT Press, 2003.

[6] EEA. Climate change, impacts and vulnerability in europe 2016 - an indicator-based report. Technical report, European Union, 2017.

[7] C. Le Quéré, R. Moriarty, R. Andrew, G. Peters, P. Ciais, P. Friedlingstein, S. Jones, S. Sitch, P. Tans, and A. Arneth. Global carbon budget 2016. *Earth System Science Data*, 8(2):605–649, 2016.

[8] T. Stocker, D. Qin, G. Plattner, M. Tignor, S. Allen, J. Boschung, A. Nauels, Y. Xia, V. Bex, and P. Midgley. Climate change 2013: The physical science basis. contribution of working group i to the fifth assessment report of the intergovernmental panel on climate change. Technical report, IPCC, 2013.

[9] National Centers for Environmental Information. Global climate report - annual 2017 state of the climate. Technical report, NOAA, 2017.

[10] T. Stocker, D. Qin, G. Plattner, M. Tignor, S. Allen, J. Boschung, A. Nauels, Y. Xia, V. Bex, and P. Midgley. Climate change 2013 - the physical science basis. Technical report, IPCC, 2013.

[11] United Nations. United nations framework convention on climate change. Technical report, New York, 1992.

[12] United Nations. Kyoto protocol to the united nations framework convention on climate change. Technical report, New York, 1998.

[13] UNFCCC. Report of the conference of the parties on its sixteenth session, held in cancun from 29 november to 10 december 2010. addendum. part two: Action taken by the conference of the parties at its sixteenth session. Technical report, United Nations, 2011.

[14] S. Asefi-Najafabady, P. Rayner, K. Gurney, A. McRobert, Y. Song, K. Coltin, J. Huang, C. Elvidge, and K. Baugh. A multiyear, global gridded fossil fuel co2 emission data product: Evaluation and analysis of results. *Journal of Geophysical Research: Atmospheres*, 119(17):10–213, 2014.

[15] UNFCCC. Paris agreement. Technical report, United Nations, 2015.

[16] V. Hards. *Volcanic Contributions to the Global Carbon Cycle*, volume 10. British Geological Survey, 2005.

[17] O. Edenhofer, B. Knopf, T. Barker, L. Baumstark, E. Bellevrat, B. Chateau, P. Criqui, M. Isaac, A. Kitous, and S. Kypreos. The economics of low stabilization: model comparison of mitigation strategies and costs. *The Energy Journal*, pages 11–48, 2010.

[18] IEA. Energy technology perspectives 2017 - catalysing energy technology transformations. Technical report, Paris, 2017.

[19] ZEP Zero Emissions Platform. Climate change, ccs and why we need it - fast. `http://www.zeroemissionsplatform.eu/carbon-capture-and-storage.html`, mar 2017. Accessed: 2018-03-26.

[20] The global status of ccs: 2016 summary report. Technical report, Global CCS Institute, 2016.

[21] T. Kuramochi, A. Ramírez, W. Turkenburg, and A. Faaij. Comparative assessment of co2 capture technologies for carbon-intensive industrial processes. *Progress in energy and combustion science*, 38(1):87–112, 2012.

[22] J. Pires, F. Martins, M. Alvim-Ferraz, and M. Simões. Recent developments on carbon capture and storage: an overview. *Chemical Engineering Research and Design*, 89(9):1446–1460, 2011.

[23] D. Leung, G. Caramanna, and M. Maroto-Valer. An overview of current status of carbon dioxide capture and storage technologies. *Renewable and Sustainable Energy Reviews*, 39:426–443, 2014.

[24] R. Porter, M. Fairweather, M. Pourkashanian, and R. Woolley. The range and level of impurities in co2 streams from different carbon capture sources. *International Journal of Greenhouse Gas Control*, 36:161–174, 2015.

[25] F. Neele, H. Quinquis, A. Read, M. Wright, J. Lorsong, and D. Poulussen. Co2 storage development: status of the large european ccs projects with eepr funding. *Energy Procedia*, 63:6053–6066, 2014.

[26] M. Knoope, A. Ramírez, and A. Faaij. Investing in co2 transport infrastructure under uncertainty: A comparison between ships and pipelines. *International journal of greenhouse gas control*, 41:174–193, 2015.

[27] A. Arrietta, P. Brickell, V. Camparada, C. Fry, R. Gachot, J. Lewandowski, A. Nielsen, M. Patel, and D. Ritlop. Hazards of inert gases and oxygen depletion. Technical report, European Industrial Gases Association AISBL, 2009.

[28] Advisory Council of the European Technology Platform. The cost of co2 storage - post-demonstration ccs in the eu. Technical report, Zero Emissions Platform, 2011.

[29] C. White, D. Smith, K. Jones, A. Goodman, S. Jikich, R. LaCount, S. DuBose, E. Ozdemir, B. Morsi, and K. Schroeder. Sequestration of carbon dioxide in coal with enhanced coalbed methane recovery a review. *Energy & Fuels*, 19(3):659–724, 2005.

[30] T. Johansson, A. Patwardhan, N. Nakićenović, and L. Gomez-Echeverri. *Global energy assessment: toward a sustainable future*. Cambridge University Press, 2012.

[31] K. Michael, M. Arnot, P. Cook, J. Ennis-King, R. Funnell, J. Kaldi, D. Kirste, and L. Paterson. Co2 storage in saline aquifers — current state of scientific knowledge. *Energy Procedia*, 1(1):3197–3204, 2009.

[32] Working Group III of the Intergovernmental Panel on Climate Change. Carbon dioxide capture and storage. Technical report, IPCC, 2005.

[33] G. Pusch, G. Ionescu, F. May, G. Voigtländer, L. Stecken, and H. Vosteen. Common features of carbon dioxide and underground gas storage. *Oil Gas-European Magazine*, 36(3):131–137, 2010.

[34] IPCC. Special report on global warming of 1.5 °c. *United Nations*, oct 2018.

[35] CBS RIVM. Press release: Co2-uitstoot in 2017 gelijk aan die in 1990. *Centraal Bureau voor de Statistiek*, sep 2018.

[36] S. Samadi, S. Lechtenböhmer, C. Schneider, K. Arnold, M. Fischedick, D. Schüwer, and A. Pastowski. Decarbonization pathways for the industrial cluster of the port of rotterdam. Technical report, Wuppertal Institute for Climate, Environment and Energy, sep 2016.

[37] EBN. Co2 onder de zee: de beste en énige oplossing voor nu. *Focus*, 2018.

[38] OCAP. Press release: Externe co2 noodzakelijk voor klimaatneutrale glastuin-bouw. `http://www.ocap.nl/nl/nieuws/news2017-22-06.html`, may 2017. Accessed: 2018-06-12.

[39] M. Rutte, S. van Haersma Buma, A. Pechtold, and G. Segers. Regeerakkoord 2017: 'vertrouwen in de toekomst'. Technical report, Rijksoverheid, 2017.

[40] E. Wiebes. Kamerbrief over pbl-notitie 'kosten energie- en klimaattransitie in 2030 - update 2018'. `https://www.rijksoverheid.nl/documenten/kamerstukken/2018/04/26/kamerbrief-over-notitie-kosten-energie-en-klimaattransitie-in-2030-update-2018`, 26 apr 2018. Accessed: 2018-06-17.

[41] A. Ellerman and B. Buchner. The european union emissions trading scheme: origins, allocation, and early results. *Review of environmental economics and policy*, 1(1):66–87, 2007.

[42] A. Purvis and S. Vaghi. Submission to the european commission's consultation on revision of the eu emissions trading system (eu ets) directive. *Global CCS Institute*, 2015.

[43] Equinor (Statoil). Carbon storage projects. `https://www.equinor.com/en/how-and-why/climate-change/carbon-storage.html`, feb 2018. Accessed: 2018-09-30.

[44] J. Deflandre, A. Estublier, A. Baroni, J. Daniel, and F. Adjémian. In salah co2 injection modeling: a preliminary approach to predict short term reservoir behavior. *Energy Procedia*, 4:3574–3581, 2011.

[45] S. Bourne, S. Crouch, and M. Smith. A risk-based framework for measurement, monitoring and verification of the quest ccs project, alberta, canada. *International Journal of Greenhouse Gas Control*, 26:109–126, 2014.

[46] Shell Canada. Athabasca oil sands project - quest carbon capture and storage. `https://www.shell.ca/en_ca/about-us/projects-and-sites/quest-carbon-capture-and-storage-project.html`. Accessed: 2018-04-18.

[47] CATO. Program overview. `https://www.co2-cato.org/cato/overview`. Accessed: 2018-06-01.

[48] Global CCS institute Project Database. Gaz de france k12-b co2 injection. `https://web.archive.org/web/20090519234835/http://www.conpacksys.com/html/projects/prod10.html`, may 2009. Accessed: 2018-06-01.

[49] R. de Vos. Linking the chain - integrated cato2 knowledge prepares for the next step in co2 capture & storage. Technical report, CATO, 2014.

[50] ANP. Chronologie co2-opslag barendrecht. `https://www.trouw.nl/home/chronologie-co2-opslag-barendrecht~a82c206d/`, nov 2010. Accessed: 2018-09-27.

[51] Global CCS Institute Project Databse. Road project overview. `http://hub.globalccsinstitute.com/publications/road-ccs-project-non-confidential-feed-study-report/11-project-overview`, jun 2011. Accessed: 2018-08-18.

[52] H. Kamp. Kamerbrief over stand van zaken ccs-project road. `https://www.rijksoverheid.nl/documenten/kamerstukken/2017/06/27/kamerbrief-over-stand-van-zaken-ccs-project-road`, 27 jun 2017. Accessed: 2018-06-17.

[53] Port of Rotterdam. Persbericht: Co2-opslag onder noordzee technisch haalbaar en kosteneffectief. `https://www.portofrotterdam.com/nl/nieuws-en-persberichten/co2-opslag-onder-noordzee-technisch-haalbaar-en-kosteneffectief`, apr 2018. Accessed: 2018-09-27.

[54] Y. van der Laan. Co2 onder de zee: de beste en énige oplossing voor nu. Technical report, EBN, 2018.

[55] D. Haeseldonckx and W. D'Haeseleer. The use of the natural-gas pipeline infrastructure for hydrogen transport in a changing market structure. *International Journal of Hydrogen Energy*, 32(10-11):1381–1386, 2007.

[56] R. Peters (Director Gas Technology, TNO Energy). Personal communication with r. peters on offshore power-to-gas opportunities, March 2018. *TNO Energy coordinates the North Sea Energy program, an industry-driven innovation program that connects the offshore wind sector and gas industry.*

[57] WEC. Bringing north sea energy ashore efficiently. Technical report, World Energy Council Netherlands, 2017.

[58] K. Welkenhuysen. Integration of geoscientific data and uncertainties in techno-economic forecasting on co2 capture and storage. 2017.

[59] The Energy Institute. Hazard analysis for offshore carbon capture platforms and offshore pipelines. Technical report, Global CCS institute, 2013.

[60] P. Linstrom and W. Mallard. *NIST Chemistry WebBook - Standard Reference Database Number 69*. NIST, 2005.

[61] B. Roy. *Fundamentals of classical and statistical thermodynamics*. John Wiley & Sons, 1st edition, 2002.

[62] P. Tipler and G. Mosca. *Physics for scientists and engineers*. W.H.Freeman Co Ltd, 6th edition, 2007.

[63] A. Oosterkamp and J. Ramsen. State-of-the-art overview of co2 pipeline transport with relevance to offshore pipelines. *Polytec Report number: POL-O-2007-138-A*, 2008.

[64] M. Knoope, A. Ramírez, and A. Faaij. A state-of-the-art review of techno-economic models predicting the costs of co2 pipeline transport. *International journal of greenhouse gas control*, 16:241–270, 2013.

[65] A. Olajire. Co2 capture and separation technologies for end-of-pipe applications–a review. *Energy*, 35(6):2610–2628, 2010.

[66] R. Porter, M. Fairweather, C. Kolster, N. Mac Dowell, N. Shah, and R. Woolley. Cost and performance of some carbon capture technology options for producing different quality co2 product streams. *International Journal of Greenhouse Gas Control*, 57:185–195, 2017.

[67] Transport en opslag van co2 in nederland - verkennende studie door gasunie en ebn in opdracht van het ministerie van economische zaken. Technical report, Gasunie & EBN, 2017.

[68] R. Cheng, G. Saini. Co2 mollier chart in metric units. `http://www.chemicalogic.com/Pages/DownloadMollierCharts.html`, 1995. Accessed: 2018-07-01.

[69] R. Van der Straaten, E. Elewaut, D. Koelewijn, H. Baily, S. Holloway, J. Barbier, E. Lindeberg, H. Möller, and K. Gaida. Inventory of the co2 storage capacity of the european union and norway. *Final report of the Joule II project No. CT92-0031: The Underground Disposal of Carbon Dioxide. British Geological Survey, Nottingham*, pages 16–115, 1996.

[70] Ministerie van Economische Zaken & TAQA Offshore B.V. Aanvulling op de aanvraag co2 opslagvergunning p18-4. `https://www.rvo.nl/sites/default/files/sn_bijlagen/bep/70-Opslagprojecten/ROAD-project/Fase1/4_Aanvragen/A-06-2-Aanvulling-opslagvergunning-kl-354540.pdf`, jun 2011. Accessed: 2018-06-12.

[71] Geologische Dienst Nederland & TNO. Velden. `https://www.nlog.nl/kaart-velden`. Accessed: 2018-06-12.

[72] C. Colebrook, T. Blench, H. Chatley, E. Essex, J. Finniecome, G. Lacey, J. Williamson, and G. Macdonald. Turbulent flow in pipes, with particular reference to the transition region between the smooth and rough pipe laws. *Journal of the Institution of Civil engineers*, 12(8):393–422, 1939.

[73] TAQA BV. Near-term co2 storage in the dutch north sea. Technical report, Sintef, 2011.

[74] Schlumberger. Oilfield glossary. `https://www.glossary.oilfield.slb.com/Terms/g/geothermal_gradient.aspx`. Accessed: 2018-09-02.

[75] A. Thompson and B. Taylor. Guide for the use of the international system of units (si). *NIST Special Publication 811*, 2008.

[76] P. Perrot. *A to Z of Thermodynamics*. Oxford University Press, 1998.

[77] B. Clapeyron. Mémoir sur la puissance motrice de la chaleur. *Journal de l'École Royale Polytechnique*, pages 153–190, 1834.

[78] E. Lemmon, M. Huber, and M. McLinden. *NIST Reference Fluid Thermodynamic and Transport Properties— REFPROP*. National Institute of Standards and Technology, 8 edition, apr 2007.

[79] R. Subramanian. Heat transfer in flow through conduits. Technical report, Department of Chemical and Biomolecular Engineering, Clarkson University, 2015.

[80] P. Bernard and J. Wallace. *Turbulent flow: analysis, measurement, and prediction*. John Wiley & Sons, 2002.

[81] F. White. *Fluid Mechanics Seventh Edition*. McGraw-hill, 7th edition, 2011.

[82] A. Mills. *Basic heat and mass transfer*. Pearson, 2nd edition, 2014.

[83] F. White. Heat and mass transfer. *Reading, Mass.: Addison-Wesley*, 1988.

[84] M. Moran, H. Shapiro, D. Boettner, and M. Bailey. *Fundamentals of engineering thermodynamics*. John Wiley & Sons, 6th edition, 2010.

[85] G. Simeoni, T. Bryk, F. Gorelli, M. Krisch, G. Ruocco, M. Santoro, and T. Scopigno. The widom line as the crossover between liquid-like and gas-like behaviour in supercritical fluids. *Nature Physics*, 6(7):503–507, 2010.

[86] W. Salzman. Joule expansion. Technical report, Department of Chemistry, University of Arizona., 2004.

[87] R. Perry, C. Chilton, and S. Kirkpatrick. *Chemical engineers' handbook*. McGraw-Hill New York, 5 edition, 1973.

[88] C. Oldenburg. Joule-thomson cooling due to co2 injection into natural gas reservoirs. *Energy Conversion and Management*, 48(6):1808–1815, 2007.

[89] E. Burnett. Experimental study of the joule-thomson effect in carbon dioxide. *Physical Review*, 22(6):590, 1923.

[90] Rijkswaterstaat - waterdata. `https://www.rijkswaterstaat.nl/water/ waterdata-en-waterberichtgeving/waterdata`. Accessed: 2018-10-02.

[91] S. Churchill and M. Bernstein. A correlating equation for forced convection from gases and liquids to a circular cylinder in crossflow. *Journal of Heat Transfer*, 99(2):300–306, 1977.

[92] T. Newson and P. Brunning. Thermal conductivity of deepwater offshore sediments. *International Journal of Offshore and Polar Engineering*, 14(04), 2004.

[93] S. Beck and R. Collins. Moody chart for pipe friction with smooth and rough walls. University of Sheffield, 2008.

[94] C. Colebrook. Turbulent flow in pipes with particular reference to the transition region between the smooth and rough pipe laws. *Journal of the Institution of Civil Engineers, London*, 11:133–156, 1939.

[95] D. Clamond. Efficient resolution of the colebrook equation. *Industrial & Engineering Chemistry Research*, 48(7):3665–3671, 2009.

[96] Design and operation of co2 pipelines. DNV Recommended Practice RP-J202, DNV-GL, Oslo, Norway, 2017.

[97] A. Raza, R. Gholami, R. Rezaee, C. Bing, R. Nagarajan, and M. Hamid. Co2 storage in depleted gas reservoirs: A study on the effect of residual gas saturation. *Petroleum*, 4(1):95–107, 2018.

[98] L. Moody. Friction factors for pipe flow. *Trans. Asme*, 66:671–684, 1944.

[99] J. Reges, A. Salazar, C. Maitelli, L. Carvalho, and U. Britto. Flow rates measurement and uncertainty analysis in multiple-zone water-injection wells from fluid temperature profiles. *Sensors*, 16(7):1077, 2016.

[100] H. Ramey Jr. Wellbore heat transmission. *Journal of petroleum Technology*, 14(04):427–435, 1962.

[101] M. Deymi-Dashtebayaz, M. Farzaneh-Gord, N. Nooralipoor, and H. Niazmand. The complete modelling of the filling process of hydrogen onboard vehicle cylinders. *Brazilian Journal of Chemical Engineering*, 33(2):391–399, 2016.

[102] R. Oxburgh. Lowest cost decarbonisation for the uk: The critical role of ccs. *Report to the Secretary of State for Business, Energy and Industrial Strategy from the Parliamentary Advisory Group on Carbon Capture and Storage (CCS)*, 2016.

[103] F. Birol. Five keys to unlock ccs investment. Technical report, IEA, 2017.

[104] F. Spors, K. Oppermann, C. Ott, C. Lypiridis, and P. Benitez. Results-based climate finance in practice: Delivering climate finance for low-carbon development, 2017.

[105] P. Hoeller and M. Wallin. *Energy prices, taxes and carbon dioxide emissions*. Number 106. OECD Paris, 1991.

[106] The World Bank. Carbon pricing dashboard. `https:// carbonpricingdashboard.worldbank.org/map_data`. Accessed: 2018-11-4.

[107] Center for climate and Energy solutions. Five keys to unlock ccs investment. Technical report, Pew Center on Global Climate Change, 2011.

[108] R. Stavins. Experience with market-based environmental policy instruments. In *Handbook of environmental economics*, volume 1, pages 355–435. Elsevier, 2003.

[109] European Comission. Commission decision of 8 june 2010 amending decision 2007/589/ec as regards the inclusion of monitoring and reporting guidelines for greenhouse gas emissions from the capture, transport and geological storage of carbon dioxide. Official Journal of the European Union, jun 2010.

[110] ICAP. Eu emissions trading system (eu ets). Technical report, International Carbon Action Partnership, 2012.

[111] B. Hintermann. Allowance price drivers in the first phase of the eu ets. *Journal of Environmental Economics and Management*, 59(1):43–56, 2010.

[112] European Comission. Commision decision of 18 august 2011 on amending decision 2007/589/ec as regards the inclusion of monitoring and reporting guidelines for greenhouse gas emissions from new activities and gases. Official Journal of the European Union, aug 2011.

[113] Quandl. Ecx eua futures, continuous contract. `https://www.quandl.com/data/CHRIS/ICE_C1-ECX-EUA-Futures-Continuous-Contract`, sep 2018. Accessed: 2018-09-17.

[114] Bloomberg News. Carbon reaches 10-year high, pushing up european power prices. `https://www.bloomberg.com/news/articles/2018-08-23/carbon-reaching-20-euros-a-ton-in-europe-raises-price-for-power`, aug 2018. Accessed: 2018-09-21.

[115] D. Leeson, N. Mac Dowell, N. Shah, C. Petit, and PS. Fennell. A techno-economic analysis and systematic review of carbon capture and storage (ccs) applied to the iron and steel, cement, oil refining and pulp and paper industries, as well as other high purity sources. *International Journal of Greenhouse Gas Control*, 61:71–84, 2017.

[116] Tata Steel Europe. Price lists. `https://www.tatasteeleurope.com/en/markets/engineering/strip/price-lists`, oct 2018. Accessed: 2018-10-26.

[117] M. Knoope, W. Guijt, A. Ramírez, and A. Faaij. Improved cost models for optimizing co2 pipeline configuration for point-to-point pipelines and simple networks. *International Journal of Greenhouse Gas Control*, 22:25–46, 2014.

[118] M. Austell. Development of large-scale ccs in the north sea via rotterdam as co2-hub, wp 4.1 final report, sl. Technical report, EU CO2 Europipe Consortium, 2011.

[119] T. Wildenborg, J. Gale, C. Hendriks, S. Holloway, R. Brandsma, E. Kreft, and A. Lokhorst. Cost curves for co2 storage, part 2: European sector. Technical report, Netherlands Institute of Applied Geoscience TNO - National Geological Survey, Utrecht, 2004.

[120] L. Gao, M. Fang, H. Li, and J. Hetland. Cost analysis of co2 transportation: case study in china. *Energy Procedia*, 4:5974–5981, 2011.

[121] J. Van Drunen (Specialist Engineer HMC). Personal communication with j. van drunen about an offshore pressure increasing step for liquid co_2, September 2018.

[122] H. Pershad, K. Harland, A. Stewart, and S. Slater. Co2 pipeline infrastructure: an analysis of global challenges and opportunities. *Final Report (IEAGGP)*, 2010.

[123] J. Meerman, A. Ramírez, W. Turkenburg, and A. Faaij. Performance of simulated flexible integrated gasification polygeneration facilities. part a: A technical-energetic assessment. *Renewable and Sustainable Energy Reviews*, 15(6):2563–2587, 2011.

[124] C. Spaans (Technical Director, HFG). Personal communication with c. spaans on the design of a conceptual conditioning and injection module, October 2018. *Heerema Fabrication Group (HFG) specializes in the engineering and fabrication of large and complex offshore structures.*

[125] FEED Study. Kingsnorth carbon capture & storage project - basis of design for studies – phase 1a. Technical report, E.ON UK plc, 2012.

[126] J. Hazewinkel (Partner, Darel BV). Personal communication with j. hazewinkel about the policy challenges surrounding ccs projects, October 2018. *Darel BV is an energy consultancy involved with the first phase of the Porthos project in the port of Rotterdam.*

[127] K. Macintyre. Design considerations for carbon dioxide injection facilities. *Journal of Canadian Petroleum Technology*, 25(2), 1986.

[128] Carbon Capture Global CCS Institute and Storage Association. Hazard analysis for offshore carbon capture platforms and offshore pipelines. Technical report, Energy Institute, sep 2013.

[129] Submarine pipeline systems. DNV Standard ST-F101, DNV-GL, Oslo, Norway, 2017.

[130] Engineering News. 'pigs' play crucial role in pipeline maintenance. `http://www.engineeringnews.co.za/article/pigs-play-crucial-role-in-pipeline-maintenance-2005-09-09/rep_id:4715/company:fluor-2016-07-04`, sep 2005. Accessed: 2018-10-26.

[131] The Energy Institute. Good plant design and operation for onshore carbon capture installations and onshore pipelines. Technical report, Global CCS institute, 2010.

[132] Radyne Corporation. Induction pipe heating equipment. `https://radyne.com/induction-heating-applications/induction-pipe-heating/`, oct 2018. Accessed: 2018-11-01.

[133] Implementation of Directive 2009/31/EC on the Geological Storage of Carbon Dioxide Guidance Document 2. Characterisation of the storage complex, co2 stream composition, monitoring and corrective measures. Technical report, European Commission, 2011.

[134] Financial Times. Offshore fields use power sent from land. `https://www.ft.com/content/dace18a2-d927-11e4-b907-00144feab7de`, apr 2015. Accessed: 2018-9-16.

[135] Marine Traffic. Platform p15 c. `https://www.marinetraffic.com/nl/ais/details/ships/shipid:260339/mmsi:245453000/imo:0/vessel:PLATFORM_P15_C`, may 2017. Accessed: 2018-10-18.

[136] NAM. Persbericht: Nieuw platform l13fi op z'n plek in de noordzee. `https://www.nam.nl/nieuws/2017/nieuw-platform-l13fi-op-plek-in-de-noordzee.html`, may 2017. Accessed: 2018-10-18.